

Going into (cortical) depth

Laminar imaging and applications for cognitive neuroscience

Jelle A. van Dijk

Going into (cortical) depth

laminar imaging and applications for cognitive neuroscience

De (corticale) diepte in

Laminaire beeldvormingstechnieken en toepassingen voor de cognitieve
neurowetenschappen

(met een samenvatting in het Nederlands)

Proefschrift

ter verkrijging van de graad van doctor aan de
Universiteit Utrecht
op gezag van de
rector magnificus, prof.dr. H.R.B.M. Kummeling,
ingevolge het besluit van het college voor promoties
in het openbaar te verdedigen op

vrijdag 20 maart 2020 des middags te 4.15 uur

door

Jelle Alwin van Dijk

Geboren op 19 mei 1991
te Delft

2 | Going into (cortical) depth

Promotor:

Prof. dr. S.O. Dumoulin

Copromotoren:

Dr. N. Petridou

Dr. A. Fracasso

Contents

General introduction	4
Linear amplitude scaling across cortical depth for laminar fMRI.....	18
Evaluating temporal additivity for laminar fMRI.....	40
Numerosity-selective population receptive field properties across cortical depth.....	57
Intracranial recordings show evidence of numerosity tuning in human parietal cortex	70
General discussion.....	83
References	90
Nederlandse samenvatting.....	104
List of publications	108
Curriculum Vitae	110

Chapter 1

General introduction

Our brain is one of our most important organs. As the control center of the body, it allows us to e.g. breathe, think, perform any kind of (voluntary) action, and perceive our outer and inner environment. It consists of billions of neurons that are divided between the brainstem in the center of the brain, the cerebellum at the bottom of the back of the brain, and the cerebrum (the ‘big brain’; Figure 1A). The brainstem controls basic bodily functions such as breathing, while the cerebellum coordinates voluntary movement. The cerebrum performs higher functions such as learning, speech, decision making, and processing sensory input. The superficial portion of the human cerebrum is called the cerebral cortex or gray matter, as it appears grayish in histological slices. It consists of vast quantities of several types of neuronal cell bodies that are interconnected via their axons and dendrites. Some types of neurons have myelinated axons that extend inwards to neurons in other regions of the brain, or to other parts of the body. The combination of all these myelinated axons has a white appearance and is thus called white matter. The myelinated axons can be thought of as neuronal highways, relaying information from one place in the brain to another. The white matter is largely surrounded by gray matter, which in turn is surrounded by cerebrospinal fluid (CSF). CSF is a clear, colorless fluid that serves as a shock absorber, provides immunological protection, and plays a vital role in the regulation of blood flow in the brain. Most processing in the human brain takes place in gray matter, as this is where the cell bodies and dendrites of neurons generally are located.

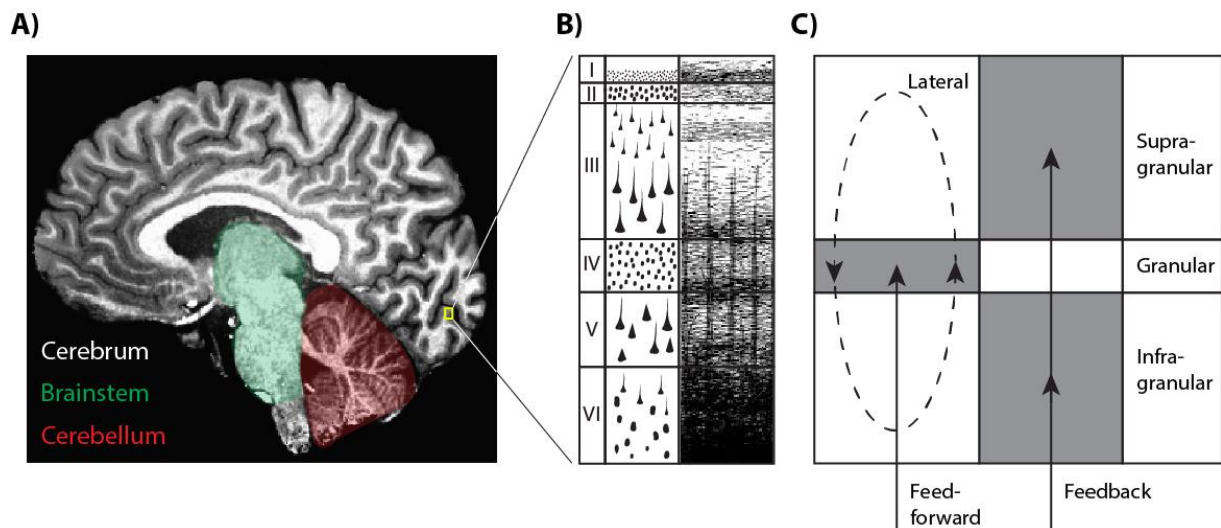


Figure 1: Organization of the human brain. A) Sagittal slice of the brain without skull, indicating the location of the brainstem (green), cerebellum (red), and cerebrum (gray and white). B) Schematic representation of cytoarchitectonic (left column) and myeloarchitectonic (right column) laminar organization of early visual cortex. Roman numerals denote cortical layers. Adapted from: (Duvernoy, Delon, & Vannson, 1981; Miriam D. Waehner). C) Functional connectivity across cortical depth. Cortical depth compartment locations are consistent with cortical laminae in B). After: (Felleman & Van Essen, 1991).

Brain organization

Cortical layers

Zooming in on the human cortex, we see that it is between 1.5 and 4 mm thick (Fischl & Dale, 1999) and that it can be divided into several layers, based on cytoarchitectonic (distribution of cell bodies of neurons; Figure 1B, left panel; Brodmann, 1903, 1909), or myeloarchitectonic (distribution of myelin; Figure 1B, right panel; Gennari, 1782; Nieuwenhuys, 2013; C. Vogt & Vogt, 1919; O. Vogt, 1910) features. These layers -also called laminae- are present throughout the entire brain, although the relative thickness of each of the layers differs between brain areas. Six layers can be defined throughout most of the human cortex (Brodmann, 1909). Laminae can also be defined based on the functional connectivity, which follows a specific pattern across cortical depth (Figure 1C). This functional connectivity can be divided into ascending (feedforward), descending (feedback), and lateral interactions (Felleman & Van Essen, 1991; Shipp, 2007). In the visual system, ascending connections generally terminate in layer IV (Felleman & Van Essen, 1991; Shipp, 2007; Sincich & Horton, 2005). This central layer, also called the granular layer, consists mostly of stellate and pyramidal cell bodies. In primary visual cortex (V1), ascending connections mainly consist of thalamic afferents (Hubel & Wiesel, 1972). For other parts of the visual system, ascending connections mainly contain afferents from visual field maps lower in the visual hierarchy, although this connectivity is less clear-cut than for V1 (Hubel, 1988). Descending (feedback) connections in the cortex mainly terminate in the supragranular and infragranular layers of the cortex (Felleman & Van Essen, 1991). Descending information can come in the form of feedback from other parts of the brain, such as influences of attention. Lateral processing refers to the information flow between neurons located at different cortical depths, but at a similar location at the surface of the cortex.

Cortical blood supply

Neurons need oxygen to function as they cannot store energy themselves. This is supplied by blood vessels. Signals from blood vessels can in turn be used to map brain activity. The cortical vasculature is arranged in a specific way (Duvernoy et al., 1981; Figure 2). Pial arteries delivering oxygen-rich blood run along the cortical (also called pial) surface. As these can only supply oxygen to neurons at the cortical surface, there needs to be a way to deliver oxygen to neurons deeper in the cortex. This comes in the form of diving arteries. These arteries run perpendicular to the cortical surface, extending across multiple cortical layers (Figure 2). These diving arteries then split off further into smaller and smaller arterioles and capillaries, where the oxygen exchange with neurons ultimately takes place. The deoxygenated blood is then removed via the venules that feed into the larger ascending or draining veins (Duvernoy et al., 1981; Havlicek & Uludag, 2019). These draining veins run perpendicular to the cortical surface and deliver their contents to the pial veins at the cortical surface. Thus, there is a clear directionality of blood flow across cortical depth, with oxygenated blood travelling from the cortical surface to the deeper layers of the cortex, and deoxygenated blood travelling from the deeper layers, through more superficial layers, to the cortical surface. The pial arteries, diving arteries, draining veins, and pial veins are collectively called the cortical macrovasculature. Arterioles, capillaries, and venules are collectively called the cortical microvasculature.

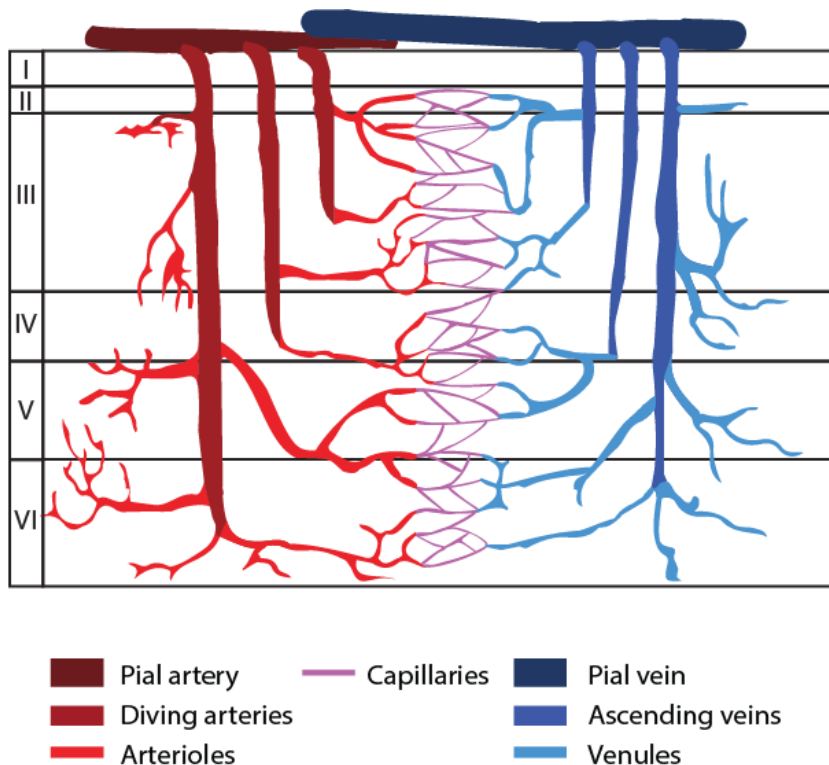


Figure 2: Schematic representation of the cortical vasculature. Red: oxygen-rich blood. Blue: deoxygenated blood. Purple: capillaries, where oxygen is exchanged with neurons.

Visual information processing

Vision is one of our most important senses. Although the eyes are important in collecting visual information, 'seeing' happens in the brain. In fact, roughly 25% of the human brain is dedicated to processing visual information (Van Essen, 2003). When you see an object, any visual information about that object undergoes numerous processing steps to arrive at an integrated percept (Figure 3; Gilbert, 2000). First, light reflecting off the object enters the eye and falls on the retina. Photoreceptors in the retina convert the light to electrical signals that are relayed to the brain through the optic nerve. The optic nerve then passes through the optic chiasm, where signals from the nasal (nose-side) part of each retina cross over. The information that is sent to each hemisphere of the brain from then on contains the retinal signals from two eyes, of only one side of the visual world. Information to the left of fixation (the left visual field) is relayed to the right hemisphere, and information from the right visual field is relayed to the left hemisphere. This information passes through the optic tract to the lateral geniculate nucleus (LGN) and is subsequently sent on via the optic radiation to the primary visual cortex (V1), located in the occipital lobe. There, the first cortical processing step takes place. From there on, the information is sent to higher visual areas. Early and intermediate areas in the visual processing hierarchy process relatively basic stimulus information, such as local contrast, orientation, edges, and motion. Information processing in higher-order visual areas becomes increasingly complex, with visual areas processing information such as the presence of faces, words, houses, or numerosity.

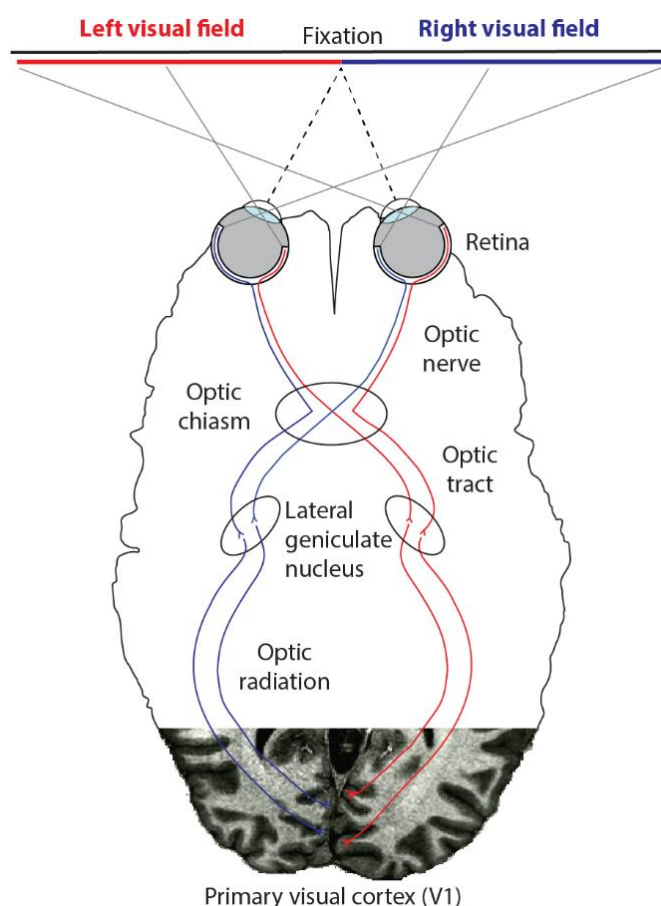


Figure 3: Schematic representation of the visual system. Information from the outside world enters the eye and falls on the retina. This is then passed on via the optic nerves. At the optic chiasm, the information from the nasal (nose-side) part of the retina crosses over to the other hemisphere. Information is then passed on to the primary visual cortex via the optic tract, lateral geniculate nucleus, and optic radiation. All information to the right of fixation (right visual field) is relayed to the left hemisphere, while information from the left visual field is relayed to the right hemisphere. After: (Gray, 1995).

Higher-order information processing: numerosity

Numerosity refers to the set size of a group of items (see Figure 4A, B for examples). Numerosity perception is a trait shared not only among humans from infants onwards, but also among a wide range of other species such as non-human primates, cats, corvids, and zebra fish (Brannon & Terrace, 1998; Ditz & Nieder, 2016a; Hauser, Tsao, Garcia, & Spelke, 2003; Pisa & Agrillo, 2009; Potrich, Sovrano, Stancher, & Vallortigara, 2015). Numerosity perception is advantageous, as for example correctly and quickly judging the number of bananas in a pile or the number of assailants can be essential for a monkey's survival. Numerosity perception is also implicated in many higher cognitive functions, such as multiple object tracking (Piazza, 2011), mathematics (Dehaene, 1997; Halberda, Mazocco, & Feigenson, 2008; Harvey, 2016), decision making (Nieder & Miller, 2003), and dividing attention (Knops, Piazza, Sengupta, Eger, & Melcher, 2014). Neuronal populations selectively responding to numerosity stimuli have been identified using electrodes mostly in animals, and a network of numerosity-selective topographic cortical maps has been identified using functional magnetic resonance imaging (fMRI) in humans (Figure 4C; Harvey & Dumoulin, 2017; Harvey, Klein, Petridou, & Dumoulin, 2013). Even though basic numerosity perception can be studied in animals, it is difficult to study higher-order (visual) processing in any species but humans.

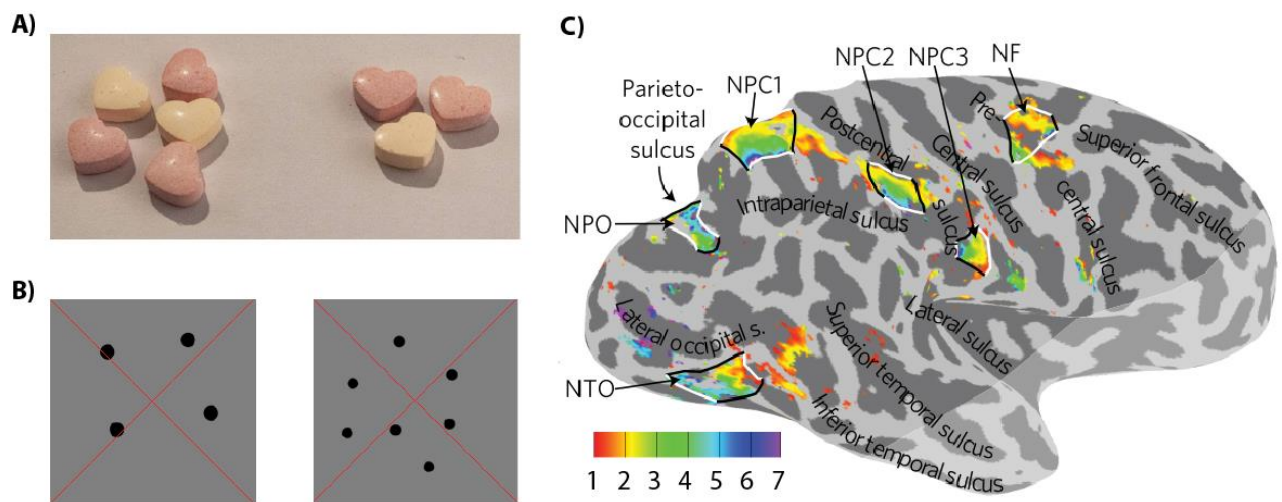


Figure 4: Numerosity examples and numerosity maps in the human brain. A) Selecting the largest pile of heart-shaped candy is essential to satisfy your sweet tooth. The number of candies in each pile is instantly clear, without counting. B) Example numerosity stimuli (4 and 7) as used in this thesis. C) Cortical numerosity-selective topographic maps in the right hemisphere of an example subject. NTO, NPO, NPC1-3, and NF denote different topographic maps. The lighter-gray area at the bottom of the brain denotes the area that was not covered by the fMRI field of view. From: (Harvey & Dumoulin, 2017).

Thesis outline

A significant portion of processing takes place between cortical laminae. In the visual system, sub-millimeter resolution fMRI has been used in the early visual cortex to identify laminar processing for population receptive field sizes (Fracasso, Petridou, & Dumoulin, 2016) and attention effects (Klein, Fracasso, van Dijk, et al., 2018; Kok, Bains, Van Mourik, Norris, & De Lange, 2016). As higher-order (visual) processing is much easier to study in humans than in animals, we look to extend laminar fMRI past basic visual processing. **In this thesis, I investigate laminar processing of higher-order (visual) information.** In **Chapters 2 & 3**, I address methodological challenges of laminar fMRI. I investigate laminar processing for numerosity stimuli in **Chapter 4**. I complement these fMRI findings with neuronal temporal response dynamics using intracranial recordings in **Chapter 5**.

High-resolution methods for human neuroscience

Traditionally, methods to investigate the fine-grained organization of the brain have involved either ex-vivo, or invasive electrode measurements, as non-invasive techniques did not have a sufficient resolution in space (spatial resolution) to e.g. distinguish between different cortical laminae (Gazzaniga et al., 2014). For instance, the identification of cortical layers based on the cyto- and myeloarchitecture was performed solely using slices of brains combined with histological staining methods, while the functional connectivity division of neurons across cortical depth has been based on probing the brains of several animal species with electrodes while they performed a task.

It is unfavorable for human cognitive neuroscience to study brain responses in health and disease using dead brains or other species, as dead brains do not have any neuronal activity (except if you are imaging a salmon and you do the statistics wrong (Bennett, Miller, & Wolford, 2009)) and other species lack e.g. the verbal comprehension that is often required to understand task instructions. Luckily, a variety of imaging methods are available to this end, all with their own benefits and drawbacks (Gazzaniga et al., 2014). To investigate laminar processing in the human brain, we need imaging methods that provide a sufficient spatial resolution, even though that means sacrificing some resolution in the time domain (temporal resolution). We can then complement these methods with imaging techniques that have an inherently high temporal resolution.

Magnetic Resonance Imaging

Magnetic Resonance Imaging (MRI) is a widely used method to investigate both the structure and function of the brain in health and disease. This popularity is due to the wide availability of MRI scanners, as most hospitals have at least one MRI scanner. Additionally, MRI scans do not involve any invasive procedures (e.g. surgery, injection of radioactive tracers, or X-rays), and are safe and easy to administer to most people of most ages. MRI scanners use extremely strong electromagnets to manipulate the spin direction of hydrogen atoms. The strength of this electromagnet is expressed in Tesla (T). Scanners used in a clinical setting typically have magnetic field strengths of 1.5 or 3 T. For comparison, a typical fridge magnet has a field strength of 5 mT, and electromagnets used in scrapyards to effortlessly lift cars are typically around 1 T. These scanners provide sufficient spatial resolution for most clinical applications. As the field strength of a scanner increases, so does the relative signal strength (signal-to-noise ratio; SNR). This increased SNR can be traded for an increased spatial and/or temporal resolution.

The last decade has seen a significant increase in field strength for MRI scanners. Ultra-high fields of 7 T and higher have become available to the research community, providing ever-increasing image quality. One of the major advantages of 7 T (and higher field strength) scanners, is that it allows for the sub-millimeter investigation of the brain at both a structural, and especially a functional level.

fMRI typically measures the ratio between oxygenated and deoxygenated blood in the brain, which is related to neuronal activation (Logothetis, 2002). This is called the blood oxygenation level-dependent (BOLD) signal. The unit of measurement for the spatial resolution of MRI scans is the 3-dimensional pixel, called voxel. A typical voxel size for regular fMRI scans is 2 x 2 x 2 mm. The visual cortex is 1.5 – 2 mm thin. This means that with regular fMRI, one voxel covers the entire thickness of the cortex. Thus, it is impossible to investigate processing across cortical depth at these resolutions. With the advent of ultra-high field MRI scanners, it has become possible to increase the spatial resolution of functional scans to under 1 x 1 x 1 mm. We call this sub-millimeter or laminar fMRI. While at first glance, 1 x 1 x 1 mm might look as though it is a two-fold increase in spatial resolution, it is in fact an eight-fold increase in resolution (8 mm^3 versus 1 mm^3) as voxels are volume measurements. This is further exacerbated for sub-millimeter resolutions, with voxel sizes of functional scans in this thesis reaching as small as only 0.34 mm^3 (smaller voxels result in a higher resolution).

As laminar fMRI has a spatial resolution that is significantly less than the thickness of the cortex, it allows researchers to record signals at different cortical depth portions (De Martino et al., 2018; Dumoulin, Fracasso, van der Zwaag, Siero, & Petridou, 2018; Kashyap, Ivanov, Havlicek, Poser, & Uludağ, 2017). One of the biggest promises of this development is that it has the potential to reveal cortical depth-dependent properties resulting from or involved in feedforward and feedback processing (Dumoulin, 2017; Dumoulin et al., 2018; Self & Roelfsema, 2017). While the ultimate goal of laminar fMRI is to record from different anatomical layers individually, this remains impossible at current spatial resolutions. Therefore, using the term laminar fMRI for sub-millimeter fMRI is technically a misnomer. However, as it is widely used in the sub-millimeter fMRI literature, I will use both the term laminar fMRI as well as sub-millimeter fMRI in this thesis. I use laminar fMRI methods in **Chapters 2, 3, and 4** of this thesis.

Challenges of laminar fMRI

While laminar fMRI holds great promise, data acquisition and analysis at this resolution are non-trivial in practice. Even though it is increasingly popular, these challenges currently prevent it from seeing widespread applications. I will briefly discuss some of them.

Data acquisition challenges and considerations

Functional MRI is an umbrella term for several different data acquisition techniques that are each used to measure a proxy of brain activity. Each of these techniques have their own advantages and disadvantages, and most are based on the BOLD signal. One of these techniques is gradient echo (GRE) echoplanar imaging (EPI) due to its easy implementation, high SNR, good sensitivity to large and small blood vessels, and (relatively) large coverage (Havlicek & Uludag, 2019). GRE-EPI is the general method of choice for regular (non-laminar) fMRI studies, and consequentially also for laminar fMRI. For laminar fMRI, the primary focus is recording signals from the layer-specific microvasculature. However, this is mixed with non layer-specific signals from mainly the venous macrovasculature for GRE-EPI (Havlicek & Uludag, 2019).

Across cortical depth, blood is drained towards the cortical surface (Duvernoy et al., 1981). This directional blood pooling has the consequence that the recorded signal at a given cortical depth is the combination of any signal at that depth, plus the hemodynamic consequences (in- and outflow of (de)oxygenated blood) of signals at all depths below it. Other acquisition techniques, such as spin echo-based ones, have a higher specificity, recording signals from mostly the microvasculature, but are limited in SNR and coverage. Alternative non-BOLD acquisition techniques that have good specificity (ability to selectively record from the microvasculature) and sensitivity (SNR), such as cortical blood volume (CBV) measurements (e.g. VASO; Huber et al., 2015, 2017), are effective but are much more difficult to implement. I use GRE-EPI acquisitions in all fMRI chapters in this thesis.

The increased spatial resolution of laminar fMRI and associated penalty in temporal resolution lead to a very limited coverage of the functional acquisition slab. While at regular resolution, virtually whole-brain functional volumes can be collected in approximately 1.5 s, sub-millimeter resolution functional volumes are limited to 2-3 cm-thick slabs, collected every 1-4 s. Therefore, it is difficult to study large cortical networks quickly with laminar fMRI. Moreover, if anatomical landmarks cannot be identified, or the targeted location is variable between subjects, prior localizer scans might be required for the correct targeting. The placement of the functional volume thus needs to be carefully planned and performed to target the desired location.

In regular scanner setups, the receive coils that are used to record the fMRI signal are distributed around the scalp of the subject. To increase the local SNR, these elements can be placed more closely together, over the desired cortical location. For this, custom-built receive coils are needed. As the increased SNR comes at the cost of a further reduction in the field of view, these coils further complicate the targeting process.

For the best image quality, it is paramount that subjects move their head as little as possible during a scanning session. While this holds true for any MRI scan, it is especially relevant for laminar fMRI, as moving just one millimeter already means a spatial shift of over a voxel. Subject motion can be reduced by using experienced subjects, and by restricting head motion as much as possible using mechanical constraints such as padding around the head, tape, custom head casts, or bite bars. Even though the last two options are effective in reducing motion even in experienced subjects, they can feel very restrictive in the already cramped scanner environment.

Data analysis challenges

Once collected, all fMRI data need to be processed to reduce noise as much as possible, select the voxels that should be included in the analysis by registering the functional volumes to an anatomical scan, and calculate the desired outcome metrics. While this is already non-trivial for fMRI at regular resolution, analyzing laminar fMRI data requires several extra steps and increased precision, further complicating the process. I will discuss the most important of these steps below.

fMRI data contain voxels located in white matter, gray matter, and non-brain matter (CSF, bone, etc.). For data analysis purposes, you typically want to select only the gray matter voxels. Regular resolution fMRI data do not show a clear distinction between white and gray matter. To select the correct voxels, functional volumes are brought to the same space as an anatomical scan and are then positioned in such a way that the volumes are aligned. This process is called (co-)registration. As anatomical scans show a very clear difference between gray and white matter, it is then easy to select only the former and use this to restrict the functional data to only (cortical) gray matter voxels. The distinction between gray and white matter voxels is clearer in laminar fMRI data than for regular resolution fMRI data. It is even possible to select the gray matter voxels immediately from the functional data. Although this was the standard just a few years ago, this approach is extremely tedious as you manually need to draw the gray matter definition for each slice, every time you collect new data. A much faster way to select the desired gray matter voxels, is to register the functional data to anatomical data, just like with regular resolution data. However, fMRI data are distorted due to small inhomogeneities in the magnetic field, resulting in a mismatch between functional and the undistorted anatomical data. These distortions increase with higher field strengths and cause local shifts in voxel locations in the functional volume. These geometrical distortions are present in all fMRI data, but as sub-millimeter fMRI requires more precise registration to the anatomy, it is especially important to correct for these distortions at these sub-millimeter resolutions. To do this, we collect additional functional volumes with identical distortions, but in an opposite direction. This allows for correcting distortions by calculating the undistorted image: the midpoint nonlinear transformation between the two distorted images. Using this correction, it becomes possible to precisely register the laminar fMRI data to the anatomical data. This registration must be done to a great degree of precision, as misaligning a volume by 1 mm already means being more than a voxel off-target.

Apart from the functional data, anatomical data processing also requires additional/adjusted data-analysis steps for laminar fMRI. The resolution of anatomical data used in laminar fMRI studies needs to be sub-millimeter, just like the functional data. A typical whole-brain anatomy covers a couple million voxels. Software that automatically determines which voxels contain white, gray, or other matter has improved over the last years, but most of the current methods still need some manual correction. Next, to be able to perform any analysis across cortical depth, you first need to define at what cortical depth each gray-matter voxel lies. Cortical depth for fMRI is usually expressed as relative depth between 0 (gray-white matter border) and 1 (gray matter-CSF border). Central cortical depth, at a relative depth of 0.5 should correspond with layer IV. Simply dividing the gray matter into equal parts across cortical depth is an attractive option. While this results in layer IV being located at the correct locations in flat pieces of cortex, it under- or overestimates the location of layer IV (and other layers) in the highly curved gyri and sulci of the brain (Waehnert et al., 2014). As it turns out, the total volume of each cortical layer is constant along the cortex, resulting in thick, compressed outer layers and thin, stretched-out inner layers in sulci, and vice versa for gyri. Nowadays, equi-volume depth mapping, which incorporates the changes in relative depth of layers based on this biological principle, is the generally accepted and implemented method for generating cortical depth maps.

Linear systems analysis for laminar fMRI

A fundamental assumption of nearly all fMRI analysis techniques, is that the relationship between local neuronal activity and the BOLD response can be described as linear (Figure 5). That is, the recorded BOLD signal is assumed to be proportional to the local average neuronal activity, averaged over a voxel, over a period of time (Figure 5; Boynton, Engel, Glover, & Heeger, 1996). This is essential for (almost) all analyses that use a standard or subject-specific hemodynamic impulse response function (HRF) to predict the temporal BOLD response pattern in reaction to a set of known stimuli. These predictions are generated by multiplying and temporally summing the assumed HRF. A prime example is any general linear model (GLM) based approach, which are used in most fMRI research carried out to this day. If BOLD response linearity is violated, it leads to under- and/or overestimations and potential mislocalization of activity. Luckily, BOLD linearity at regular resolution holds for most practical applications (e.g. Boynton, Demb, Glover, & Heeger, 1999; Boynton et al., 1996; Boynton, Engel, & Heeger, 2012), although there are some deviations, mostly in event-related designs (e.g. Birn, Saad, & Bandettini, 2001; Kershaw, Kashikura, Zhang, Abe, & Kanno, 2001; Pfeuffer, McCullough, Van De Moortele, Ugurbil, & Hu, 2003; Robson, Dorosz, & Gore, 1998; Soltysik, Peck, White, Crosson, & Briggs, 2004; Vazquez & Noll, 1998; Zhang, Zhu, & Chen, 2008).

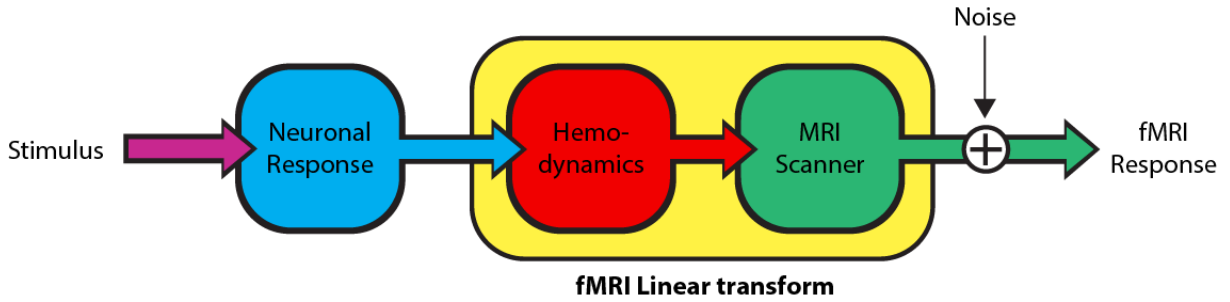


Figure 5: Diagram of the linearity assumption for fMRI. The relationship between the Stimulus and Neuronal Response can be a nonlinear function of any stimulus property. The fMRI Response, consisting of the Hemodynamic consequences of the Neuronal Response and recorded by the MRI Scanner, is linearly related to the Neuronal Response. This is the linearity assumption for fMRI. Noise may be introduced at any stage but can be summarized as a single noise factor. After: (Boynton et al., 1996).

BOLD response linearity for fMRI must adhere to the two assumptions of a linear system: scaling, and temporal additivity (Figure 6). We can define a system with a hemodynamic transform L , neuronal response over time $n(t)$, and the hemodynamic response $H(t)$ as output:

$$L[n(t)] = H(t) \quad (\text{Equation 1})$$

For the scaling assumption to hold, multiplying the neuronal response by a constant k (as the result of e.g. an increase in stimulus intensity) should lead to a k -fold increase in the hemodynamic response:

$$L[kn(t)] = kL[n(t)] = kH(t) \quad (\text{Equation 2})$$

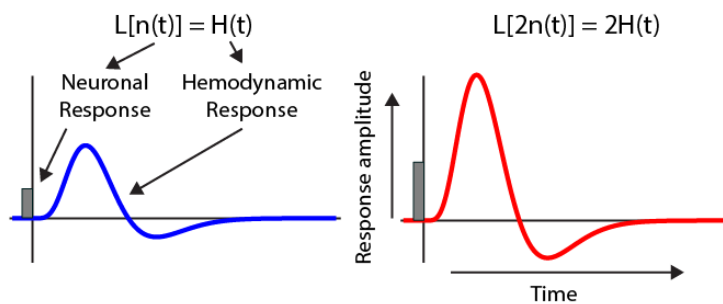
For the temporal additivity assumption to hold, the response to the sum of two neuronal responses should be equal to the sum of the responses of each separate input. Given two neuronal responses $n_1(t)$ and $n_2(t)$, this is formalized as:

$$L[n_1(t) + n_2(t)] = L[n_1(t)] + L[n_2(t)] \quad (\text{Equation 3})$$

The easiest way to visualize this property, is by imagining two neuronal responses that are elicited close in time to each other, such that the hemodynamic response associated with the first neuronal response has not yet returned to baseline when that the second neuronal response is elicited. The temporal additivity assumption then states that the second hemodynamic response -resulting from the second neuronal response- simply adds to the first hemodynamic response, without interacting in any way (Boynton et al., 2012).

For laminar fMRI, the local hemodynamic response at a given depth does not only depend on the local neuronal response, but also on the responses at deeper cortical depths because of directional blood pooling towards the cortical surface. This dependency may result in a violation of the linearity assumptions for laminar fMRI. Therefore, before we can start using laminar fMRI to answer neuroscientific questions, we must first investigate whether the assumptions of a linear system hold for laminar fMRI. In **Chapter 2**, I assess the scaling assumption across cortical depth, and in **Chapter 3** I assess the temporal additivity assumption across cortical depth in the early and intermediate visual cortex (visual field maps V1, V2, and V3).

Scaling



Temporal Additivity

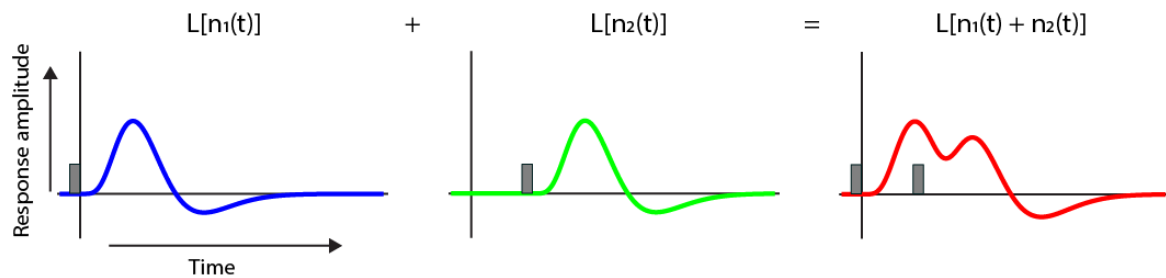


Figure 6: Linearity assumptions for a linear system: Scaling (top row) and Temporal additivity (bottom row). Gray bars represent stimulus presentations. L denotes a hemodynamic transform. Factor $n(t)$ represents the neuronal response over time t . $H(t)$ denotes the hemodynamic response over time t .

Electrocorticography

As neuronal processing happens on the hundreds of millisecond timescale and the temporally sluggish blood response to neuronal activity that fMRI measures progresses on the second timescale, the temporal resolution of (laminar) fMRI leaves things to be desired. Several other non-invasive neuroimaging methods have a significantly better temporal resolution (Gazzaniga et al., 2014). However, this increased temporal resolution comes at the cost of a significantly reduced spatial resolution, as is the case for e.g. electroencephalography (EEG) and magnetoencephalography (MEG). Methods that combine a great temporal resolution with a good spatial resolution thus need to be invasive. Most direct brain recordings are performed using (arrays of) electrodes that are inserted into the brain of an animal. This is an extremely invasive procedure. However, these electrophysiological methods can have a single-neuron resolution, with a temporal resolution in the millisecond range. Even though these methods would be great to use in humans for their spatial and temporal resolution, they are only rarely applied, and only if medically necessary.

A somewhat more common -though still quite rare- method in humans is implanting cortical surface electrodes. These electrodes are typically 1-2 mm in diameter and are placed directly on the cortical surface (electrocorticography; ECoG). These electrodes directly measure the electrical activity of only the neurons that lie directly underneath them (Lachaux, Rudrauf, & Kahane, 2003). The temporal resolution of ECoG is in the millisecond range. As it is an invasive method, ECoG can only be used when this is deemed clinically necessary. This is commonly done in patients with medically intractable epilepsy. When epilepsy is non-responsive to any other treatment, the epileptic focus (the location in the brain from where the epileptic seizures originate) is often surgically removed. To spare as much of the healthy cortex as possible, electrode grids are implanted under the skull of the patient (Lee, Spencer, & Spencer, 2000). The patient is then monitored to identify the exact location of the epileptic focus. This is then used as a guide for neurosurgery. During the monitoring phase, some patients agree to participate in scientific studies. In summary, ECoG provides a relatively high spatial and extremely high temporal resolution, complementing laminar fMRI. Together, these methods can be used to gain a better understanding of the fine-grained functional organization of the human brain.

Summary

Most cortical processing takes place between different laminae of the cortex. With advances in neuroimaging, it is now becoming possible to investigate information processing across cortical depth. While early visual processing at the laminar level is relatively well-studied, much is still unknown about the laminar organization of higher-order (visual) information processing. Although laminar fMRI can be used to investigate laminar information processing, this technique comes with numerous challenges, some of which remain unresolved thus far. One of these issues is the applicability of fMRI analyses based on the assumption of a linear relationship between neuronal activity and BOLD signal amplitude. In **Chapters 2 & 3**, I assess whether the two assumptions that must be met for this linearity, hold across cortical depth. I perform these measurements in the visual system.

In **Chapters 4 & 5**, I investigate higher-order visual information using high-resolution methods. Specifically, I investigate laminar processing of numerosity information in the parietal (association) cortex using laminar fMRI in **Chapter 4**. As little is known about laminar processing of higher-order visual information, I use the information flow in the early visual cortex as hypothesis. In the early visual system, processing progresses from central cortical depth towards both the deep and superficial layers. In **Chapter 5**, I complement the high spatial resolution study of the previous chapter by exploring the temporal characteristics of numerosity processing using intracranial recordings.

Chapter 2

Linear amplitude scaling across cortical depth for laminar fMRI

van Dijk, J.A., Fracasso, A., Petridou, N., & Dumoulin, S.O., Linear amplitude scaling across cortical depth for laminar fMRI (submitted)

Acknowledgement of author contributions

JAvD, AF, and SOD designed the experiment. JAvD and AF collected and analyzed the data. All authors contributed to and reviewed the main manuscript text. JAvD prepared all figures. SOD and NP provided general supervision and guidance throughout.

Abstract

A fundamental assumption of nearly all functional magnetic resonance imaging (fMRI) analyses is that the relationship between local neuronal activity and the blood oxygenation level dependent (BOLD) signal can be described as following linear systems theory. With the advent of ultra-high field (7T and higher) MRI scanners, it has become possible to perform sub-millimeter resolution fMRI in humans. A novel and promising application of sub-millimeter fMRI is measuring responses across cortical depth, i.e. laminar imaging. However, the cortical vasculature and associated directional blood pooling towards the pial surface strongly influence the cortical depth dependent BOLD signal, particularly for gradient-echo BOLD. This directional pooling may potentially affect BOLD linearity across cortical depth. Here we assess whether the amplitude scaling assumption for linear systems theory holds across cortical depth. For this, we use stimuli with different luminance contrasts to elicit different BOLD response amplitudes. We find that BOLD amplitude across cortical depth scales with luminance contrast, and that this scaling is identical across cortical depth. Our results suggest that the amplitude scaling assumption for linear systems theory across cortical depth holds for luminance contrast manipulations in sub-millimeter laminar BOLD fMRI.

Introduction

The cerebral cortex consists of separate cortical regions that perform specialized computations. The first parcellation of the cortex into separate cortical regions was based on anatomical differences across cortical depth, i.e. cortical layers or laminae (Brodmann, 1903, 1909; Gennari, 1782; Nieuwenhuys, Broere, & Cerliani, 2015; C. Vogt & Vogt, 1919; O. Vogt, 1910, for reviews see Geyer & Turner, 2013; Nieuwenhuys, 2013).

Magnetic resonance imaging (MRI) is one of the most popular techniques to study the human brain non-invasively. The recent development in static magnetic field strength to ultra-high fields of 7 Tesla and higher, has enabled researchers to investigate the human brain at a sub-millimeter (mesoscopic) scale. At this spatial resolution, it becomes possible to measure both anatomical and functional cortical depth dependent signals that reflect contributions of different cortical layers. Sub-millimeter laminar functional MRI (fMRI) promises to complement anatomical measurements across cortical depth with functional properties that may indicate feedforward and feedback processes (Dumoulin et al., 2018; Self & Roelfsema, 2017).

However, fMRI across cortical depth faces substantial challenges (Dumoulin et al., 2018; Kashyap et al., 2017; Yacoub, De Martino, & Ugurbil, 2018). One dominant challenge relates to the cortical vascular organization. While fMRI detects hemodynamic consequences of neuronal activity (Heeger, Huk, Geisler, & Albrecht, 2000; Logothetis, 2002), the cortical vasculature has a specific organization across cortical layers: blood flows from pial and intracortical arteries and arterioles to the capillary bed that directly interfaces with neuronal tissue, and is then drained via venules and intracortical veins to larger pial veins at the cortical surface (Duvernoy et al., 1981; Turner, 2002). This likely explains a large part of the consistently reported finding that BOLD signal amplitude is larger at the cortical surface and systematically decreases toward deeper layers (see e.g. Chen, Wang, Gore, & Roe, 2012; De Martino et al., 2013; Dumoulin, 2017; Dumoulin et al., 2018; Fracasso, Van Veluw, et al., 2016; Kim & Ress, 2017; Koopmans, Barth, Orzada, & Norris, 2011; Koopmans, Boyacıoğlu, Barth, & Norris, 2012; Lawrence, Formisano, Muckli, & de Lange, 2017; Polimeni, Fischl, Greve, & Wald, 2010; Puckett, Aquino, Robinson, Breakspear, & Schira, 2016; Self, van Kerkoerle, Goebel, & Roelfsema, 2019; J. C. Siero, Petridou, Hoogduin, Luijten, & Ramsey, 2011; van den Berg, Klomp, & Petridou, 2016; Yu, Qian, Chen, Dodd, & Koretsky, 2014; Zimmermann et al., 2011). The vascular architecture across cortical depth has also been modeled in detail e.g. (Boas, Jones, Devor, Huppert, & Dale, 2008; Reichold et al., 2009) and poses a fundamental challenge for the analysis of laminar fMRI as blood pooling effects might differently affect the blood oxygenation level dependent (BOLD) signal in deeper layers compared to more superficial ones (Heinzle, Koopmans, den Ouden, Raman, & Stephan, 2016).

Furthermore, due to the directional blood pooling across layers, hemodynamic responses from deeper cortical layers influence signals at superficial layers. For example, if there is neuronal activity in the deeper cortical depth portions only and not in the more superficial ones, a BOLD signal change would be measured at all cortical depths, due to this directional blood pooling (see Figure 1, lowest red line). Theoretically, this could occur in absence of feedforward signals due to clinical manifestations (see e.g. Masuda, Dumoulin, Nakadomari, & Wandell, 2008), or in situations where neuronal activity is primarily driven by feedback signals -typically arriving in the supragranular and/or infragranular depth portions, as demonstrated by Kok and colleagues (Kok et al., 2016) and Klein et al (Klein, Fracasso, Dijk, et al., 2018).

In summary, the specific cortical vascular organization can potentially undermine fundamental assumptions in fMRI analysis at the sub-millimeter scale. Nearly all fMRI data-analysis techniques assume that fMRI responses are linearly proportional to a local average neuronal activity over a period of time following linear systems theory (Boynton et al., 1996). For this theory to hold, two assumptions must be met: scaling and temporal additivity. These assumptions have been tested for conventional supra-millimeter fMRI for which they largely hold, provided that the stimuli used are within a defined range of stimulus parameters that is commonly used in neuroimaging experiments (see e.g., Boynton et al., 1996; Boynton, Engel, & Heeger, 2012; Cohen, 1997; Friston, Jezzard, & Turner, 1994; Heeger et al., 2000; Miezin, Maccotta, Ollinger, Petersen, & Buckner, 2000); for nonlinearities, mostly found in event-related designs (see e.g., Birn, Saad, & Bandettini, 2001; Kershaw, Kashikura, Zhang, Abe, & Kanno, 2001; Pfeuffer, McCullough, Van De Moortele, Ugurbil, & Hu, 2003; Robson, Dorosz, & Gore, 1998; Soltysik, Peck, White, Crosson, & Briggs, 2004; Vazquez & Noll, 1998; Zhang, Zhu, & Chen, 2008). The laminar BOLD signal amplitudes and directional blood pooling across layers potentially violate these assumptions, as different portions across cortical depth are not independent.

Here we test whether the scaling assumption for a linear system holds in human visual cortex for BOLD amplitude across cortical depth using the most common acquisition protocol at 7T; gradient echo (GRE) BOLD fMRI. Thus, we seek to extend the BOLD linearity assumption to the cortical depth domain, specifically for amplitude scaling. If we define a system with a hemodynamic transform L , neuronal response over time $n(t)$, and the hemodynamic response $H(t)$ as output:

$$L[n(t)] = H(t) \quad (\text{Equation 1})$$

For the scaling assumption to be satisfied, the new output must be equal to the original output, multiplied by a constant k :

$$L[kn(t)] = kL[n(t)] = kH(t) \quad (\text{Equation 2})$$

On a sub-millimeter level, however, the hemodynamic response at depth d does not only depend on the local neuronal response, but also on responses at deeper cortical depths because of the draining effects towards the cortical surface. Thus, the hemodynamic response at depth d can be expressed as:

$$H_c(d) = L[n(t)]_d + \sum_{i=d_0}^{d-1} w_i H_c(i) \quad (\text{Equation 3})$$

Where $H_c(d)$ is the hemodynamic response at depth d ; $L[n(t)]_d$ is the hemodynamic transform of the local neuronal response over time at depth d ; and $\sum_{i=d_0}^{d-1} w_i H_c(i)$ reflects the draining from the sum of the hemodynamic response $H_c(i)$ at all cortical depths below depth d , up to the gray-white matter surface d_0 , each weighted by a factor w_i . This weighting factor represents an estimation of the draining of altered deoxyhemoglobin content and increased blood pressure from lower layers (Marquardt, Schneider, Gulban, Ivanov, & Uludağ, 2018). The hemodynamic response at a given depth is thus a combination of the local neuronal activity and draining from deeper layers. Therefore, the hemodynamic response is not only dependent on the neuronal responses at that location (or depth) but also on the neuronal responses at other locations (depths). This dependence might violate the assumption that the hemodynamic response is proportional to the underlying local neuronal activity and could drive the system nonlinear. For example, if task demands drive deeper cortical depths more actively than more superficial depths due to feedback connections (Angelucci et al., 2002; Felleman & Van Essen, 1991), this would result in an increase in the hemodynamic response at all depths, while there is no additional local neuronal component at most depths. This is illustrated in Figure 1, lower red curve. This violates the scaling assumption between cortical depths.

We can express the scaling assumption across cortical depth as:

$$H_{c2}(d) = kH_{c1}(d) \quad (\text{Equation 4})$$

Where $H_{c1}(d)$ and $H_{c2}(d)$ are the hemodynamic responses at each cortical depth d , for condition $c1$ and $c2$ respectively, and k is a scaling constant from one stimulus condition to another (Figure 1, green curve), which should be constant across depth for the scaling assumption to hold across cortical depth.

We used stimuli with different luminance contrasts (i.e. sinewave gratings with 5, 20, and 80% luminance contrast) to elicit gradually increasing neuronal responses. For linear amplitude scaling across cortical depth to hold, the BOLD response amplitude across cortical depth to a higher contrast (Figure 1, green curve) should be equal to the response profile across cortical depth for a lower contrast multiplied with a scaling factor k that is independent of cortical depth (Figure 1, gray curve), therefore retaining the shape but changing in amplitude. Figure 1 also shows two changes in response amplitude that do not follow linear systems theory (Figure 1, red lines). For example, an intercept shift due to e.g. a spatially restricted increase in neuronal activation does not satisfy linear systems theory requirements (Figure 1, lower red curve).

All subjects participated in two sessions. In one session, participants passively fixated the center of a large fixation cross, while they performed a one-back motion direction discrimination task in the other session. We find that response amplitudes increase with increasing contrast and increase towards the cortical surface. Scaling these responses according to linear systems theory resulted in a substantial overlap between contrasts, supporting the validity of linear amplitude scaling for GRE-BOLD fMRI across cortical depth for stimulus luminance contrast. Correspondence between sessions was excellent.

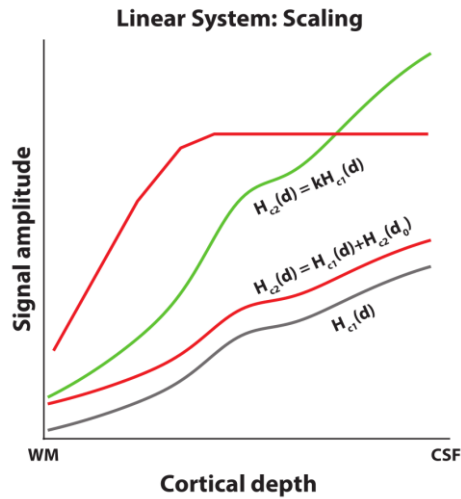


Figure 7: Theoretical response amplitude changes across cortical depth as luminance contrast increases. See also Equation 4. WM = white matter, CSF = cerebrospinal fluid. Gray line: Base response amplitude across cortical depth for a given contrast, $H_c(d)$, red and green lines indicate theoretical response changes as the luminance contrast increases. The green line satisfies the scaling requirement according linear system theory, i.e. the response increase corresponds to a multiplication of $H_c(d)$ with a scaling factor k , resulting in $kH_c(d)$. Both red lines indicate potential increases in responses that do not follow linear system theory. The lower red line corresponds to adding a response at the deepest cortical depth d_0 , and the resulting draining offset to the original BOLD response, $H_c(d) + H_{c2}(d_0)$. Although this is a linear transformation, this does not satisfy the scaling requirement for a linear system. The upper red line corresponds to a response increase that includes a maximum response. A maximum response is also a nonlinear - and biologically plausible - transformation.

Methods

Participants

Five participants (all male, age range 23-44 years) took part in the experiment. One participant was left-handed. All participants had normal or corrected-to-normal visual acuity and were experienced with the MRI environment. Informed consent was acquired from all participants. All experimental procedures were conducted in accordance to the Declaration of Helsinki and approved by the ethics committee of the University Medical Center Utrecht.

Stimuli

Stimuli were presented on a 32" LCD screen, specifically designed for use in an MRI environment (Cambridge Research Systems, 2012). The screen resolution was 1920x1080 pixels, with an active area of 69.8 x 39.3cm and a refresh rate of 120Hz, with a built-in linear luminance look-up table. The display was positioned at the end of the bore, and viewed via a mirror, at a total viewing distance of 220cm. The stimulus diameter subtended 10.2 degrees of visual angle (deg).

All stimuli were generated with MATLAB (Mathworks, 2015b) using the Psychophysics Toolbox (Brainard, 1997; Pelli, 1997). A green fixation cross (0.1 deg in diameter) stretching from corner to corner throughout the center 10.2 deg, was presented at all times. The stimuli consisted of sinewave gratings (0.5 cycles per degree) oriented in any of 4 possible directions (0-135 deg in 45 deg steps; Figure 2A; similar to (Masuda et al., 2010)). The gratings were moving perpendicular to the orientation of the bars at 1.76 deg per second and limited by a circular aperture with 5.1 deg radius. Movement was either towards the left, or towards the right edge of the screen. The luminance contrast of the gratings was 5, 20, or 80%. These contrasts largely lie within the approximately linear range of stimulus space (Boynton et al., 1999).

Stimuli and fixation cross were presented for 12 seconds, followed by a 12-second period of mean luminance baseline with the fixation cross. During the 12 seconds of stimulus presentation, stimuli were shown each time for 750 ms, followed by 250 ms of mean luminance. The subsequent presentation randomly moved in the same motion direction as the previous presentation (12.5% chance), or not. No more than two consecutive presentations could have the same motion direction. Each block contained a stimulus of only 1 luminance contrast. Each run consisted of 15 blocks (5 blocks of each contrast, presented in a semi-randomized order). As the repetition time of the functional volumes was very long and averaging between session is undesirable at sub-millimeter resolution, this design was the most reasonable.

Task

Participants completed two sessions. Each session consisted of 6 or 7 runs. The same stimuli were used during both sessions. During one session, participants were instructed only to fixate the center of the fixation cross. To assess the stability of amplitude scaling between sessions, subjects performed a one-back motion direction discrimination task on the other session. During this session, participants were instructed to fixate the center of the fixation cross and indicate whenever two consecutive stimulus presentations had the same motion direction by means of a button press.

Visual field maps definition

Visual field maps were acquired in separate scanning sessions, using near-identical procedures as in previous studies (e.g. Dumoulin & Wandell, 2008). All visual field maps were restricted to 5.1 degrees eccentricity -the radius of the stimulus in this study- based on eccentricity estimates following the population receptive field (pRF) approach (Dumoulin & Wandell, 2008). All data were collected using a Philips Achieva 7T scanner (Philips, Best, the Netherlands) using a dual-channel volume transmit coil

and a 32-channel receive coil (Nova Medical, MA, USA), using a 2D-EPI sequence. For participants S1, S4, and S5, visual field mapping data were collected using a traversing bar-stimulus as in (Dumoulin & Wandell, 2008), but with gray-scale natural images as carrier. Functional data were acquired at a 1.8 mm isotropic resolution, with a TR/TE = 1500/25 ms, and 248 time points per run. Three runs were collected for each participant. For S2, and S3, identical stimuli were used as by Dumoulin & Wandell. For S2, 8 functional runs were collected at a resolution of 2 mm isotropic, and TR/TE = 1500/25 ms (248 time points per run). For S3, 7 functional runs were collected at a resolution of 1.8 mm isotropic, TR/TE = 2100/25 ms (182 time points per run). Visual field maps for visual areas V1, V2, and V3 were defined for all participants (Figure 2B).

High resolution MRI and fMRI acquisition

High resolution anatomical and functional data were acquired using a Philips Achieva 7 T scanner with a maximum gradient strength of 40mT/m and a slew rate of 200 T/m/s (Philips, Best, The Netherlands). A dual-channel volume transmit coil was used for all scans (Nova Medical, MA, USA). A 32-channel receive coil (Nova Medical, MA, USA) was used for all anatomical scans, while two custom-built 16-channel high-density surface receive arrays were used for all functional scans (MRCoils BV; Petridou et al., 2013). These surface arrays were positioned adjacent so that the two arrays touched each other lengthwise but did not overlap. Participants were positioned such that their external occipital protuberance was approximately aligned with the center between the arrays, at the height of the most distal receive elements from the isocenter.

Anatomical data were acquired using an MP2RAGE sequence (Marques et al., 2010). Whole-brain sequence parameters were: TI1 = 800 ms, TI2 = 2700 ms, TR_{MP2RAGE} = 5500 ms, TR/TE = 6.2/2.3 ms, flip angle $\alpha_1 = 7^\circ$, and $\alpha_2 = 5^\circ$, bandwidth = 403.7 Hz/pixel, acceleration factor using SENSE encoding = 3.5 x 1.3 (RL and AP respectively), resolution = 0.64mm isotropic, total scan time 9 min 57 s.

Functional data were acquired with a T2*-weighted 3-dimensional multi-shot EPI (3D-EPI, two shots per slice, 34 slices, 68 shots overall). The sequence parameters were: TR/TE = 59/28 ms, flip angle: 20°, acceleration factor using SENSE encoding: 3.5 (right-left) x 1.3 (anterior-posterior), echo planar factor: 27, bandwidth (phase-encode): 19.1 Hz/pixel, voxel size = 0.70mm isotropic, FOV = 131 (right-left) x 120 (feet-head) x 24 (anterior-posterior) mm, 34 coronal slices, and 28% oversampling in the slice direction. Functional volumes were acquired every 4 s and functional scans were each 91 time frames (364 s) in duration.

Additionally, we acquired ‘topup’ functional data with reversed right-left phase-encoding and geometrical distortions in opposite directions from the original functional data (Andersson, Skare, & Ashburner, 2003). Images with opposite phase encoding polarities were extracted, and susceptibility induced distortion was estimated using nonlinear warping to estimate the undistorted mid-point between the two volumes in AFNI (Cox, 1996). Five volumes were acquired per topup run. For each session, 6 or 7 functional and accompanying topup runs were acquired for each participant.

Pre-processing: functional data

The fMRI data pre-processing was performed using AFNI. First, motion parameters between runs were computed by aligning the first volumes for each run to the first volume of the first run. Subsequently, motion parameters within runs were calculated by aligning each volume within a run to the first volume of that run. The individual motion-corrected runs were then despiked, scaled, and detrended. During the scaling step, the time-series for each run and every voxel were converted to percentage BOLD by dividing the signal of each voxel by its temporal mean, multiplying the resulting signal with 100, and subsequently subtracting 100 to ensure that the mean temporal response for each voxel was zero percent. The detrending step was performed using the AFNI function 3dDtrend with a fourth-degree polynomial detrending. A warp field to correct for geometric distortions in the 3D-EPIs was calculated using a nonlinear transformation, performed on the original (non-motion corrected, scaled, despiked, or detrended) volumes. For this, the first 5 volumes of the 3D-EPI for each run, and the 5 volumes of each topup 3D-EPI run were used. As the 3D-EPI volumes have the opposite distortions in the phase-encoding direction from the topup 3D-EPI, the undistorted 3D-EPI volume is the halfway warping between the two extremes (Andersson et al., 2003).

Next, the motion estimates and warp field results were combined to calculate the 3D-EPI mean image, averaging over all warped and motion corrected volumes between runs and collapsing over all time points. This mean EPI image was then registered to the anatomical data. This process involved several steps. First, the anatomy was clipped so that only the occipital lobe was left. Then the anatomy and mean EPI image were brought into the same space by aligning their respective centers of mass. Next, the 'Nudge dataset' plugin in AFNI was used to provide a good starting point for the automated registration. This registration consisted of two affine transformations, using the local Pearson correlation as cost function (Saad et al., 2010). The first one allowed for a maximum shift and rotation of 3mm. The second iteration allowed for a maximum shift and rotation of 1mm. The transformation matrices for the manual and automated steps were joint into a single affine matrix. To reduce the number of interpolation steps we applied this registration matrix along with the warp field (see previous paragraph) in a single step to each motion-corrected, despiked, scaled, and detrended run (see previous paragraph) to align these volumes to the registered mean EPI image. For this, we used the AFNI function 3dNwarpApply with nearest neighbor interpolation. Then, the resulting volumes were resampled into anatomy space to allow for accurate cortical depth calculation, using nearest neighbor interpolation. This procedure resulted in registered time-series for each run. All in all, our procedure involved a total of two spatial interpolation steps to get from the motion-corrected, despiked, scaled, and detrended runs to the registered, topup-corrected time-series for each run in anatomy space.

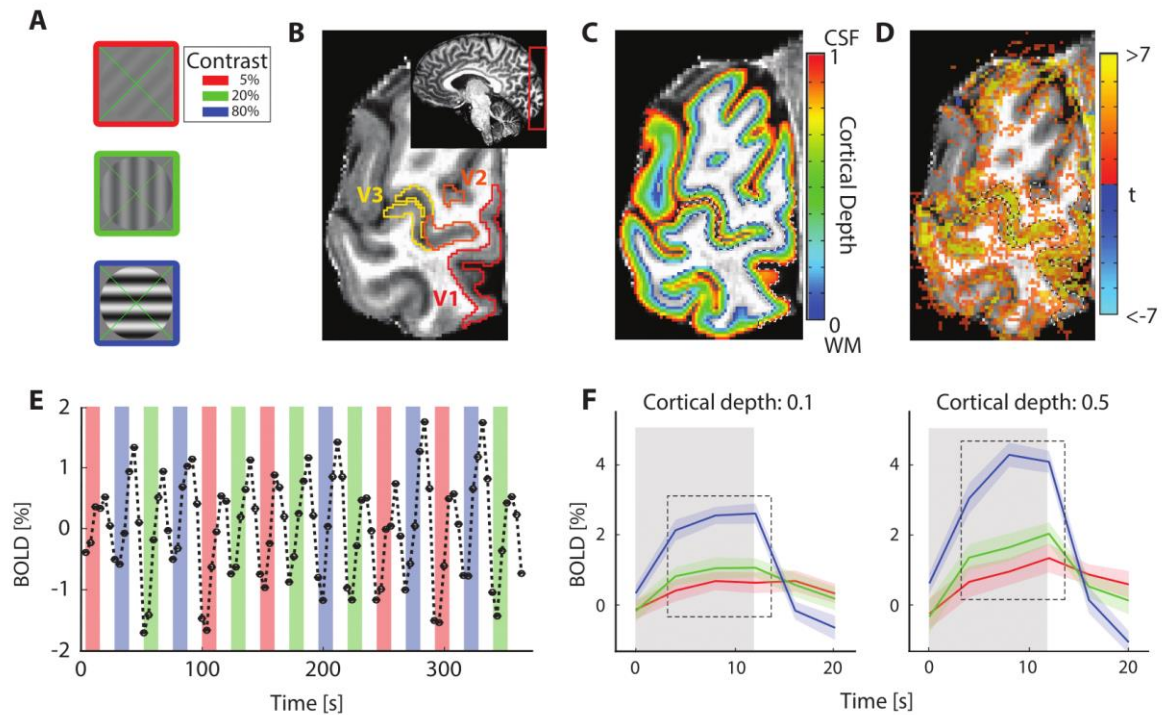


Figure 2: Stimulus design and processing steps. A) Example stimuli with 5% (red border), 20% (green border), and 80% (blue border) luminance contrast. B) Example anatomical slice with visual field map definition overlay. Inset: slab positioning for functional data acquisition. C) Anatomical slice with volume-preserving depth map (colored), and visual field map (dashed lines) overlay. D) Anatomical slice with t -statistical map (colored), and visual field map (dashed lines) overlay. This illustrates the accuracy of the registration. This statistical map is only used for illustrative purposes. E) Example time-series. Colors correspond to luminance contrast presentations with the same color-code as figure 2A. Colored bars represent when the stimulus was shown, transparent bars represent the presentation of mean-luminance baseline. F) Averaged block responses at relative cortical depth 0.1 and 0.5, where 0 is the gray-white matter border, and 1 is the gray matter-cerebrospinal fluid border. The line color corresponds to responses elicited by the luminance contrasts as in figure 2A. Error regions represent ± 2 standard errors (95% confidence intervals) of the mean across repeated stimulus presentations for V1. Gray rectangle represents when a stimulus was presented. Dashed box represents the time points included in the analysis.

Pre-processing: anatomical data

The MP2RAGE anatomical images were segmented using the CBS-tools plugin (Bazin et al., 2007) (www.nitrc.org/projects/cbs-tools/) in MIPAV (<http://mipav.cit.nih.gov/>), and subsequently manually optimized in 3D Slicer (Fedorov et al., 2012). Next, a volume-preserving distance map between the gray matter-white matter (GM/WM) border and the gray matter-cerebrospinal fluid (GM/CSF) border was computed (Waehnert et al., 2014) in 6 separate level-set volumes. This approach takes into account cortical folding in the depth estimation and is implemented in CBS-tools. These level sets were projected on the 3D-EPI space for subsequent laminar analysis (Figure 2C).

Analysis

BOLD across cortical depth

For each participant, visual field map (V1, V2 and V3) and luminance contrast, we took each registered, topup-corrected time-series (Figure 2E) and divided these into 24s blocks, each starting at stimulus onset. The volume-preserving distance map was divided in 5 quantiles, spanning from gray matter-white matter (GM/WM) border to gray matter-cerebrospinal fluid (GM/CSF) border. We calculated the mean percentage BOLD signal change for the response amplitude of the second, third, and fourth sampling point in a block (at 4, 8, and 12 s after stimulus onset respectively; see Figure 2F, dashed box), and the standard error of the mean across repeated stimulus presentations for each depth bin and luminance contrast (Figure 2F). Note that this approach ignores the depth-dependent differences in temporal BOLD response characteristics (see e.g., Siero et al., 2015, 2011). As the temporal resolution in this experiment is 4 s, we only sample a few points of the response curve, and these temporal BOLD response differences are too small to effectively pick up at this temporal resolution. Moreover, averaging over the sampling points further reduces the presence of small temporal differences. Initial analysis using a basic general linear model (GLM) with luminance contrast as independent variable, yielded near identical results. This type of analysis also takes the post-stimulus undershoot into account. However, as the basic assumptions for a GLM include that the system that is being tested adheres to linear systems theory, this analysis is inherently circular and therefore not used in this study. We calculated the across repeated stimulus presentations of the BOLD response amplitudes to each luminance contrast for each visual field map by dividing the across repeated stimulus presentations standard deviation by the mean signal amplitude across repeated stimulus presentations at each depth bin. These estimates were then averaged over participants (Figure 2G-I). Similar measures were previously used for depth-dependent fMRI by Kim & Ress (J. H. Kim & Ress, 2017).

Linearity assessment

To assess the response linearity across cortical depth, we first plotted all unique combinations of BOLD amplitudes across cortical depth ($H_{c1}(d)$ and $H_{c2}(d)$) to two out of three different contrasts across cortical depth against each other for each individual participant and visual field map (5% vs 20%, 20% vs 80%, and 5% vs 80% grating contrast for V1, V2, and V3; see Figure 4A-C for group averages, and Figure S 2 for individual contrast pairs). We then used a linear fit to estimate the best fitting line to the BOLD amplitudes from each of the combinations of BOLD responses across cortical depth mentioned above. Only a slope parameter was estimated with this linear fit as is required to satisfy the linear amplitude scaling assumption. This was done for all individual participants, and repeated for V1, V2, and V3. This estimated slope of the best fitting line then corresponds to the scaling constant k in Equation 4.

Next, we overlaid the responses to different contrasts for each participant and region of interest by scaling each stimulus contrast response ($H_{c2}(d)$) by a constant k to fit other measured luminance contrast responses over depth ($H_{c1}(d)$ see Figures 4D-F and 5D-F for group averages). As there were multiple luminance contrasts, multiple scaling constants were estimated, one for each combination of $H_{c1}(d)$ and $H_{c2}(d)$. These scaling constants were estimated using a regression for each luminance contrast pair, fitting only a slope parameter to scale one luminance contrast response amplitude over depth to the other, thus omitting the intercept estimation. Then, we calculated the explained variance of the original responses ($H_{c1}(d)$) based on the scaled responses to the other contrasts $kH_{c2}(d)$ to assess the degree of linearity of the responses across cortical depth. Explained variance was calculated for each pair of contrasts (one original, and one scaled) separately. Note that the calculated amplitude scaling constants and explained variance using this approach, and the approach used in the previous

paragraph, are identical. However, the results from the analysis in this paragraph are displayed on the group level. As such, the two approaches are complementary. All procedures were performed for the initial (fixation-only) and the retest (one-back task; Figure 5A-F) sessions separately. To assess the reliability of scaling between sessions we overlaid the response amplitudes for both sessions on each other (Figure 5G-I) and calculated the explained variance between sessions.

Additionally, we calculated the average response amplitude over cortical depth between contrasts by averaging the three luminance contrast responses. This averaged response was then scaled to each individual luminance contrast response over cortical depth in the same way as described in the previous paragraph. Next, we calculated the explained variance between these scaled responses and the original responses for each of the three pairs (scaled and original response amplitude over depth). Results of this analysis can be found in Figure S3. Note that this approach already includes a weighted version of the scaling target response in the averaged response. These responses are therefore not independent of each other. In the other approaches described in this section, the luminance contrast response pairs are independent of each other.

Results

BOLD signal amplitude increases with luminance contrast and cortical depth

For each subject, the fMRI signal increased both as a function of luminance contrast and cortical depth in V1-3 (see Figure 3A-C for V1 for three example participants; for additional participants see Figure S1). These signal increases are consistent with previous literature reporting increases with luminance contrast (Boynton et al., 1996, 2012) and cortical depth (J. H. Kim & Ress, 2017; Muckli et al., 2015; Polimeni et al., 2010; Siero et al., 2011). The latter is expected based on the cortical vasculature, as blood pooling increases towards the pial surface (Duvernoy et al., 1981). The standard error across repeated stimulus presentations increased towards the cortical surface. This is expected as thermal noise scales with signal amplitude.

Next, we averaged the different subjects and observed the same signal increase (Figure 3D-F). For example, in the central depth bin of V1 (Figure 3D), the 5% luminance contrast elicited a response amplitude of 0.8% BOLD, whereas 20% and 80% luminance contrast elicited 1.1% BOLD and 2.6% BOLD respectively in the same depth bin. For V2 (Figure 3E), the 5%, 20%, and 80% luminance contrast elicited a response amplitude of 1.3, 1.6, and 2.4 % BOLD in the central depth bin respectively. For V3 (Figure 3F), these values were 1.5, 1.7, and 2.4% BOLD respectively.

Variability across cortical depth (Figure 3G-I) was expressed by dividing the standard deviation of the signal amplitude over voxels at a given cortical depth bin within a given visual field map by the mean signal amplitude across repeated stimulus presentations at each depth bin within each visual field map, expressed as a percentage. This was calculated for each participant separately. Variability was highest for 5% luminance contrast responses for all visual field maps, with 80% consistently showing the lowest variability. Variability was generally lowest around the central depth bins, increasing outwards. In V1, there is a notable increase in variability near the gray-white matter surface. Additionally, variability is generally higher in V1 for 5% and 20% luminance contrast with respect to the other visual field maps. This is mainly driven by a lower BOLD response amplitude for these luminance contrasts compared to other visual field maps, as visible in Figure 3D.

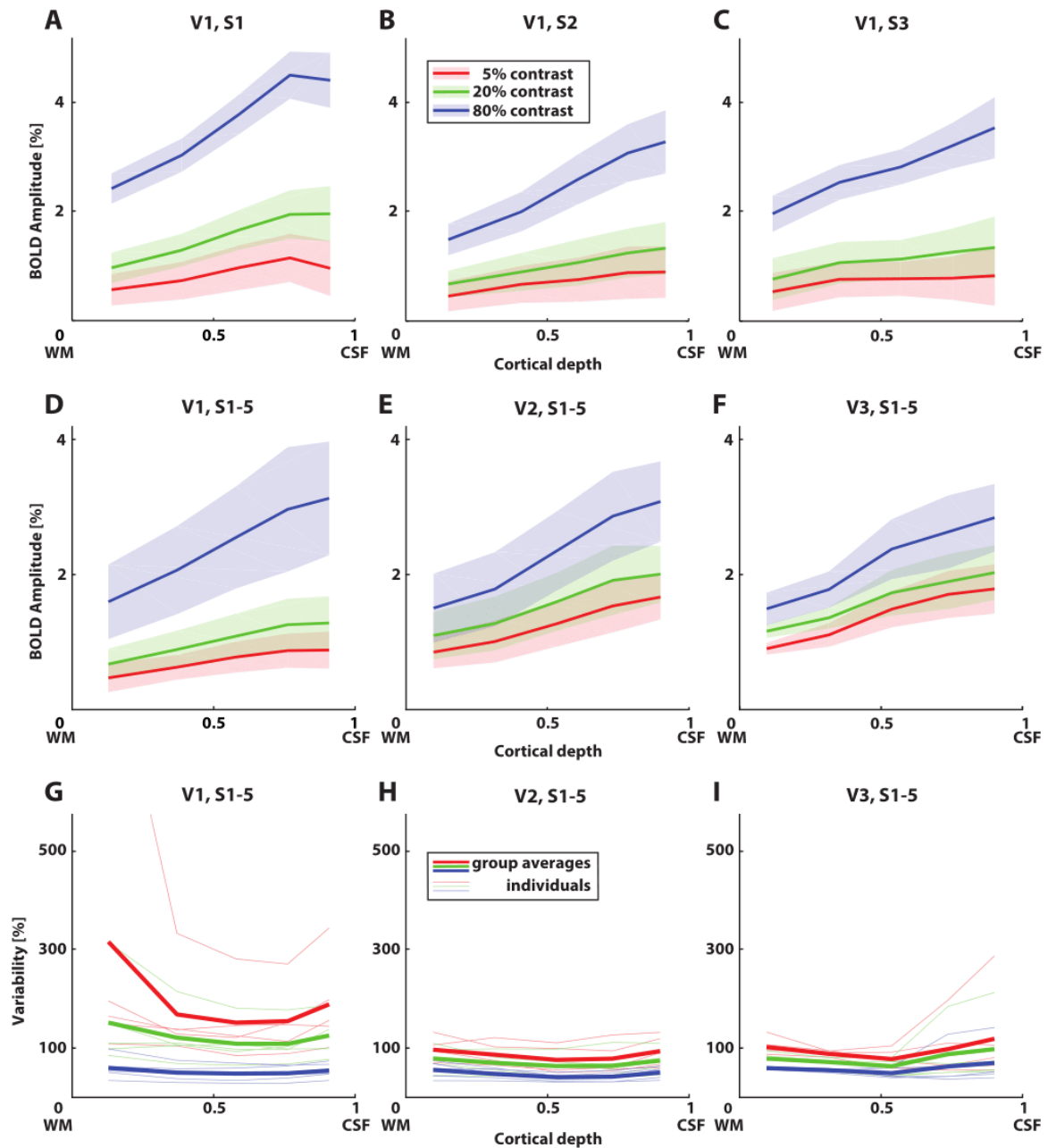


Figure 3: BOLD response amplitudes as a function of cortical depth and different luminance contrasts for the first session. A-C) BOLD response amplitudes across cortical depth for three example participants, for visual field map V1. Error regions represent ± 2 standard errors of the mean (95% confidence intervals) across repeated stimulus presentations for a region of interest, for each depth bin and luminance contrast. Panels for the other participants can be found in Figure S1. D-F) Group averages for visual field map V1, V2, and V3. BOLD response amplitudes increase with luminance contrast and towards the cortical surface. Error regions represent ± 2 standard errors (95% confidence intervals) of the mean response across depth between subjects. G-I) Variability (standard deviation across repeated stimulus presentations divided by the mean across voxels, in percentage) over depth for visual field map V1, V2, and V3. Thin lines denote individual subject. Thick lines denote group averages. Line colors correspond to luminance contrast, as in Figure 3A-F.

Linear systems theory captures differences in signal amplitudes

To assess the response linearity across cortical depth, we plotted all unique combinations of BOLD responses to two different luminance contrasts across cortical depth for each individual participant (Figure 4A-C; see Figure S2 for separate plots for each contrast pair). If responses to a higher luminance contrast ($H_{c1}(d)$) are a scaled version of a lower luminance contrast ($kH_{c1}(d)$, see equation 4), BOLD responses across cortical depth should fall on a straight line going through the origin with a slope equal to k . For V1, these linear fits explained an average variance of $r^2 = 0.99, 0.97$, and 0.99 for 5% to 20%, 5% to 80%, and 20% to 80% luminance contrast scaling respectively. For V2, the average explained variance was $r^2 = 0.99, 0.99$, and 0.98 , and $r^2 = 0.96, 0.99$, and 0.98 for V3.

To visualize the results in an alternative way, we plotted the averaged original responses ($H_{c1}(d)$) and averaged scaled responses ($kH_{c1}(d)$, equation 4; Figure 4D-F). See Table 1, left value in every cell, for all group estimates of k . The scaled responses were good predictors for responses at other contrasts. Both analyses indicate that the response amplitude across cortical depth elicited by one luminance contrast, was an excellent predictor for the response amplitude across cortical depth to another luminance contrast.

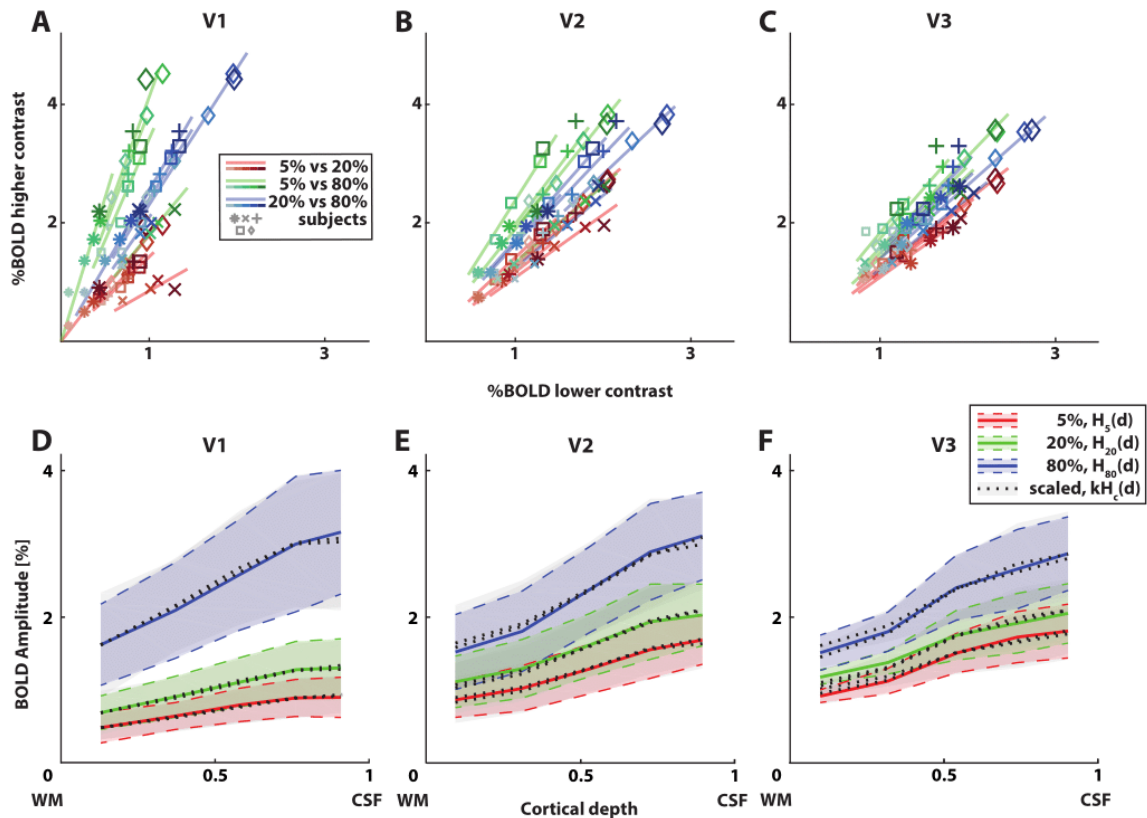


Figure 4: Linear systems theory captures differences in signal amplitude for the first session. A-C) BOLD response amplitude for individual participants (different marker symbols), for V1, V2, and V3. Different marker colors represent different depth bins. Each possible pair of two out of three luminance contrasts is plotted against each other (different colored lines), with %BOLD for the lower contrast on the x-axis, and for the higher contrast on the y-axis. Linear fits were forced to only fit a slope parameter, k from Equation 4. These fits explained 96-99% of variance. See Figure S2 for separate plots of each luminance contrast pair. D-F) Measured BOLD response across cortical depth for different luminance contrasts (colored lines) and visual field maps (different panels), overlaid with scaled responses to other

contrasts (dotted lines). Scaled responses represent the measured BOLD response across cortical depth for other contrasts, scaled by a scaling constant k (see Equation 4). These scaled responses explained 96-99% of variance. Error regions represent ± 2 standard errors (95% confidence intervals) of the mean response across depth between subjects. These are scaled by a factor k for the scaled responses.

Table 1: Group amplitude scaling factor k for all unique combinations of BOLD responses to two different luminance contrasts across cortical depth. The left value in each cell represents the scaling parameter for the first session, and the right value in each cell represents the scaling parameter for the second session. Separate rows: pairs of luminance contrasts. Separate columns: visual field maps.

k (session 1 / session 2)			
	V1	V2	V3
$H_{20}(d) = kH_5(d)$	1.50 / 1.61	1.24 / 1.26	1.16 / 1.15
$H_{80}(d) = kH_5(d)$	3.62 / 3.89	1.87 / 1.93	1.58 / 1.69
$H_{80}(d) = kH_{20}(d)$	2.38 / 2.33	1.50 / 1.53	1.37 / 1.47

Linear amplitude scaling generalizes across sessions

Next, we assessed whether these results generalized between sessions. In the second session, participants had to detect when the motion direction of the stimulus was identical on two consecutive presentations. The average discriminability (d') was 2.2, indicating a detection performance of well above chance level (d' of S1-5 were 2.6, 2.2, 2.1, 2.3, and 1.8 respectively, minimum d' for any individual run is 1.4).

Akin to our results above, the BOLD signal increased both as a function of contrast and cortical depth in V1-3 (Figure 5A-C). In the central depth bin of V1 (Figure 5A), the 5% luminance contrast elicited a response amplitude of 0.7% BOLD, whereas 20% and 80% luminance contrast elicited 1.1% BOLD and 2.5% BOLD respectively in the same depth bin. For V2 (Figure 5B), the 5%, 20%, and 80% luminance contrast elicited a response amplitude of 1.2, 1.5, and 2.3 % BOLD in the central depth bin respectively. For V3 (Figure 5C), these values were 1.3, 1.6, and 2.3% BOLD respectively.

Similar to Figure 4D-F, we plotted the averaged original responses ($H_{c1}(d)$) and averaged scaled responses ($kH_{c1}(d)$, equation 4; Figure 5D-F). See Table 1, right value in every cell, for all group estimates of k . The scaled responses were excellent predictors for responses at other contrasts. For V1, these scaled responses explained an average variance of $r^2 = 0.98$, 0.96, and 0.99 for 5% to 20%, 5% to 80%, and 20% to 80% luminance contrast scaling respectively. For V2, the average explained variance was $r^2 = 0.99$, 0.99, and 0.99, and $r^2 = 0.98$, 0.99, and 0.99 for V3.

Furthermore, we overlaid the responses across cortical depth to each session. These responses were near identical ($r^2 = 0.99$ for all contrasts and visual field maps), indicating that the reliability between sessions of luminance contrast responses across cortical depth is excellent.

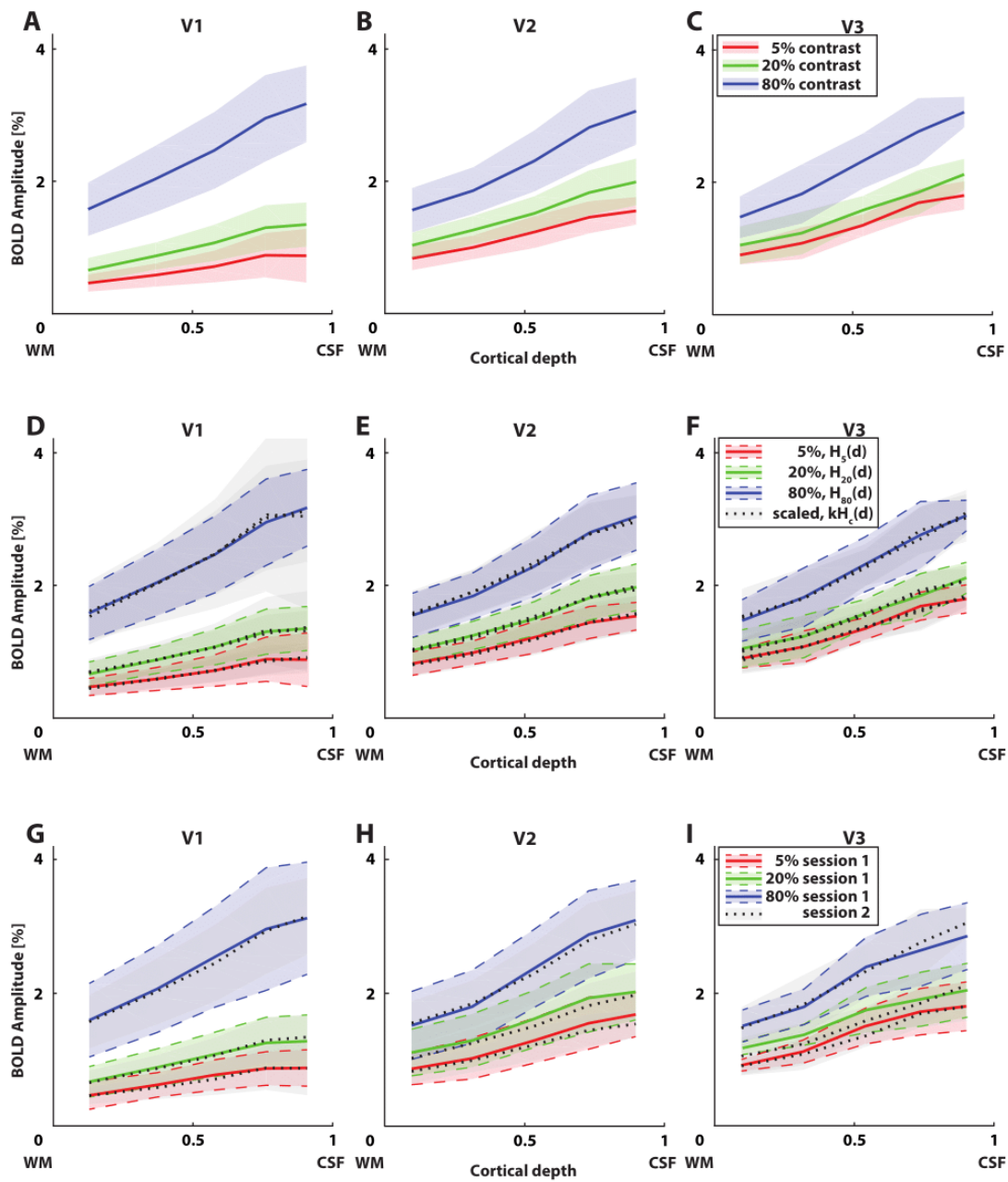


Figure 5: BOLD response amplitude and amplitude scaling for the second session are very similar to the first session. A-C) Group average BOLD response amplitudes across cortical depth of the second session for visual field map V1, V2, and V3. Error regions represent ± 2 standard errors (95% confidence intervals) of the mean response across depth between subjects. D-F) Measured BOLD response across cortical depth of the second session for different contrasts (colored lines) and visual field maps (different panels), overlaid with scaled responses to other contrasts (dashed lines). These scaled responses explained 96-99% of variance. Error regions represent ± 2 standard errors (95% confidence intervals) of the mean response across depth between subjects. These are scaled by a factor k for the scaled responses. G-I) Group average BOLD response amplitudes across cortical depth for the first session (solid lines) and second session (dotted lines, grayscale). Error regions represent ± 2 standard errors (95% confidence intervals) of the mean response across depth between subjects. Responses for both sessions matched almost perfectly (explained variance 99%).

Discussion

We assessed whether the scaling assumption for a linear system holds for BOLD amplitude across cortical depth. We evaluated BOLD fMRI responses across cortical depth elicited by viewing moving sinewave gratings with 5%, 20%, and 80% luminance contrast. We find that BOLD responses vary as a function of both luminance contrast and cortical depth. Additionally, we find that the variability of the BOLD response amplitude decreases with increasing luminance contrast, and that variability is highest in V1. In particular, we find that scaled BOLD responses across cortical depth, elicited by viewing one luminance contrast, are excellent predictors (average explained variance $r^2 = 0.96-0.99$) for responses across cortical depth to another luminance contrast, supporting the validity of the amplitude scaling assumption for BOLD amplitude across cortical depth. We do not find differences between scanning sessions, indicating that the robustness of the amplitude scaling assumption for the tested visual stimulus across cortical depth is stable over time.

Variability across cortical depth decreased with increasing luminance contrast, with 5% luminance contrast showing the highest variability across cortical depth for all visual field maps. This can be attributed to consistently lower signal amplitude than for other luminance contrasts, with comparable variability (see Figure 3A-C, Figure S1). Generally, variability showed a U-shaped profile across cortical depth, being lowest around the central depth bins and increasing towards the WM/CSF and WM/GM borders (see Figure 3G-I). However, as physiological and thermal noise may have different layer dependence, variability profiles across depth and the specific values measured here are likely to vary with parameters such as functional resolution, distance of the measured tissue to the radio frequency coils, and task-related signal amplitude.

Several recent studies have investigated the laminar response profiles focusing on the underlying neurovascular coupling in humans (De Martino et al., 2013; Herman, Sangahalli, Blumenfeld, Rothman, & Hyder, 2013; Huber, Goense, et al., 2014; Huber et al., 2015; Kemper et al., 2015; Koopmans, Barth, & Norris, 2010; Koopmans et al., 2011, 2012; Olman et al., 2012; Polimeni et al., 2010; Ress, Glover, Liu, & Wandell, 2007; Siero et al., 2011; Xing, Yeh, Burns, & Shapley, 2012; Zimmermann et al., 2011); non-human primates (G. Chen et al., 2012; Goense & Logothetis, 2006; Goense, Merkle, & Logothetis, 2012; Goense, Zappe, & Logothetis, 2007; Smirnakis et al., 2007; Zappe, Pfeuffer, Merkle, Logothetis, & Goense, 2008); and other mammals (Harel, Lin, Moeller, Ugurbil, & Yacoub, 2006; Jin & Kim, 2008; Lu et al., 2004; Silva & Koretsky, 2002; Yang et al., 2002; Yu et al., 2012, 2014; Zhao, Wang, Hendrich, Ugurbil, & Kim, 2006). All these studies have focused on the feasibility of laminar imaging. In addition, a few studies have employed sub-millimeter fMRI for systems and cognitive neuroscience questions (Y. Chen et al., 2011; Cheng, Waggoner, & Tanaka, 2001; De Martino et al., 2015; Fracasso, Petridou, et al., 2016; Goodyear & Menon, 2001; Huber et al., 2015; Kok et al., 2016; Marquardt et al., 2018; Muckli et al., 2015; Smith & Muckli, 2010; Yacoub, Harel, & Ugurbil, 2008; Yacoub, Shmuel, Logothetis, & Ugurbil, 2007). However, these latter studies have largely avoided the interpretation of BOLD amplitude measures, as this type of measure is susceptible to blood pooling effects across cortical depth. Here we provide data for the usability of BOLD fMRI amplitude measurements across cortical depth and the amplitude linearity assumption that underlies many fMRI analyses.

Here we used a T2*-weighted, gradient-echo (GRE) based 3D-EPI acquisition to collect the functional data. This type of acquisition is sensitive to the microvasculature, but also to larger vessels (macrovasculature; e.g. draining veins) and is thus affected by blood-pooling effects across cortical depth. Therefore, a signal elicited at a deeper cortical depth affects the measured signal at more superficial cortical depths, which results in less laminar specificity and the commonly observed signal increase in that direction, also found in this study. These effects could be corrected for in the analysis,

for instance by implementing a spatial correction approach as proposed by Markuerkiaga and colleagues (Markuerkiaga, Barth, & Norris, 2016), Marquardt and colleagues (Marquardt et al., 2018), or potentially by implementing more elaborate models of BOLD at different cortical depths that better capture general spatiotemporal properties of the hemodynamic signal, and the dynamics of capillary, arterial, and venous effects (Aquino, Robinson, Schira, & Breakspear, 2014; Aquino, Schira, Robinson, Drysdale, & Breakspear, 2012; Boas et al., 2008; Heinze et al., 2016; Puckett et al., 2016; Uludağ & Blinder, 2018) with respect to more traditional hemodynamic models (Buxton, Wong, & Frank, 1998; Klaas Enno Stephan, Weiskopf, Drysdale, Robinson, & Friston, 2007). We observed a relative decrease in BOLD amplitude for the most superficial depth bin in several visual field maps and for several luminance contrasts. These could be due to partial volume artifacts, and because the microvasculature is less dense near the cortical surface (Duvernoy et al., 1981).

One could argue that the increase in BOLD amplitude towards the cortical surface overshadows any cortical depth-dependent specificity in sub-millimeter GRE-based fMRI, i.e. the depth dependent signal may arise from partial voluming of the larger vessels at superficial depths only and signals may decrease as a function of the distance from these depths. However, it has been shown that there is sufficient specificity present in depth-dependent GRE acquisitions to measure different signals across the cortical depth. Biophysical models show that in the worst-case scenario, extravascular contamination from the veins at the pial surface falls off four-fold at a distance of half the vessel diameter, thus rapidly decreasing when moving away from the cortical surface (Ogawa et al., 1993). Additionally, at very high resolutions it is possible to isolate signals from middle layers from those at the pial surface (Fracasso, Luijten, Dumoulin, & Petridou, 2017). Furthermore, several studies using GRE-BOLD acquisitions and advanced analysis methods, have shown cortical depth-dependent modulations; of population receptive field size (Dumoulin & Wandell, 2008; Fracasso, Petridou, et al., 2016); with attention (Klein, Fracasso, Dijk, et al., 2018); with the absence or presence of illusory contours (Kok et al., 2016); and with contextual feedback (Muckli et al., 2015).

It is possible that the different vascular compartments over cortical depth have different (non)linear contributions to the measured BOLD signal at different luminance contrasts, e.g. nonlinear for the macrovasculature (draining veins), and linear for the microvasculature. We speculate that given the sensitivity of GRE-BOLD fMRI to the microvasculature, one would expect that nonlinearities over cortical depth resulting from the macrovasculature would have been detected here. We speculate that an increase in spatial resolution would not be expected to yield considerably different results. One could also argue that the microvasculature can exhibit nonlinearities, while the macrovasculature exhibits linear contributions to BOLD signal amplitude over cortical depth. However, if this were the case, GRE-BOLD fMRI would be able to pick up on nonlinearities in the microvasculature, especially closer to the gray-white matter surface as the capillary density is high at that compartment (Duvernoy et al., 1981). These would be detectable as nonlinearities at deeper and intermediate cortical depths, as compared to superficial depths, as these are most contaminated by macrovascular contributions. The third option would be that both the macrovascular and microvascular contributions are nonlinear but cancel each other out (near) perfectly. In this case, it would be hard to separate these contributions using GRE-BOLD fMRI. However, this would mean that linearity can still be assumed for most practical applications. All in all, linearity is not a feature that is only expected of GRE-BOLD fMRI, but also for other acquisition sequences at sub-millimeter resolutions, e.g. spin echo-based acquisitions, 3D-GRASE (Feinberg & Günther, 2009), and VASO (Huber et al., 2015, 2017; Jin & Kim, 2008). If anything, it is expected that GRE-BOLD fMRI is most sensitive to nonlinear macrovascular contributions.

Although the explained variance for the amplitude scaling is extremely high, there are minor deviations from linearity. These deviations are also apparent in Figure 4A-F, and Figure 5D-F. The deviations from linearity are more apparent at the highest luminance contrast, hinting at a potential increase in nonlinearity near the higher end of stimulus parameter space.

For a more complete evaluation of linear systems theory for BOLD amplitude across cortical depth in the visual domain, stimuli varying in high and other low-level domains such as spatial frequency, as well as the temporal additivity assumption for a linear system should also be investigated. However, the current stimuli span a wide range of stimulus energy, also using luminance contrasts at the edge of parameter space (5% and 80%). Thus, if the BOLD amplitude across cortical depth were nonlinearly scaled between different stimulus energy, we would have been able to capture this. Moreover, contrast manipulations are frequently used in the visual neuroscience literature, and were originally used for the assessment of the scaling assumption at supra-millimeter resolutions (Boynton et al., 1999, 1996, 2012). All in all, our results can be generalized for the visual domain along different contrast levels, while the scaling assumption remains to be validated for other modalities and measurements of contrast energy. Our data do not allow for the investigation of different contributions to the generation of the BOLD signal, so neuronal to vascular and vascular to BOLD contributions cannot be disentangled with the current experimental design. Additionally, because of the currently used pooling of large numbers of voxels using a region of interest-based approach, we cannot exclude that local pockets of nonlinearity might be observed within a region of interest (here: visual field map). However, our results do provide evidence for the linearity of BOLD amplitude across cortical depth as a function of luminance contrast for region of interest-based approaches. The temporal additivity assumption for a linear system was not currently assessed as the presently used volume acquisition time (4 s) results in too sparse a sampling of the fMRI time-series to assess this property. At the current resolution (0.7 mm isotropic voxels), this is the fastest our system could collect data. Thus, only one out of two assumptions for a linear system across cortical depth has been evaluated so far.

To our knowledge, response amplitude to different luminance contrasts is only assessed by one other laminar fMRI publication to date. In that study, Marquardt and colleagues (Marquardt et al., 2018) assess the cortical depth profiles of luminance contrast responses, but do not assess luminance contrast linearity of BOLD amplitude across cortical depth. Instead, they propose a novel spatial deconvolution approach to correct for the directional component of the intracortical vasculature (Marquardt et al., 2018). The range of their measured signal amplitudes is similar to the current findings. They also use a GRE-based EPI sequence with the same resolution, albeit with a shorter TR (2.94 s versus 4 s here) and more coverage (52 slices versus 34 slices in the present study). Upon simple visual inspection, both their deconvolved and original results are likely to fit with the current findings, providing further evidence that the scaling assumption for a linear system holds across cortical depth for luminance contrast manipulations.

We do not find any evidence for significant changes in signal amplitude across cortical depth between sessions, even though the second session included a stimulus-related task. This appears to be in contradiction with previous studies that have shown attention-related differences for supra-millimeter fMRI (see e.g., O'craven, Rosen, Kwong, Treisman, & Savoy, 1997; Schwartz et al., 2005); across cortical depth in e.g. population receptive field center positions (Klein, Fracasso, Dijk, et al., 2018); or suggest such differences due to e.g. a lack of feedforward input in patients with macular degeneration (Masuda et al., 2008). Potential explanations for the apparent lack of task-driven changes in our study are two-fold. First, evidence suggests that attentional signal modulation in early visual cortex is reduced with respect to extrastriate visual field maps (Clark & Hillyard, 1996; Klein,

Fracasso, Dijk, et al., 2018; Moran & Desimone, 1985; O’craven et al., 1997; Somers, Dale, Seiffert, & Tootell, 1999). Moreover, Klein et al (Klein, Fracasso, Dijk, et al., 2018) focused on measures that do not depend on signal amplitudes. When comparing signal amplitudes, they found little modulation of BOLD amplitude between different attention conditions. Additionally, the one-back task used in the present study required very little attentional resources to carry out correctly as the events were sparse, and the stimulus was very salient. We therefore argue that attentional modulation did not play a role in the present study.

Conclusion

We provide evidence that the scaling assumption for linear systems theory can be met for BOLD amplitude measures across cortical depth, i.e. responses scale with luminance contrast, and this amplitude scaling is identical across cortical depth. Thus, the BOLD linearity assumption for amplitude scaling commonly employed for conventional fMRI analysis, extends to the cortical depth domain for luminance contrast manipulations.

Supplementary Information

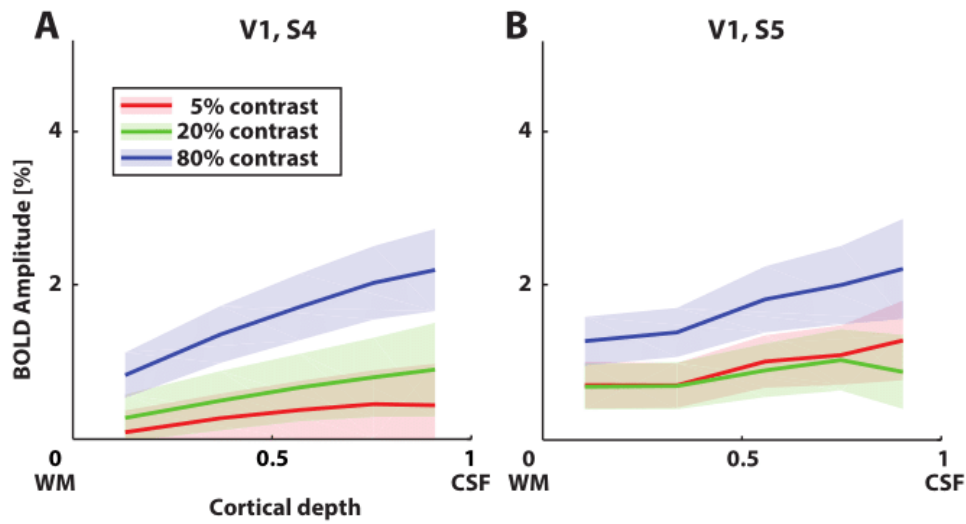


Figure S 1: BOLD response amplitudes as a function of cortical depth and different luminance contrasts for the first session. BOLD response amplitudes across cortical depth for the two participants not shown in Figure 3A-C, for visual field map V1. Error regions represent 95% confidence intervals of the mean across repeated stimulus presentations in a region of interest, for each depth bin and luminance contrast.

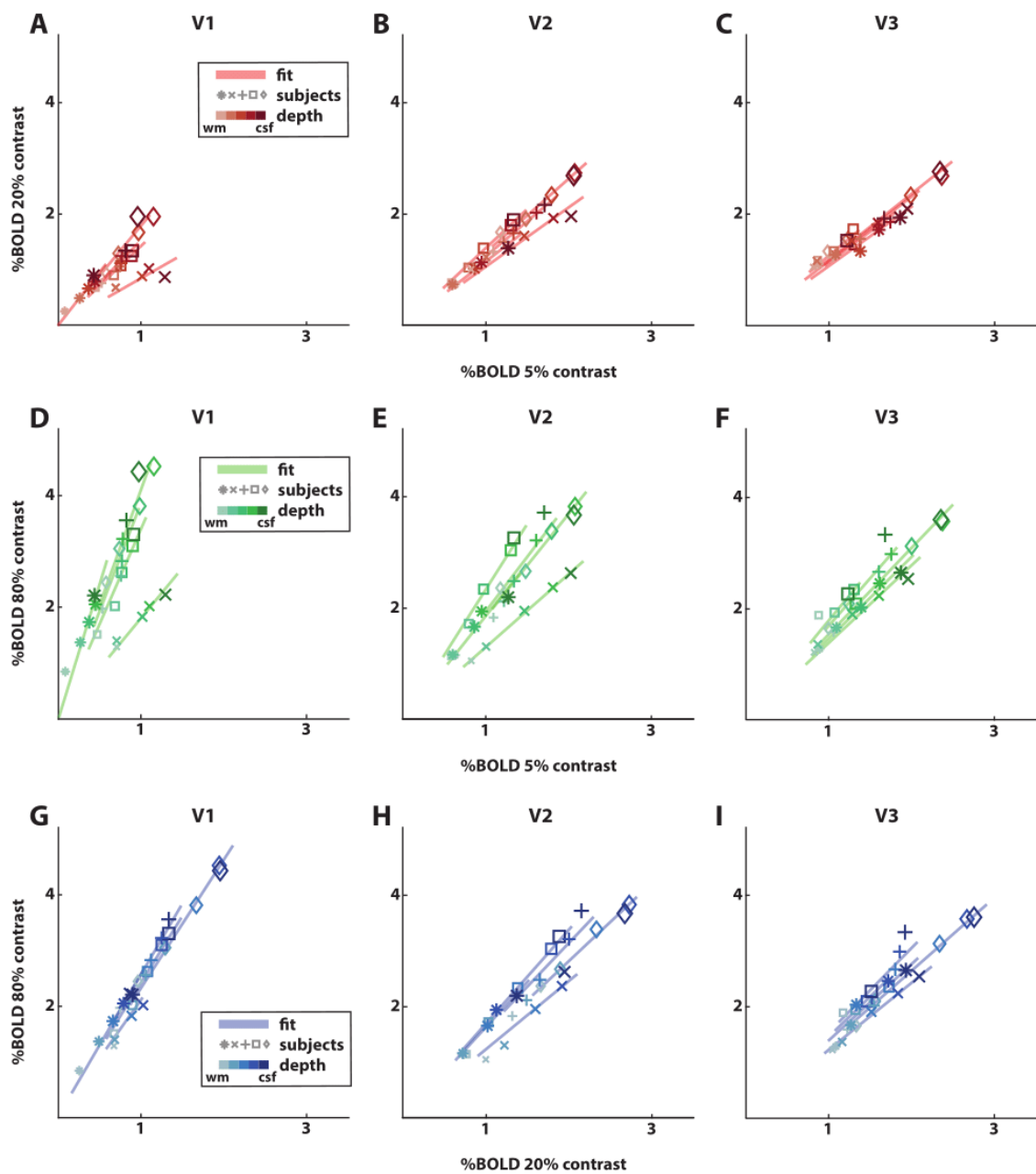


Figure S 2: BOLD response amplitude at each depth bin for every combination of two luminance contrast presentations, for each participant (different marker shapes), with best linear fit line. Different cortical depths are denoted as different marker sizes and colors, as indicated in the appropriate legends. N.B. Combining each column of panels in one figure, results in Figures 4A-C. A-C) BOLD response amplitudes for 5% luminance contrast (x-axis) plotted against the BOLD response amplitude for 20% luminance contrast (y-axis) for V1-V3. D-F) BOLD response amplitudes for 5% luminance contrast (x-axis) plotted against the BOLD response amplitude for 80% luminance contrast (y-axis) for V1-V3. G-I) BOLD response amplitudes for 20% luminance contrast (x-axis) plotted against the BOLD response amplitude for 80% luminance contrast (y-axis) for V1-V3.

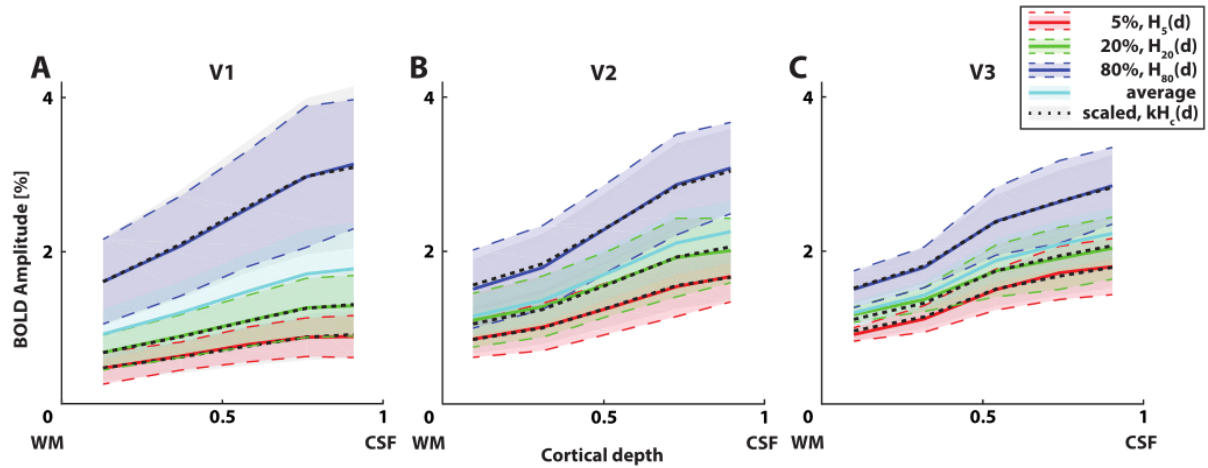


Figure S 3: Measured BOLD response amplitude across cortical depth for different luminance contrasts for session 1 (red, green, and dark blue solid lines), and BOLD response amplitude across cortical depth averaged over all luminance contrasts for session 1 (light blue line). Dashed black lines represent the average luminance contrast response (light blue line), scaled by a factor k to best fit each luminance contrast response. These scaled responses explained 99% of variance. Error regions represent 95% confidence intervals of the mean response across depth between subjects. Different panels display different visual field maps.

Chapter 3

Evaluating temporal additivity for laminar fMRI

van Dijk, J.A., Fracasso, A., Petridou, N., & Dumoulin, S.O., Evaluating temporal additivity for laminar fMRI (in preparation)

Acknowledgement of author contributions

JAvD, AF, and SOD designed the experiment. JAvD and AF collected and analyzed the data. All authors contributed to and reviewed the main manuscript text. JAvD prepared all figures. SOD and NP provided general supervision and guidance throughout.

ABSTRACT

Advancements in ultra-high field (7 T and higher) magnetic resonance (MRI) scanners have made it possible to investigate both the structure and function of the human brain at a sub-millimeter scale. As neuronal feedforward and feedback information arrives in different layers, sub-millimeter functional MRI has the potential to uncover information processing between cortical microcircuits, across cortical depth. For nearly all fMRI analyses, one of the main assumptions is that the relationship between local neuronal activity and the blood oxygenation level dependent (BOLD) signal can be described as following linear systems theory. Directional blood pooling across cortical depth, stemming from the anatomy of the cortical vasculature may affect BOLD response linearity, complicating analysis and interpretation. Here we assess whether the temporal additivity assumption of linear systems theory holds for laminar fMRI. We find that BOLD response predictions are constant across cortical depth in V1, V2, and V3. Our results suggest that the temporal additivity assumption for linear systems theory holds for laminar fMRI. Together with our previous work, we show that BOLD response linearity holds across cortical depth for sub-millimeter gradient-echo BOLD fMRI in the early visual cortex.

Introduction

Magnetic resonance imaging (MRI) is one of the dominant methods to non-invasively study the structure and function of the (human) brain. Over the past two decades, this imaging method has seen rapid developments, resulting in ever-increasing technical possibilities and applications. With the advent of ultra-high (7 Tesla and higher) field MRI scanners, it has become possible to investigate both structure and function of the human brain at a sub-millimeter resolution. As the human cortex has a thickness of 1.5 - 4 mm (Fischl & Dale, 1999) and is comprised of six anatomically (and functionally) distinct laminae or layers (Brodmann, 1903, 1909; Gennari, 1782; C. Vogt & Vogt, 1919; O. Vogt, 1910), sub-millimeter resolutions enable the investigation of cortical depth-dependent signals reflecting contributions from different cortical layers (also known as laminar MRI). Sub-millimeter functional MRI (fMRI) promises to complement anatomical measurements across cortical layers, adding valuable information about fundamental processing in cortical microcircuits, and functional properties that reflect feedforward and feedback interactions within the thickness of the cortex (De Martino et al., 2018; Dumoulin et al., 2018; Lawrence et al., 2017; Natalia Petridou & Siero, 2017; Self & Roelfsema, 2017; Self et al., 2019; K. E. Stephan et al., 2019).

These promises, however, do not come without challenges (Dumoulin et al., 2018; Kashyap et al., 2017; Yacoub et al., 2018). One dominant challenge of laminar fMRI relates to the organization of the cortical vasculature across cortical depth. Blood flows from pial and intracortical arteries and arterioles to the capillary bed that directly interfaces with neuronal tissue, and is then drained via venules and intracortical veins to larger veins at the cortical surface (Duvernoy et al., 1981; Turner, 2002). This results in a directional blood collection -also called blood pooling- across cortical depth towards the cortical surface. Therefore, the fMRI signal at a specific cortical depth does not only consist of measurements of the hemodynamic consequences of local neuronal activity (Heeger et al., 2000; Logothetis, 2002), but also of hemodynamic changes at underlying cortical depths, closer to the gray-white matter surface. The weighting of these two factors -local neuronal activity in micro vessels, and draining effects from micro- and macrovasculature- is dependent upon the specific acquisition methods used (S. G. Kim & Ogawa, 2012; Natalia Petridou & Siero, 2017). Detailed models of the vascular architecture across cortical depth (see e.g. Boas et al., 2008; Reichold et al., 2009) additionally show that blood pooling effects might differentially affect blood oxygenation-dependent (BOLD) signals at deeper cortical depths compared to ones closer to the cortical surface (Heinzle et al., 2016).

While draining effects across cortical depth pose a challenge to laminar fMRI, these effects are largely irrelevant for fMRI at conventional resolutions ($>1 \text{ mm}^3$), as one voxel at these resolutions typically spans most of the thickness of the cortex. One of the major assumptions underlying nearly all fMRI data-analysis techniques, is that fMRI responses are linearly proportional to a local average neuronal activity over a period of time (Boynton et al., 1996). This assumption largely holds for conventional-resolution fMRI, provided that the stimuli used are within a defined range of stimulus parameters that is commonly used in neuroimaging experiments, see e.g. (Boynton et al., 1996, 2012; Cohen, 1997; Friston et al., 1994; Heeger et al., 2000; Miezin et al., 2000); for nonlinearities, mostly found in event-related designs and very short stimulus presentations, see e.g. (Birn et al., 2001; Kershaw et al., 2001; Pfeuffer et al., 2003; Robson et al., 1998; Soltysik et al., 2004; Vazquez & Noll, 1998; Zhang et al., 2008). However, because of draining effects across cortical depth, laminar BOLD fMRI might violate linearity assumptions, as different cortical depth bins are not independent.

For BOLD response linearity to hold, two assumptions must be met: linear scaling, and temporal additivity. The linear scaling assumption across cortical depth using gradient echo (GRE) BOLD in the visual cortex has previously been confirmed to hold (van Dijk et al., submitted), but the temporal additivity assumption remains yet to be evaluated. Here we test whether the temporal additivity assumption for a linear system holds in human visual cortex using GRE-BOLD at 7T. We thus seek to complete the evaluation of the BOLD amplitude linearity assumptions across cortical depth.

If we define a system with a hemodynamic transform L , neuronal response over time $n(t)$, and hemodynamic response $H(t)$ as output:

$$L[n(t)] = H(t) \quad (\text{Equation 1})$$

For the property of temporal additivity to hold, the response to the sum of two inputs should be equal to the sum of the responses to each separate input. Given two inputs $n_1(t)$ and $n_2(t)$, this is formalized as:

$$L[n_1(t) + n_2(t)] = L[n_1(t)] + L[n_2(t)] \quad (\text{Equation 2})$$

The easiest way to visualize this property, is by imagining two neuronal responses that are elicited close in time to each other, such that the hemodynamic response associated with the first neuronal response has not yet returned to baseline when that the second neuronal response is elicited. The temporal additivity assumption then states that the second hemodynamic response -resulting from the second neuronal response- simply adds to the first hemodynamic response, without interacting in any way (Boynton et al., 2012). On a sub-millimeter level, the hemodynamic response at a given depth d does not only depend on the local neuronal response, but also on responses at cortical depths closer to the gray-white matter border due to blood pooling effects. Thus, the temporal additivity assumption at cortical depth d can be formalized as:

$$\begin{aligned} L[n_1(t) + n_2(t)]_d + \sum_{i=d_0}^{d-1} w_i L[n_1(t) + n_2(t)]_i \\ = L[n_1(t)]_d + L[n_2(t)]_d + \sum_{i=d_0}^{d-1} v_i L[n_1(t)]_i + \sum_{i=d_0}^{d-1} u_i L[n_2(t)]_i \end{aligned}$$

(Equation 3)

Then, by substituting Equation 1 for legibility, and rearranging:

$$H_{1,2}(t)_d = H_1(t)_d + H_2(t)_d - \sum_{i=d_0}^{d-1} w_i H_{1,2}(t)_i + \sum_{i=d_0}^{d-1} v_i H_1(t)_i + \sum_{i=d_0}^{d-1} u_i H_2(t)_i$$

(Equation 4)

Where $H_{1,2}(t)_d$ is the hemodynamic response over time to a combination of stimulus 1 and 2 at depth d ; $H_1(t)_i$ and $H_2(t)_i$ are the hemodynamic responses over time to stimulus 1 and 2 respectively at depth d . The factor $\sum_{i=d_0}^{d-1} w_i H_{1,2}(t)_i$ represents the draining contributions from the combined hemodynamic response $H_{1,2}(t)_i$ at all cortical depths i between the gray-white matter border d_0 and the depth bin directly below cortical depth d . These responses are weighted by a depth-dependent factor w_i . The factors $\sum_{i=d_0}^{d-1} v_i H_1(t)_i$, and $\sum_{i=d_0}^{d-1} u_i H_2(t)_i$ represent the draining contributions as described above, but for $H_1(t)_i$ and $H_2(t)_i$ respectively and weighted by factors v_i and u_i respectively. The weighting factors w_i , v_i or u_i represent an estimation of the draining of altered deoxyhemoglobin content and increased blood pooling from lower layers (Marquardt et al., 2018). Both the hemodynamic response to two combined responses, and two separate responses, are thus

dependent not only on local neuronal activity, but also on draining from deeper cortical depths. These draining effects might not be identical for responses to the combination of two stimuli, versus the two stimulus responses separately, and thus violate the temporal additivity assumption at a given cortical depth.

For the temporal additivity assumption across cortical depth to hold, BOLD responses to longer stimulus presentation durations should be predicted by a temporal summation of the BOLD responses to shorter stimulus presentation durations. This should hold equally well at all cortical depths. Note that this does not imply that the predicted responses at a given depth need to exactly match the corresponding measured response, but merely that the goodness of fit of these predictions is constant across cortical depth. Indeed, previous research has shown that the predictions built from shifted and summed responses, do not correspond one-to-one to the measured responses (see e.g. Boynton et al., 1996).

Here we test whether the temporal additivity assumption for a linear system holds in human visual cortex for BOLD amplitude across cortical depth, using GRE-BOLD. We thus seek to extend the BOLD linearity assumption of temporal additivity to the cortical depth domain. We used three different stimulus presentation durations (2.6, 5.2, and 10.4 s, sinewave gratings at 50% luminance contrast) to elicit neuronal responses in striate and extrastriate cortex. For temporal additivity across cortical depth to hold, the quality of the fits of shifted and summed BOLD responses on measured BOLD responses should be consistent across cortical depth.

We find that peak response amplitudes for each stimulus presentation duration increase towards the cortical surface. Moreover, we find larger response amplitudes for longer stimulus presentations. Predictions of responses to longer stimulus presentation durations acquired by shifting and adding responses to shorter stimulus presentation durations, showed good fit quality, and was consistent across cortical depth. In line with previous research, we find that the predictions from the shortest (2.6 s) stimulus presentation duration generally had lower fit quality overall than the medium (5.2 s) stimulus presentation duration. We conclude that the temporal additivity assumption holds across cortical depth for laminar GRE-BOLD fMRI in the visual cortex.

Methods

Participants

Five subjects (all male, age range 25-45) participated in the experiment. All participants were familiar with the MRI environment and had participated in previous experiments. They had normal or corrected-to-normal visual acuity. One subject was excluded because of poor signal amplitude. Signed informed consent was acquired from all participants. All experimental procedures were conducted in accordance to the Declaration of Helsinki and approved by the ethics committee of the University Medical Center Utrecht.

Stimuli

Stimuli were presented on a 32-inch LCD screen, specifically designed for use in an MRI environment (Cambridge Research Systems, 2012). The screen resolution was 1920 x 1080 pixels, with a screen size of 69.8 x 39.3 cm, a refresh rate of 120 Hz, and a built-in linear luminance look-up table. The display was positioned at the far end of the bore and viewed via a mirror positioned in the MRI head coil. The total viewing distance was 220 cm. The total stimulus diameter subtended 10.2 degrees of visual angle (deg).

All stimuli were generated in MATLAB (Mathworks; 2015b) using the Psychophysics Toolbox (Brainard, 1997; Pelli, 1997). A fixation dot (0.1 deg in diameter) was presented at all times in the middle of the screen. This fixation dot was either red or green, with a color change occurring on average every 1.5 s. The stimuli consisted of sinewave gratings (0.5 cycles per degree, luminance contrast 50%) oriented in any of 4 possible directions (0-135 deg in 45 deg steps; similar to (Masuda et al., 2010), and previous work from our group), restricted by a 5.1 deg radius circular aperture. The rest of the screen displayed mean luminance at all times. The gratings were moving perpendicular to the orientation of the bars at 1.76 deg per second. Movement was either towards the left or towards the right edge of the screen.

Stimuli were presented for 2.6 s, 5.2 s, and 10.4 s blocks, counterbalanced in order, and interleaved with on average 15.6 s-long mean luminance blocks. During stimulus presentation, stimuli were shown each time for 700 ms, followed by 167 ms of mean luminance. No two subsequent stimulus presentations had the same motion direction or orientation. On half the stimulus blocks, stimulus onsets were jittered by 1.3 s. A total of 12 stimulus blocks (four of each duration) were presented per run. Each run started with one block of mean luminance.

Task

All participants completed one session of 8 runs. Participants were instructed to fixate on the fixation dot in the middle of the screen and report any color change of this fixation dot by means of a button press. Average fixation task performance was 78 % correct (range 49-100 % for individual runs).

Visual field map definition

Visual field map definitions were acquired in separate scanning sessions for each participant. Procedures for this were near-identical to previous studies, e.g. (Dumoulin & Wandell, 2008). Details for the visual field map definitions for these specific subjects can be found in van Dijk et al (submitted). All visual field maps were restricted to 5.1 degrees eccentricity. Only V1, V2, and V3 were included in this study (see Figure 1A for an example of V1).

MRI and fMRI acquisition

High resolution anatomical and functional data were acquired using a Philips Achieva 7 T scanner. with a maximum gradient strength of 40mT/m and a slew rate of 200 T/m/s (Philips, Best, The Netherlands). A dual-channel volume transmit coil was used for all scans (Nova Medical, MA, USA). A 32-channel

receive head coil (Nova Medical, MA, USA) was used for all anatomical scans, and two custom-built 16-channel high-density surface receive arrays were used for all functional scans (Petridou et al., 2013; MRCoils BV). These surface arrays were positioned adjacent so that the two arrays touched each other lengthwise but did not overlap. Participants were positioned such that their external occipital protuberance was approximately aligned with the center between the arrays, at the height of the most distal receive elements from the isocenter.

Anatomical data were acquired using an MP2RAGE sequence (Marques et al., 2010). Sequence parameters were: $T11 = 800$ ms, $T12 = 2700$ ms, $TRMP2RAGE = 5500$ ms, $TR/TE = 6.2/2.3$ ms, flip angle $\alpha1 = 7^\circ$, and $\alpha2 = 5^\circ$, bandwidth = 403.7 Hz/pixel, acceleration factor using SENSE encoding = 3.5×1.3 (RL and AP respectively), resolution = 0.64mm isotropic, whole-brain coverage, with a total scan time of 9 min 57 s.

Functional data were acquired using a $T2^*$ -weighted 3-dimensional multi-shot EPI (3D- EPI, two shots per slice, 25 slices, 50 shots overall). The sequence parameters were: $TR/TE = 59/28$ ms, flip angle: 20° , acceleration factor using SENSE encoding: 2.9 (right-left) $\times 1.3$ (anterior-posterior), echo planar factor: 27, bandwidth (phase-encode): 702.4 Hz/pixel, voxel size = 0.80 mm isotropic, FOV = 126.3 (right-left) $\times 120$ (feet-head) $\times 20$ (anterior- posterior) mm, 25 coronal slices, and 10% oversampling in the slice direction. The volume repetition time was 2.6 s. Each functional run was 102 time frames (4 min 25.2 s) in duration. The acquisition volume orientation was parallel to the receive arrays.

For each functional run, we acquired an additional five volumes with reversed right-left phase-encoding. Reversing the phase-encoding direction ensured that these so-called ‘topup’ runs had the opposite geometrical distortions to the original volumes (Andersson et al., 2003). These topup runs were used in conjunction with the original data to estimate a nonlinear warp field to create a susceptibility distortion-free volume, which is the midpoint between the functional and topup data (Andersson et al., 2003). This undistorted volume then makes it possible to align the functional data to the subject anatomy more accurately, needed for region of interest definition and cortical depth-based analysis.

Pre-processing: functional data

Data processing was performed using AFNI (Cox, 1996) and MATLAB (Mathworks, version 2015b). First, a warp field to correct for susceptibility distortions was calculated using a nonlinear transformation, with the first five volumes of each of the functional and topup runs as input. Motion parameters within runs were estimated by aligning each volume within a run to the first volume of that run. Subsequently, motion parameters between runs were estimated by aligning the first volume of each run to the first volume of the first run using Fourier interpolation. Next, all runs were individually despiked, scaled, and detrended. Despiking was performed using the AFNI function 3dDespike. The scaling step entailed converting the time-series of each run to percentage BOLD. This was achieved by dividing the signal of each voxel by its temporal mean, multiplying that signal with 100, and subsequently subtracting 100 to ensure that the temporal mean of that voxel was zero percent signal change. For the detrending, the AFNI function 3dDetrend with up to a fourth-degree polynomial was used. These functional runs were then temporally resampled to 1.3 s timesteps using linear resampling.

Next, the motion estimates and warp field results were combined to calculate the mean EPI image, averaging over all warped and motion corrected volumes runs and collapsing over all time points. This mean EPI image was then registered to the anatomy using a multi-step procedure. First, the anatomy was restricted to roughly the occipital lobe. Next, the mean EPI image and anatomy were brought into the same space by aligning the center of mass of the anatomy to the mean EPI image. Then, the ‘Nudge

dataset' AFNI plugin was used to manually shift and rotate the mean EPI image to provide a good starting point for two automated registration steps. These registration steps both consisted of an affine transformation to further optimize the registration, using local Pearson correlation as cost function (Saad et al., 2010). The first transformation allowed for a maximum rotation and/or shift of 3 mm in any direction, while the second transformation allowed for a maximum rotation and/or shift of 1 mm. The transformation matrices of the manual step and the two affine transformations were combined into a single affine matrix. As a control, this matrix was then applied to the original mean EPI image. These results were then inspected for registration quality. Next, we applied the combined affine matrix and the warp field to all temporally resampled motion-corrected, despiked, scaled, and detrended runs individually to align these volumes to the registered mean EPI image. This was achieved using the AFNI function 3dNwarpApply with nearest neighbor interpolation. These registered, distortion-corrected volumes were then resampled to the anatomy, resulting in the registered time-series for each run. In total, the motion-corrected, despiked, detrended time-series were spatially resampled twice, resulting in the registered, topup-corrected time-series in anatomy space (Figure 1B).

Pre-processing: anatomical data

Gray/white matter classifications of the anatomical data were carried out using MIPAV (<http://mipav.cit.nih.gov/>) with the CBS-tools plugin (Bazin et al., 2007; www.nitrc.org/projects/cbs-tools/), and subsequently manually optimized in 3D Slicer (Fedorov et al., 2012). Based on these corrected volumes, volume-preserving distance maps between the gray-white matter (GM/WM) border and the gray matter-cerebrospinal fluid (GM/CSF) border were computed (Waehnert et al., 2014) in 6 level-set volumes, also using the MIPAV with the CBS-tools plugin. These level-sets were then projected on the distortion-corrected mean time-series for subsequent laminar analysis (Figure 1C).

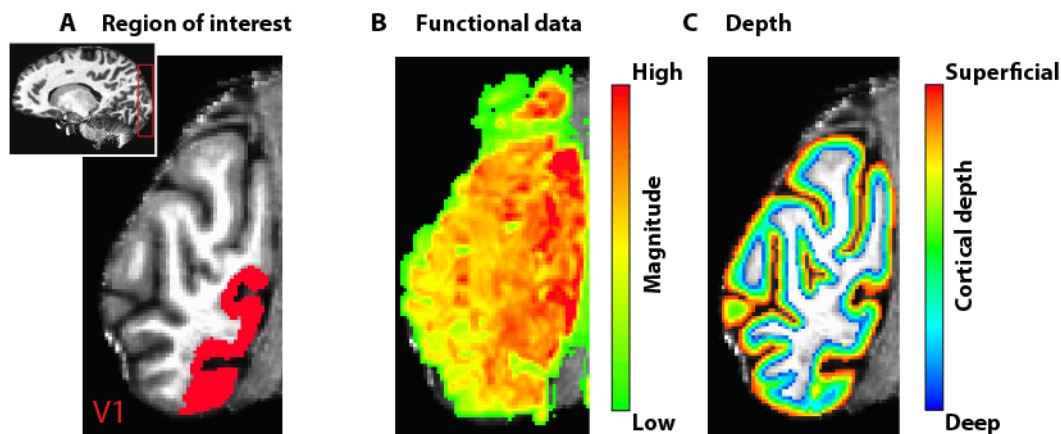


Figure 8: Processing steps. A) Example region of interest definition (V1) on a coronal anatomical slice. Inset: whole brain with coverage of functional acquisition (red box). B) Motion- and susceptibility-corrected functional data overlaid on the same anatomical slice as in A). C) Depth map overlaid on anatomical slice.

Analysis

Temporal response profiles at different cortical depths

For each participant we divided the distortion-corrected mean time-series into twelve blocks, each starting at stimulus onset. These blocks contained as many time points as the stimulus presentation duration (2.6, 5.2, or 10.4 s) plus a 15.6 s post-stimulus baseline. Blocks containing the same stimulus presentation duration were then averaged together. To assess the temporal responses at different

cortical depths, we divided the distance map (see Pre-processing: anatomical data) into 5 depth quantiles, spanning from the GM/WM to the GM/CSF border. Next, we selected voxels within each depth bin for each visual field map (V1, V2, and V3) and calculated the mean BOLD amplitude over time for each stimulus presentation duration, along with the 95% confidence interval of the variability between stimulus blocks of the same length.

Temporal additivity assessment

To assess the temporal additivity of BOLD responses for each visual field map at each depth bin, we generated predicted responses to longer stimulus presentations by temporally shifting the responses to shorter stimulus presentations, and subsequently adding this shifted response to the original response for the shorter stimulus (see e.g. Boynton et al., 1996). For example, temporally shifting a 2.6 s stimulus presentation response by 2.6 s, and subsequently adding this to the non-shifted 2.6 s response, created a predicted response to the 5.2 s stimulus presentation. Next, we estimated the goodness of fit of these predicted responses by calculating the Pearson correlation between the predictions and the original stimulus responses. We subsequently plotted the correlation at each depth for each of the three predictions. For temporal additivity across cortical depth to hold, the correlation between one stimulus presentation duration and longer one at a given cortical depth bin, should be constant over depth.

We repeated the above procedures at the group level, using between-participant 95% confidence intervals instead of between-stimulus repetitions as a measure of variability. We again calculated the temporally shifted responses to longer stimulus presentations and estimated the goodness of fit across cortical depth for each visual field map.

Results

Temporal response profiles increase with presentation duration and towards the cortical surface

For each subject, the maximum BOLD amplitude increased both as a function of stimulus presentation duration and cortical depth for all tested visual field maps (V1, V2, V3; see Figure 2A-C for V1 data of an example subject). For the example subject, peak amplitudes in V1 at deep, middle, and superficial cortical depths for the short (2.6 s), medium (5.2 s), and long (10.4 s) stimulus presentations were: 1.13, 1.34, 1.44 % BOLD (short); 1.42, 1.93, 2.38 % BOLD (medium); and 1.81, 2.24, 2.72 % BOLD (long). We observed similar patterns for the group averaged responses (Figure 2D-L). Group average peak amplitudes for V1 at deep, middle, and superficial cortical depth bins for the short (2.6 s) stimulus presentation duration were: 0.58, 0.86, and 0.98 % BOLD. For the medium (5.2 s) presentation duration, these numbers were: 0.85, 1.19, and 1.63 % BOLD respectively. Lastly, for the long (10.4 s) presentation duration, the peak amplitudes were: 1.32, 2.13, and 2.54 % BOLD. For V2, the respective peak amplitudes were 0.54, 0.88, and 1.22 % BOLD (short presentation); 0.88, 1.27, 1.76 % BOLD (medium presentation); and 1.25, 1.89, and 2.30 % BOLD (long presentation). For V3, peak amplitudes at deep, middle, and superficial cortical depth bins were 0.62, 1.05, and 1.31 % BOLD (short presentation); 0.87, 1.16, and 2.59 % BOLD (medium presentation); and 1.22, 1.72, and 2.96 % BOLD. The consistent increase towards the cortical surface and with visual hierarchy is in line with previous literature (see e.g. Kim and Ress, 2017; Muckli et al., 2015; Polimeni et al., 2010; Siero et al., 2011). Moreover, response amplitude increased with presentation durations, likewise in line with previous research (e.g. Boynton et al., 1996).

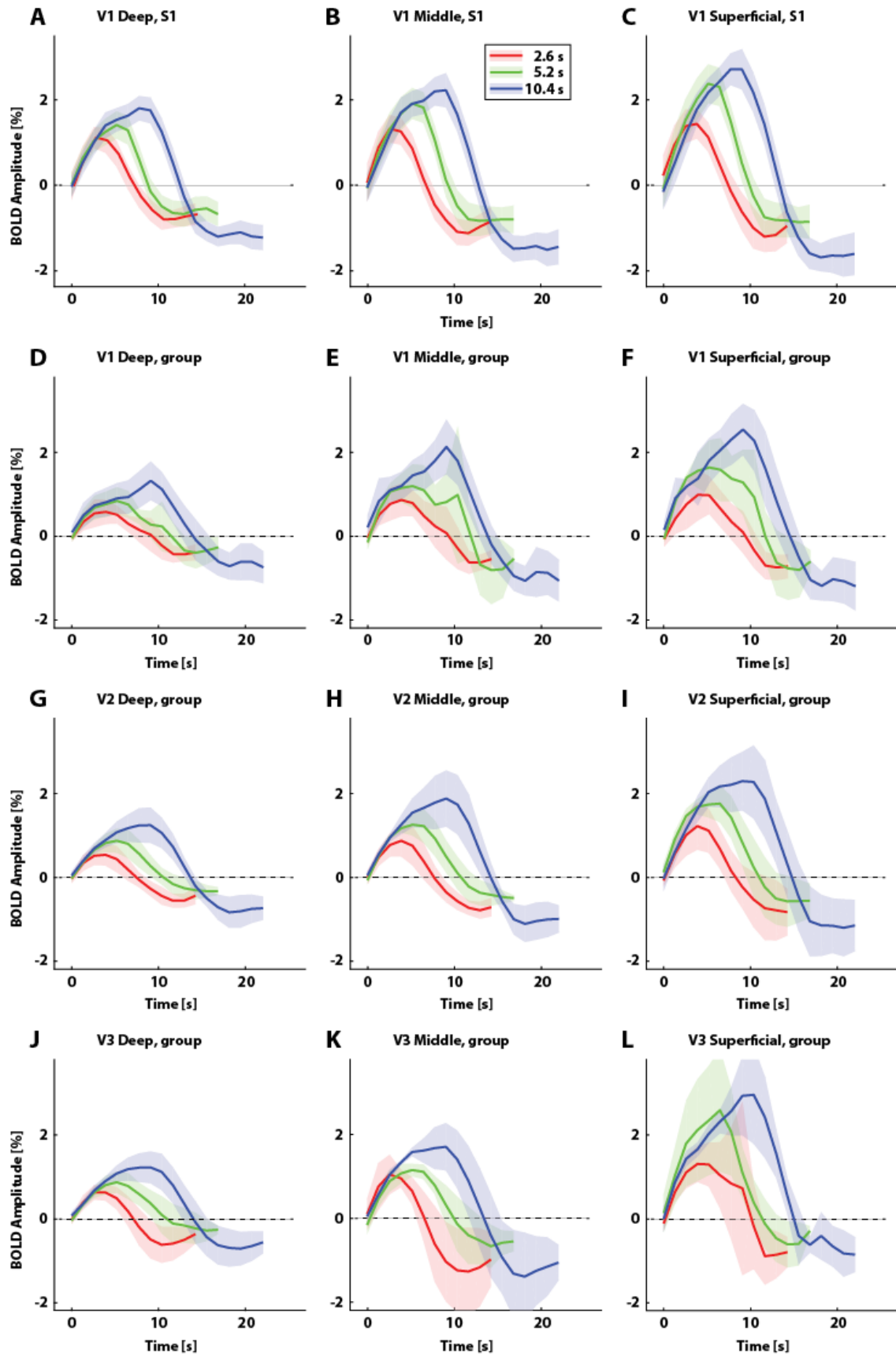


Figure 9: BOLD response profiles for three stimulus presentation durations at three cortical depth bins (deep, middle, and superficial). A-C) BOLD response profiles for one example subject, for visual field map V1. Different colors represent different stimulus presentation durations. Shaded regions represent

95% confidence intervals of the respective means across repeated stimulus presentations. Average normalized depth: 0.13 (deep), 0.58 (middle), and 0.91 (superficial). D-F) Group average BOLD response profiles for V1. Shaded regions represent 95% confidence intervals of the mean responses across participants. Average normalized depth: 0.13 (deep), 0.59 (middle), and 0.91 (superficial). G-I) As D-F, but for V2. Average normalized depth: 0.10 (deep), 0.54 (middle), and 0.90 (superficial). J-L) Idem, for V3. Average normalized depth: 0.10 (deep), 0.54 (middle), and 0.90 (superficial).

Shifted, summed response to shorter presentations show similar temporal progressions as longer presentations

To assess and visualize the temporal additivity assumption across cortical depth, we shifted the 2.6 s stimulus presentation curves for each cortical depth bin by 2.6 s and added this shifted response to the original 2.6 s response at the given bin. This resulted in the predicted response to a 5.2 s stimulus presentation duration. We then overlaid these predicted responses on the measured 5.2 s response (Figure 3A-C for three example cortical depth bins for V1; see Figures S1 and S2 for V2 and V3). Qualitatively, rise times and peak amplitudes for all ROIs and depth bins were generally similar between the predicted response and the 5.2 s measured response.

For the longest (10.4 s) stimulus presentation duration, we calculated predicted responses in the same manner as for the 5.2 s stimulus presentation duration above (Figure 3D-F). These predictions were computed from both the 2.6 s and 5.2 s responses separately. The predicted responses based on the 5.2 s presentation duration and the 10.4 s measured responses were highly similar over the entire time course of the response. The predicted responses from the 2.6 s presentation duration and the 10.4 s measured responses showed similar results (Figure 3A, D).

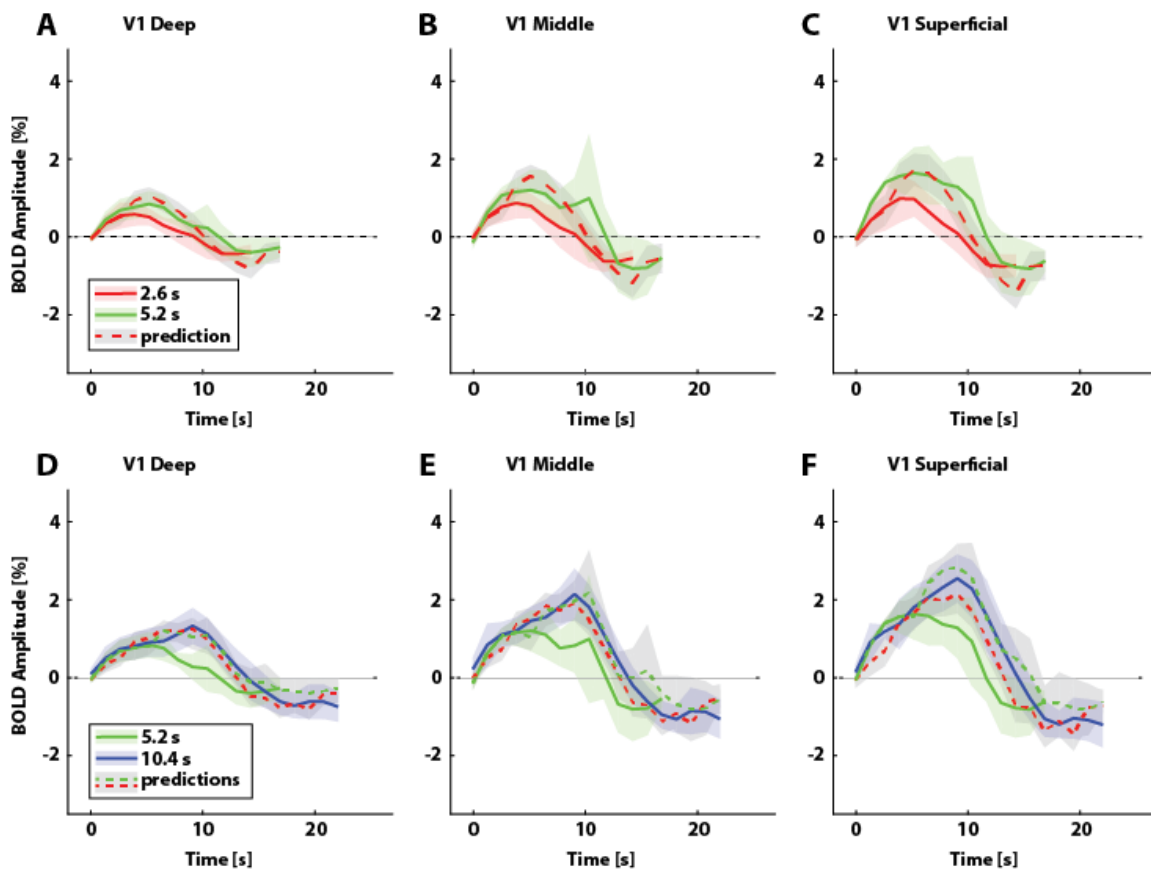


Figure 10: Predicted and measured BOLD response profiles at three cortical depth bins for visual field map V1. Average normalized depth: 0.13 (deep), 0.59 (middle), and 0.91 (superficial). A-C) Group

average responses to short (2.6 s, solid red lines) and medium (5.2 s, solid green lines) stimulus presentation durations, with predicted responses to medium presentation durations (dashed red lines) calculated by shifting and summing the measured responses to the short stimulus presentation duration for each depth bin. Shaded regions represent 95% confidence intervals of the mean response across participants. D-F) Group average responses to medium (5.2 s, solid green lines) and long (10.4 s, solid blue lines) presentation durations with predicted responses to long presentation durations, calculated by shifting and summing the measured responses to the short (dotted red lines) and medium (dotted green lines) presentation durations. Shaded regions represent 95% confidence intervals of the mean response across participants.

Temporal additivity is constant across cortical depth

To further assess the temporal additivity assumption across cortical depth, we calculated the fit quality of each prediction by calculating the correlation between that prediction and its associated measured response. Overall, all predictions for V1 were good fits to their respective measured responses (Figure 4A), with correlations ranging from $r = 0.90 - 0.98$, all $p < 0.001$. The correlation did not differ significantly between depth bins. Correlations for V2 ranged from $r = 0.91 - 0.98$, all $p < 0.001$, with no significant differences between cortical depth bins (Figure 4B). For V3, correlations were more variable, ranging from $r = 0.82 - 0.98$, all $p < 0.001$, with correlations slightly increasing towards the cortical surface (Figure 4C). Correlations were generally least variable in V1, and generally highest for the predictions made from the 5.2 s presentation to fit the measured 10.4 s presentation across visual field maps. Correlations for these predictions ranged from $r = 0.96 - 0.98$, all $p < 0.001$, and were very consistent between visual field maps and cortical depth bins.

We also visualized the fit quality across cortical depth for all participants for each visual field map (Figure 4D-F). Overall, between-participant average correlations in V1 were mostly consistent across cortical depth and between participants. The average across scaling conditions, between participants ranged from $r = 0.70 - 0.97$, all $p < 0.01$. Correlations for V2 were consistent across cortical depth (Figure 4E), with correlations ranging from $r = 0.89 - 0.96$, all $p < 0.001$. For V3, correlations were less consistent across cortical depth, and lower compared to other visual field maps (Figure 4F). However, they remained high at $r = 0.75 - 0.95$, all $p < 0.01$.

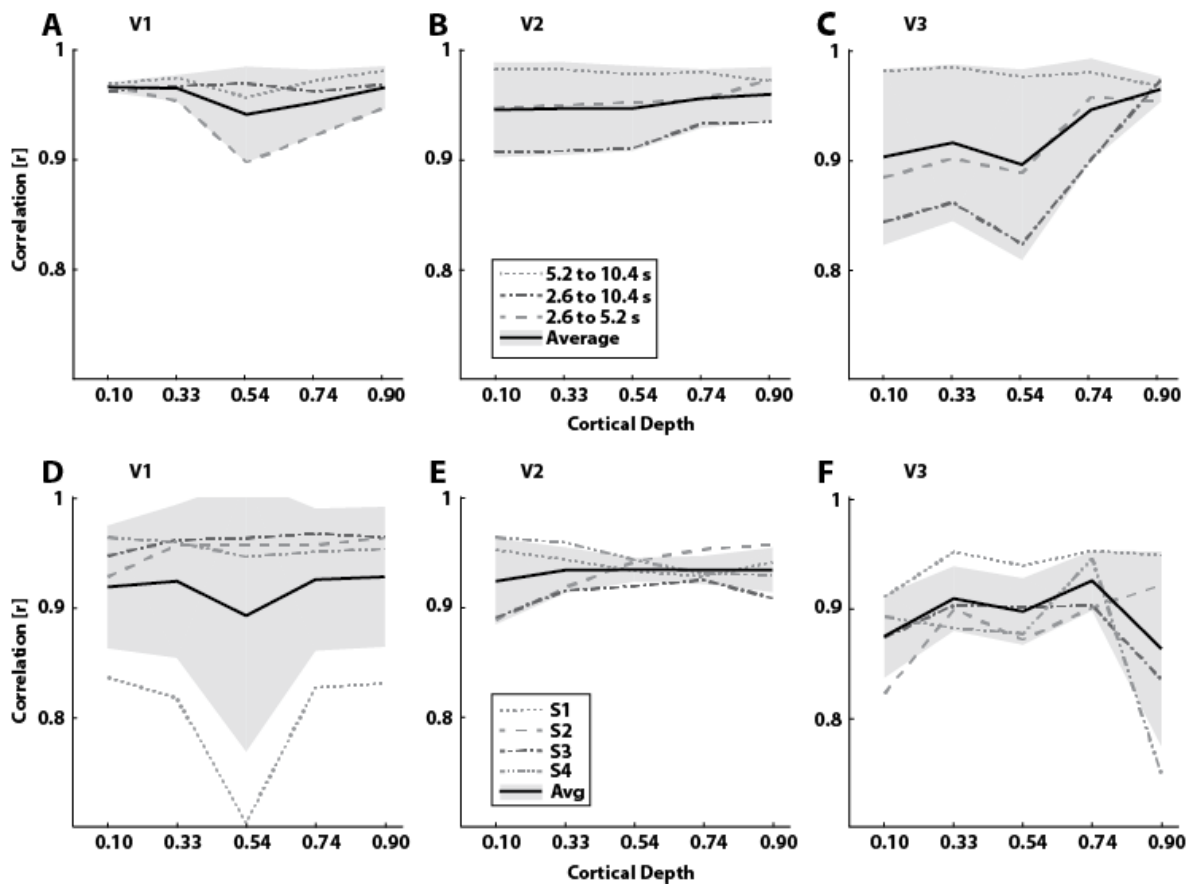


Figure 11: Goodness of fit across cortical depth for visual field maps V1, V2, and V3. A-C) Average correlation across scaling conditions (short presentation scaled to long and medium presentations; medium presentation scaled to long) for V1 (Figure 4A), V2 (Figure 4B), and V3 (Figure 4C). Shaded regions represent 95% confidence intervals of the mean across scaling conditions. D-F) Average correlation across participants for V1 (Figure 4D), V2 (Figure 4E), and V3 (Figure 4F). Dashed lines represent individual participants. Shaded regions represent 95% confidence intervals of the mean across participants.

Discussion

Here we assessed whether the temporal additivity assumption for a linear system holds in human visual cortex for BOLD amplitude across cortical depth. We evaluated GRE-BOLD fMRI responses at five cortical depth bins, elicited by moving sine wave gratings at 50% contrast and presented for 2.6, 5.2, and 10.4 s (short, medium, and long presentation). We find that BOLD response amplitudes vary both as a function of cortical depth, and presentation duration, with higher BOLD amplitudes towards the cortical surface, and with increasing presentation duration. In particular, we find that predictions to longer stimulus presentations based on the shorter presentations provide consistently good fits across cortical depth. Comparing between different predictions, correlations between predictions from the medium to the measured long presentation responses were generally highest across all visual field maps and cortical depths. In conclusion, we show that the temporal additivity assumption for BOLD response linearity holds across cortical depth for sub-millimeter BOLD amplitude measurements.

A growing body of research has focused on the feasibility of laminar GRE-BOLD fMRI in humans and other mammals. The majority of these studies have focused on the neurovascular coupling that underlies the fMRI signal in humans (De Martino et al., 2013; Herman et al., 2013; Huber, Goense, et al., 2014; Huber et al., 2015; Kemper et al., 2015; Koopmans et al., 2010, 2011, 2012; Olman et al., 2012; Polimeni et al., 2010; Ress et al., 2007; Siero et al., 2011; Xing et al., 2012; Zimmermann et al., 2011); non-human primates (Chen et al., 2012; Goense & Logothetis, 2006; Goense et al., 2012, 2007; Smirnakis et al., 2007; Zappe et al., 2008); and other mammals (Harel et al., 2006; Jin & Kim, 2008; Lu et al., 2004; Silva & Koretsky, 2002; Yang et al., 2002; Yu et al., 2012, 2014; Zhao et al., 2006). Even though relatively limited in number, the amount of studies employing laminar fMRI for systems and cognitive neuroscience questions has been growing steadily in recent years (Chen et al., 2011; Cheng et al., 2001; De Martino et al., 2015; Fracasso et al., 2016; Goodyear and Menon, 2001; Huber et al., 2015; Kok et al., 2016; Marquardt et al., 2018; Muckli et al., 2015; Smith and Muckli, 2010; Yacoub et al., 2008, 2007, for reviews see e.g. De Martino et al., 2018; Dumoulin et al., 2018; Lawrence et al., 2017; Petridou and Siero, 2017; Self et al., 2017; Self and Roelfsema, 2017; Stephan et al., 2019). However, most studies have interpreted BOLD amplitude measurements with caution, as these are susceptible to blood pooling effects across cortical depth since measures at different depths are inherently not independent. These studies have thus largely focused on non-amplitude sensitive measures. In this study, we provide evidence for the usability of BOLD fMRI amplitude measurements for systems and cognitive neuroscience questions and address the temporal additivity assumption for linear systems analysis that underlies many fMRI studies.

Particularly of note is that predictions from the short presentation duration fit to either the medium or the long presentation duration measured responses generally had the lowest correlations, particularly in V2 and V3 (Figure 4B-C). Lower fits indicate deviations from linearity. A potential explanation for this pattern, is that the short presentation duration at 2.6 s is quite comparable to an event-related design, in which deviations from linearity are regularly found (see e.g. Birn, Saad, & Bandettini, 2001; Kershaw, Kashikura, Zhang, Abe, & Kanno, 2001; Pfeuffer, McCullough, Van De Moortele, Ugurbil, & Hu, 2003; Robson, Dorosz, & Gore, 1998; Soltysik, Peck, White, Crosson, & Briggs, 2004; Vazquez & Noll, 1998; Zhang, Zhu, & Chen, 2008). Moreover, e.g. Birn, Saad and Bandettini show that deviations from linearity are greater in extrastriate cortex than in striate cortex around stimulus presentations lasting 2 s (Figure 4 in Birn et al., 2001). This might contribute to the decreased deviations from linearity for the predictions based on the 2.6 s presentations in V1 compared to V2 and V3, as found here. Additionally, studies show that nonlinear effects might increase when moving up in the visual field map hierarchy, with responses in V1 being the most linear, and higher-order visual field maps showing increasing deviations from response linearity. This has been shown for both the spatial (Kay, Winawer, Mezer, & Wandell, 2013; Wandell, Winawer, & Kay, 2015) and temporal domain (Zhou, Benson, Kay, & Winawer, 2018).

The presence of deviations from linearity (correlations of lower than 1.0) does not invalidate the current assessment of temporal additivity across cortical depth. Deviations from linearity at each cortical depth between presentation durations were to be expected. Thus, we set out to assess whether the deviations from linearity were consistent across cortical depth within visual field map, which should be reflected in the goodness of fit plots as straight horizontal lines (Figure 4). Following this logic, temporal additivity is consistent across depth in V1 and V2, with good to very good fits. These patterns generally also hold across participants (Figure 4D-F). The pattern of model fits across depth in V3 is more heterogeneous, but correlations are still generally consistent across cortical depth.

GRE 3D-EPI acquisitions are sensitive to both the microvasculature (i.e. arterioles, capillaries, and venules) and macrovasculature (e.g. draining veins) in and around the cortex. The measured signal is thus affected by blood pooling towards the cortical surface. Thus, the hemodynamic consequences of neuronal signals elicited at deeper cortical depths propagate towards the cortical surface, affecting the measured signal at more superficial cortical depths. This then leads to less laminar specificity and the regularly observed increase of BOLD signal amplitude towards the cortical surface. The increase in BOLD signal amplitude towards the cortical surface is also clearly present in the current study, with peak amplitudes for each individual condition increasing in this direction. Undesired blood pooling effects across cortical depth can be dealt with in several ways. Firstly, these effects can be corrected for at the analysis level, for instance by means of spatial correction approaches (see e.g. Markuerkiaga et al., 2016; Marquardt et al., 2018), or by implementing more elaborate models of the spatiotemporal properties of the hemodynamic signal and associated dynamics of capillary, venous, and arterial effects (Aquino et al., 2014, 2012; Boas et al., 2008; Heinzle et al., 2016; Puckett et al., 2016; Uludağ & Blinder, 2018). Secondly, blood pooling effects can be reduced at the acquisition level by choosing an acquisition protocol that is less sensitive to macrovascular effects, such as spin echo-based sequences, 3D-GRASE (Feinberg & Günther, 2009), or VASO (Huber et al., 2015, 2017; Jin & Kim, 2008).

For the current results to be generalizable, even within the visual domain, linearity for stimuli varying in high- and other low-level domain such as spatial frequency content should also be evaluated in a similar way as presented here. Moreover, a wider range of stimulus presentation durations could be employed to better cover the extremes of this stimulus space. However, the presentation durations used here are similar to the range used in a wide range of block-design fMRI studies. Our data do not allow for the investigation of different contributions to the generation of the BOLD signal, so neuronal to vascular and vascular to BOLD contributions cannot be disentangled with the current experimental design. Additionally, because of pooling of large numbers of voxels in this region of interest-based approach, we cannot exclude that local pockets of nonlinearity might be present within a visual field map. However, our results do provide support for the temporal additivity of BOLD amplitude measures across cortical depth as a function of stimulus duration, for region of interest-based approaches. Together with our previous assessment of scaling across cortical depth (van Dijk et al., submitted), we now provide a comprehensive assessment of response linearity across cortical depth for amplitude-based GRE-BOLD laminar fMRI.

Conclusion

We provide evidence that the temporal additivity assumption for linear systems theory is met for BOLD amplitude measures across cortical depth in V1, V2, and V3. This is reflected by the horizontal profile of correlation values across cortical depth of the model fits of the predictions (shifted and summed responses) on the measured responses. All in all, this work in conjunction with our earlier experiments provides a more complete assessment of linearity assumptions across cortical depth, and thus the validity of GLM-based analyses of BOLD amplitude measures for laminar fMRI of the early visual cortex.

Supplementary figures

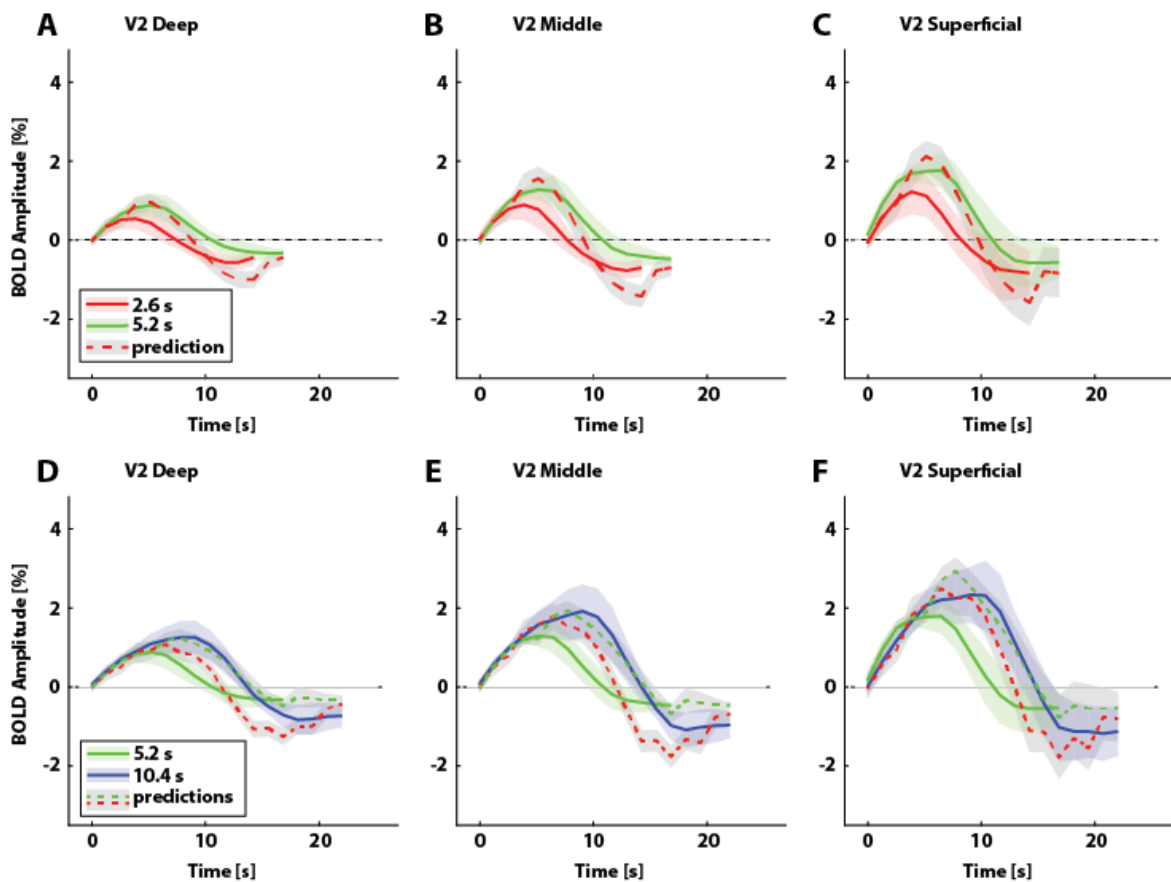


Figure S 3: Predicted and measured BOLD response profiles at three cortical depth bins for visual field map V2. Average normalized depth: 0.10 (deep), 0.54 (middle), and 0.90 (superficial). A-C) Group average responses to short (2.6 s, solid red lines) and medium (5.2 s, solid green lines) stimulus presentation durations, with predicted responses to medium presentation durations (dashed red lines) calculated by shifting and summing the measured responses to the short stimulus presentation duration for each depth bin. Shaded regions represent 95% confidence intervals of the mean response across participants. D-F) Group average responses to medium (5.2 s, solid green lines) and long (10.4 s, solid blue lines) presentation durations with predicted responses to long presentation durations, calculated by shifting and summing the measured responses to the short (dotted red lines) and medium (dotted green lines) presentation durations. Shaded regions represent 95% confidence intervals of the mean response across participants.

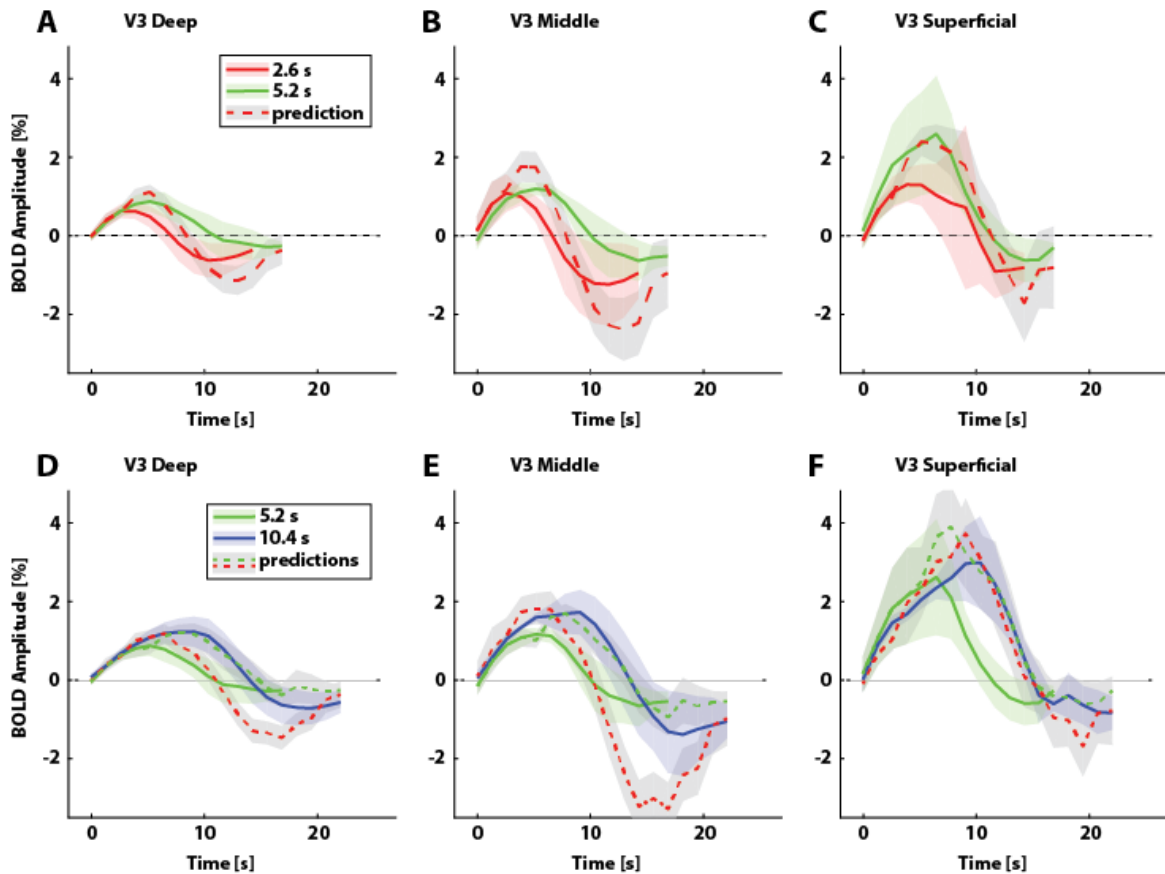


Figure S 4: Predicted and measured BOLD response profiles at three cortical depth bins for visual field map V3. Average normalized depth: 0.10 (deep), 0.54 (middle), and 0.90 (superficial). A-C) Group average responses to short (2.6 s, solid red lines) and medium (5.2 s, solid green lines) stimulus presentation durations, with predicted responses to medium presentation durations (dashed red lines) calculated by shifting and summing the measured responses to the short stimulus presentation duration for each depth bin. Shaded regions represent 95% confidence intervals of the mean response across participants. D-F) Group average responses to medium (5.2 s, solid green lines) and long (10.4 s, solid blue lines) presentation durations with predicted responses to long presentation durations, calculated by shifting and summing the measured responses to the short (dotted red lines) and medium (dotted green lines) presentation durations. Shaded regions represent 95% confidence intervals of the mean response across participants.

Chapter 4

Numerosity-selective population receptive field properties across cortical depth

van Dijk, J.A., Fracasso, A., Petridou, N., & Dumoulin, S.O., Numerosity-selective population receptive field properties across cortical depth (in preparation)

Acknowledgement of author contributions

JAvD and SOD designed the experiment; JAvD collected the data; JAvD and AF analyzed the data; all authors contributed to and reviewed the manuscript text; JAvD prepared all figures; SOD, NP, and AF provided general supervision and guidance throughout.

Abstract

Numerosity perception refers to the perception of the set size of a group of items. It is a trait shared across many species and is linked to many cognitive functions. In humans, topographically organized cortical regions responsive to numerosity have been identified using functional magnetic resonance imaging (fMRI). Neuronal populations in these regions show a response preference for specific numerosities, and this preference gradually changes along the cortical surface. With the development of sub-millimeter (laminar) fMRI acquisitions and associated analysis techniques, it has become possible to start probing at feedforward and feedback processing across cortical depth, adding an additional dimension to fMRI experiments. While knowledge about this information processing is increasing rapidly for early visual cortex, little is known about higher-order visual information processing across cortical depth. We use laminar fMRI to investigate this for numerosity perception. Following an early visual processing account, we expected a U-shaped or inverted U-shaped profile for numerosity tuning width across cortical depth. We find that tuning width increases with preferred numerosity for individual depth compartments, while the tuning width profile across cortical depth generally does not significantly differ from constant. The flat tuning profile is inconsistent with the early visual cortex-based models, but may be consistent with similar tuning width profiles between topographically organized cortical numerosity-selective regions as found in previous fMRI studies.

Introduction

Numerosity is the set size of a group of items. A wide range of species has been shown to be capable of making numerosity judgements, including human infants (Dehaene, 1997) and children (Cantlon et al., 2009), non-human primates (Brannon & Terrace, 1998; Hauser, Carey, & Hauser, 2000; Hauser et al., 2003), corvids (Ditz & Nieder, 2016a), cats (Pisa & Agrillo, 2009), and zebra fish (Potrich et al., 2015). Numerosity perception is implicated in many cognitive functions (Burr & Ross, 2008) such as multiple object tracking (Piazza, 2011), mathematics (Dehaene, 1997; Halberda et al., 2008; Harvey, 2016), decision making (Nieder & Miller, 2003), and dividing attention (Knops et al., 2014). Neurons that respond selectively to stimuli of a specific numerosity have been found using electrophysiological recordings in corvids (Ditz & Nieder, 2015, 2016b), monkeys (Nieder, Freedman, & Miller, 2002; Nieder & Miller, 2003, 2004; Sawamura, Shima, & Tanji, 2002; Tokita & Ishiguchi, 2010), and humans (Kutter, Bostroem, Elger, Mormann, & Nieder, 2018). Using functional magnetic resonance imaging (fMRI), further studies in humans have identified a network of cortical areas involved in numerosity processing (Cantlon et al., 2009; Dehaene, Spelke, Pinel, Stanescu, & Tsivkin, 1999; Eger et al., 2009; Knops et al., 2014; Piazza, Izard, Pinel, Le Bihan, & Dehaene, 2004; Pinel et al., 1999). Moreover, recent fMRI studies have revealed the existence of a topographic organization for several higher order cortical regions, with numerosity response preference and preferred numerosity range (tuning width) of neuronal populations gradually changing along the cortical surface (Harvey & Dumoulin, 2017; Harvey, Klein, et al., 2013).

Feedforward information in early visual cortex mostly arrives in layer IV (granular layer; Hubel & Wiesel, 1962, 1972, 1974), whereas feedback connections mainly terminate in layers I (a supragranular layer) and V/VI (infragranular layers) while avoiding layer IV (Anderson & Martin, 2009; Felleman & Van Essen, 1991; Graham, Lin, & Kaas, 1979; Markov & Kennedy, 2013; Rockland & Pandya, 1979; Wong-Riley, 1979). Lateral connections are present in all layers (Felleman & Van Essen, 1991). Using sub-millimeter fMRI, it is possible to study these information processing flows (for reviews see De Martino et al., 2018; Dumoulin et al., 2018; Lawrence et al., 2017; Petridou and Siero, 2017; Self et al., 2017; Self and Roelfsema, 2017; Stephan et al., 2019). Here we use sub-millimeter fMRI to investigate information processing across cortical depth in a parietal numerosity-responsive topographic map.

Tuning widths (population receptive field (pRF) sizes) in the visual system increase in size as information is processed further and further. This is reflected in increasing pRF sizes in cortical areas with increasing rank in the visual hierarchy (see e.g. Dumoulin & Wandell, 2008; Harvey & Dumoulin, 2011). Following this logic, pRF estimates across cortical depth should show a U-shaped profile, i.e. smallest in the central layer and increase both towards the infragranular layers and the supragranular layers). Indeed, this is confirmed by data showing that layer IV is populated with simple cells, while the supra- and infragranular layers contain complex cells with larger receptive fields (Hubel, 1988). Furthermore, presence of this U-shaped profile has been confirmed using monkey electrophysiology (Self et al., 2019) and human sub-millimeter fMRI (Fracasso, Petridou, et al., 2016). If processing in the association cortex is similar to early visual processing, we would expect such a U-shape across cortical depth to also be present for numerosity tuning in higher-order association cortex. Alternatively, an inverted U-shaped tuning width profile across cortical depth might be observed as processing may sharpen tuning widths to ultimately arrive at an accurate numerosity percept.

We use ultra-high field sub-millimeter fMRI to investigate tuning width and preferred numerosity profiles, and thus processing across cortical depth, in a topographical numerosity map in the parietal cortex. We show that tuning width consistently increases with preferred numerosity for individual cortical depth bins, and that tuning width generally does not vary significantly across cortical depth. We speculate that this may reflect a fundamental difference in processing between visual and numerosity-responsive cortex.

Methods

Subjects

Eight subjects (1 female, mean age: 31.4 years, age range 22-45 years old) participated in this study. All subjects were familiar with the MRI environment and had participated in previous experiments. They had normal or corrected-to-normal visual acuity. One subject was excluded because of poor signal quality. All subjects signed informed consent. All experimental procedures were approved by the medical ethics committee of the University Medical Center Utrecht and adhered to the guidelines of the Declaration of Helsinki.

Stimuli

Stimuli were presented on a 32-inch LCD screen, specifically designed for use in an MRI environment (Cambridge Research Systems, 2012). The screen resolution was 1920 x 1080 pixels, with a screen size of 69.8 x 39.3 cm, a refresh rate of 120 Hz, and a built-in linear luminance look-up table. The display was positioned at the far end of the bore and was viewed via a mirror positioned in the head coil of the MRI scanner. The total viewing distance was 220 cm. The total visible vertical extent of the screen subtended 10.2 degrees visual angle (deg).

All stimuli were generated in MATLAB (Mathworks; 2018a) using the Psychophysics toolbox (Brainard, 1997; Pelli, 1997). A large cross consisting of two thin (1 pixel) red diagonal lines starting at the corners of a 10.2 x 10.2 degree invisible square and intersecting in the center of the screen was presented at all times, with a mean luminance gray background that covered the entire screen. Stimuli consisted of groups of circles, randomly distributed to be presented entirely within an invisible circle with a 0.75-degree radius around the center of the screen. Each group of circles contained 1 to 7 or 20 circles, with 20 functioning as a baseline. Numerosity 20 was chosen to this end as it is expected to be well outside the response range of neuronal populations responding to numerosities 1 to 7, while neuronal populations responding to contrast energy would be expected to respond most strongly to this energy-rich condition (Harvey, Vansteensel, et al., 2013). The total surface area (702 pixels) of each group of circles was constant between different numerosities. This resulted in a decreased size per circle with increasing numerosity (see Figure 1A). This stimulus configuration was identical to the 'constant area' stimulus condition used in previous fMRI numerosity studies (Harvey & Dumoulin, 2017; Harvey, Klein, et al., 2013). On regular trials, the circles were black. However, groups of white circles with the same numerosity were randomly presented instead of black ones on approximately 9% of the trials. Subjects were asked to respond to these presentations by means of a button press. No numerosity-related judgments were required. Average task performance was 97.4 % correct (range 69.8 - 100 % for individual runs).

Stimuli were presented for 350 ms, followed by 250 ms of mean luminance gray. Numerosities 1 to 7 were displayed sequentially, first in ascending order and then in descending order. Each numerosity was presented six times (3600 ms including mean luminance gray presentations) before the next numerosity was presented. Numerosity 20 was presented after each ascending or descending sweep, (see Figure 1B). These presentations of numerosity 20 lasted 14400 ms (24 presentations). The combination of the ascending and descending sweep interleaved with numerosity 20 was repeated 4

times for each run. Each run started with 20 presentations of numerosity 20 (12000 ms). The total presentation time for one run was 5 m 28.8 s. The stimulus sequence and displays were near-identical to those previously used by Harvey and colleagues (Harvey & Dumoulin, 2017; Harvey, Klein, et al., 2013). Subjects completed 7 (one subject), 8 (one subject) or 9 (five subjects) runs.

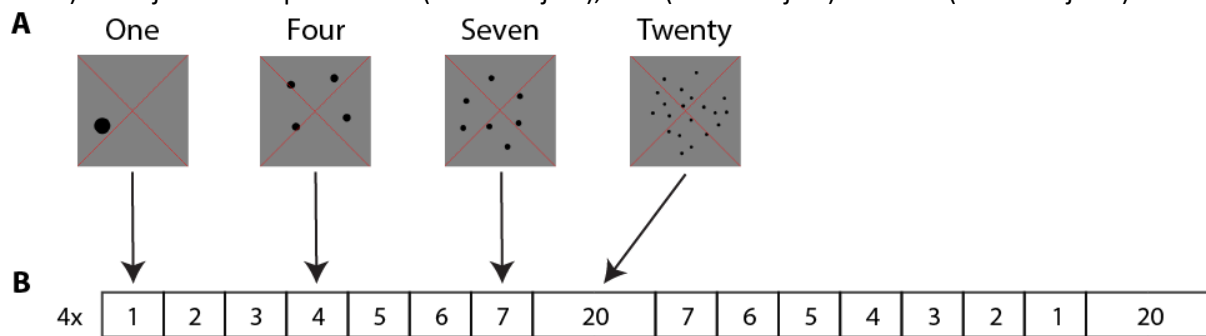


Figure 12: Stimulus design. A) Example stimulus displays with numerosity 1, 4, 7, and 20. B) Stimulus sequence. Numerosities 1-7 were presented sequentially, first in ascending, then in descending order. After each sweep, a longer block of numerosity 20 (baseline) was presented. The depicted sequence was repeated four times per run.

Region of interest definition

One topographically organized numerosity map in the parietal cortex of the right hemisphere (NPC1: (Harvey & Dumoulin, 2017; Harvey, Klein, et al., 2013) was selected for this study (Figure 2A). This region of interest was defined based on previous numerosity experiments in all but one subject (Harvey & Dumoulin, 2017; Cai et al., in preparation). For this one subject, the region of interest definition was based on the data from the current experiment. Right NPC1 was selected for its consistency between subjects (Harvey & Dumoulin, 2017) and relative ease of targeting with the high-density surface receive arrays (see next paragraph).

MRI and fMRI acquisition

High resolution anatomical and functional data were acquired using a Philips Achieva 7 T scanner. with a maximum gradient strength of 40mT/m and a slew rate of 200 T/m/s (Philips, Best, The Netherlands). A dual-channel volume transmit head coil was used for all scans (Nova Medical, MA, USA). A 32-channel receive coil (Nova Medical, MA, USA) was used for all anatomical scans, and two custom-built 16-channel high-density surface receive arrays were used for all functional scans (Petridou et al., 2013; MRCoils BV). Positioning of these receive arrays was preformed outside the scanner. First, subjects put on a cloth cap to prevent sliding of the surface arrays on their hair and facilitate accurate targeting of the region of interest. Next, the receive arrays were placed on the head, with their centers at approximately the height of electrode location CPz (following the extended 10-20 system for electrode positioning), aligned with midline of the head of the subject. The receive arrays touched each other but did not overlap. The exact positioning was varied per subject, as the process was ultimately guided by the personalized location of NPC1 based on previous numerosity fMRI studies for all but one subject. After positioning, the receive arrays were fixed in place with Powerflex bandage -a type of bandage that sticks only to itself- around the forehead and chin of the subject and a set of noise-dampening non-ferromagnetic headphones. The subject was then carefully transferred to the scanner environment, where the receive arrays were further held in place using sandbags behind the head of the subject. The subject was positioned such that the middle of the receive arrays (in the volume transmit coil) were approximately in the isocenter.

T1-weighted anatomical data for four subjects were acquired using an MP2RAGE sequence (Marques et al., 2010). Sequence parameters were: T11 = 800 ms, T12 = 2700 ms, $TR_{MP2RAGE}$ = 5500 ms, TR/TE = 6.2/2.3 ms, flip angle α_1 = 7, and α_2 = 5, bandwidth = 403.7 Hz/pixel, acceleration factor using SENSE

encoding = 3.5×1.3 (RL and AP respectively), resolution = 0.65 mm isotropic, whole-brain coverage, total scan time 9 min 57 s. T1-weighted anatomical data for the other three subjects was acquired using an MPRAGE sequence combined with a proton-density (PD)-weighted sequence. The PD-weighted acquisition was used to correct for image intensity inhomogeneities. Sequence parameters for the MPRAGE acquisition were: TR/TE = 7/2.8 ms, flip angle $\alpha = 8$ degrees, resolution = $0.49 \times 0.49 \times 0.8$ mm, whole-brain coverage, total scan time 4 min 56 s. Sequence parameters for the PD acquisition were: TR/TE = 5.8/2.8 ms, flip angle $\alpha = 1$ degree, resolution = $0.49 \times 0.49 \times 0.8$ mm, whole-brain coverage, total scan time 1 min 16 s. The field of view, orientation, and location of the PD scan was identical to the MPRAGE. T1-weighted anatomical data for one subject were acquired on a 3T MRI scanner. Sequence parameters were TR/TE = 10/4.6 ms, flip angle $\alpha = 8$ degrees, resolution = $0.80 \times 0.75 \times 0.75$ mm, whole-brain coverage.

Functional data were acquired using a T2*-weighted 3-dimensional multi-shot EPI (3D-EPI, two shots per slice, 24 slices, 48 shots overall). The sequence parameters were: TR/TE = 60/28.9 ms, flip angle: 20° , acceleration factor using SENSE encoding: 3.5 (right-left) \times 1.3 (anterior-posterior), echo planar factor: 37, bandwidth (phase-encode): 790.1 Hz/pixel, voxel size = 0.93 mm isotropic, FOV = 119 (right-left) \times 119 (feet-head) \times 22.32 (anterior-posterior) mm, 24 coronal slices, and 10% oversampling in the slice direction. The volume repetition time was 1200 ms. Each functional run was 274 time frames in duration. The acquisition volume was rotated approximately 40° in the sagittal plane to assure maximum coverage of the region of interest (Figure 2B). The exact angulation differed between subjects, depending on their orientation in the scanner and location of the region of interest.

For each functional run, we acquired an additional five volumes with reversed right-left phase-encoding. Reversing the phase-encoding direction ensured that these so-called ‘topup’ runs had the opposite geometrical distortions to the original volumes (Andersson et al., 2003). These topup runs were used in conjunction with the original data to estimate a nonlinear warp field to create a susceptibility distortion-free volume, which is the midpoint between the functional and topup data (Andersson et al., 2003). This undistorted volume then makes it possible to align the functional data to the subject anatomy with improved accuracy, needed for cortical depth-based analysis.

Pre-processing

Data processing was performed using AFNI (Cox, 1996) and MATLAB (Mathworks; 2015b). First, a warp field to correct for susceptibility distortions was calculated using a nonlinear transformation, with the first five volumes of each of the functional and topup runs as input. Subsequently, motion parameters between runs were estimated by aligning the first volume of each run to the first volume of the first run using Fourier interpolation. Next, the first 10 time points of each run were removed to ensure that the signal had reached a steady state after the start of stimulus presentation. All runs were then individually despiked, scaled, and detrended. Despiking was performed using the AFNI function 3dDespike. The scaling step entailed converting the time-series of each run to percentage signal change. For the detrending, the AFNI function 3dDetrend with up to a fourth-degree polynomial was used. Lastly, all runs were then averaged together and the between-run average temporal mean of each voxel was added, resulting in the mean time-series used as input for the numerosity modelling (see below).

Next, the motion estimates and previously computed warp field to correct for susceptibility distortions were applied to each run. Then, the mean EPI image was computed by taking mean across all these runs and time-points. This EPI mean image was then registered to the anatomy using a multi-step procedure. First, the anatomy was restricted to roughly the parietal lobe using the AFNI function @clip_volume. Next the EPI mean image was de-obliques using the AFNI function 3dWarp. Then, the

de-obliques EPI mean image and anatomy were brought into the same space by aligning the center of mass of the anatomy to the de-obliques EPI mean image. Then, the 'Nudge dataset' AFNI plugin was used to manually shift and rotate the de-obliques EPI mean image to provide a good starting point for two automated registration steps. These registration steps both consisted of an affine transformation to further optimize the registration, using local Pearson correlation as cost function (Saad et al., 2010). The first transformation allowed for a maximum rotation and/or shift of 3 mm in any direction, while the second transformation allowed for a maximum rotation and/or shift of 1 mm. These affine transformations were then applied to the manually moved, mean de-obliques EPI image. The transformation matrices of the manual step and the two affine transformations were combined into a single affine matrix. To assure that these matrices were combined correctly, the combined affine matrix was then applied to the original EPI mean image. These results were then inspected for registration quality.

All anatomical data were resampled to a 0.6 mm isotropic resolution using linear resampling. Gray/white matter classifications of the MP2RAGE anatomical data (four subjects) were carried out using MIPAV (<http://mipav.cit.nih.gov/>) with the CBS-tools plugin (Bazin et al., 2007; www.nitrc.org/projects/cbs-tools/). For the MPRAGE anatomical data (three subjects), gray/white matter classification was performed using Freesurfer (<http://surfer.nmr.mgh.harvard.edu/>). All classifications were manually optimized. Volume-preserving distance maps between the gray-white matter (GM/WM) border and the gray matter-cerebrospinal fluid (GM/CSF) border for all subjects were computed using MIPAV with the CBS-tools plugin (Waehnert et al., 2014). The distortion-corrected mean time-series were then projected on these volumes for subsequent laminar analysis (Figure 2A, B).

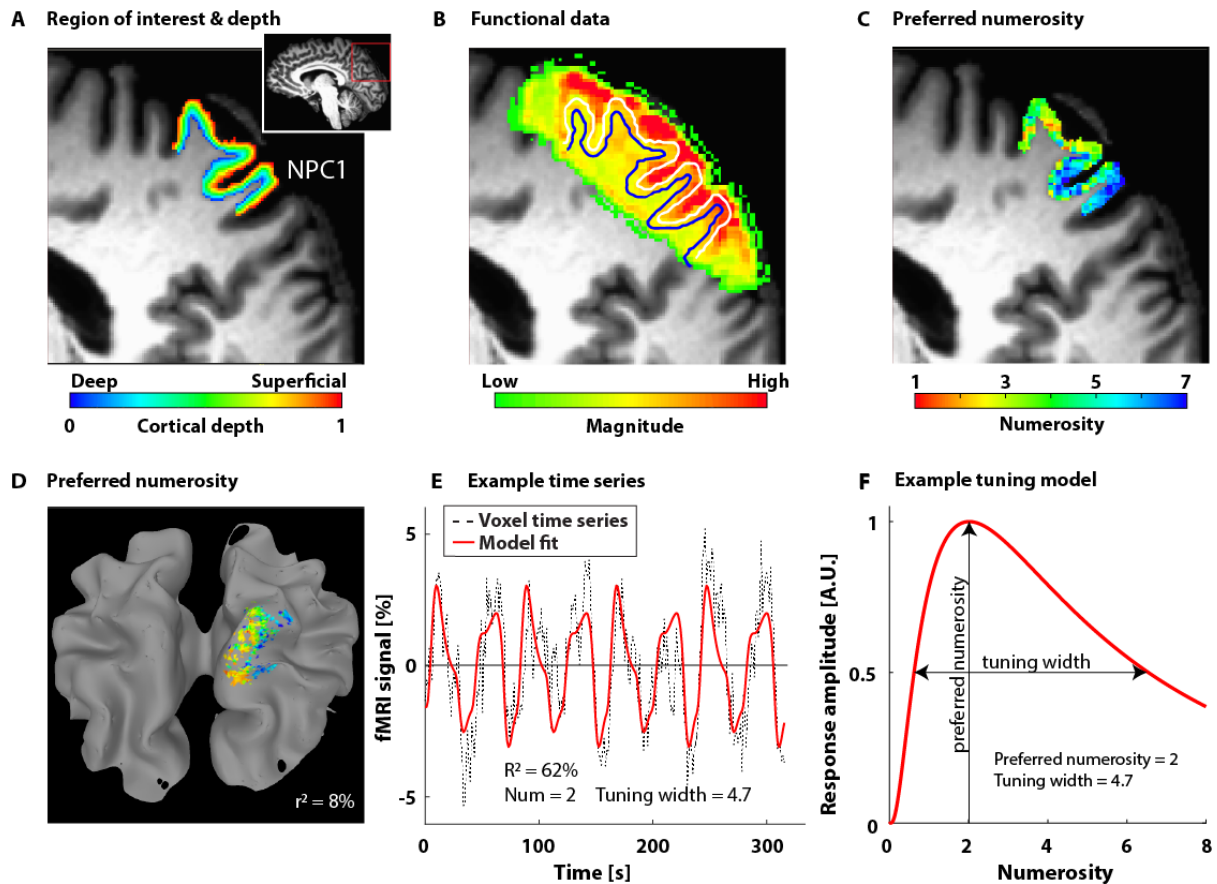


Figure 13: Processing steps and model fits. A) Region of interest (NPC1) definition and volume-preserving cortical depth map on a partial sagittal anatomical slice. Inset: whole brain anatomical slice with the location of the partial slice (red box). B) Mean susceptibility-corrected functional data registered to the anatomy, with gray matter-CSF (white) and gray-white matter (blue) borders. C) Preferred numerosity results at all depths for the region of interest. No threshold was applied. D) Preferred numerosity at the middle depth bin on a partial mesh corresponding to the coverage in A-C), coronal view. Threshold: $R^2 = 8\%$. E) Time-series of an example voxel (dotted line), overlaid with best fitting predicted fMRI response (solid red line). Goodness of fit (R^2) = 62%, preferred numerosity = 2, tuning width = 4.7. F) Example tuning model with the same preferred numerosity and tuning width as in E).

Analysis

Numerosity modelling

Numerosity tuning for each voxel was estimated from the mean time-series data and the stimulus time course, using methods very similar to pRF mapping (Dumoulin & Wandell, 2008). These methods have previously been described in Harvey and colleagues (2013). This analysis was performed using the mrVista software package (<http://white.stanford.edu/software/>) and custom numerosity-modelling code from Harvey and colleagues (2013, 2017).

In short, we estimated the aggregate numerosity tuning of neurons in each voxel. This numerosity tuning consisted of a preferred numerosity, and a tuning width for each (numerosity-selective) voxel. A forward model was used to predict the neuronal response based on the overlap of the presented numerosity at each time point in time and the numerosity tuning. This model estimated preferred numerosity and tuning width in logarithmic space as the mean and standard deviation of a Gaussian respectively. A Gaussian numerosity tuning model in logarithmic space has previously been shown to result in better model fits than a Gaussian model in linear space (Harvey, Klein, et al., 2013), and was

further motivated by behavioral (Nieder & Miller, 2003), neurophysiological (Nieder & Miller, 2003, 2004), computational (Dehaene & Changeux, 1993), and other neuroimaging (Piazza et al., 2004) studies. Next, the predicted neuronal response was convolved with a canonical two-gamma hemodynamic response function (HRF; Friston et al., 1998) to make a predicted fMRI time-series. This process was repeated to create a set of predicted fMRI time-series, for all combinations of a large range of preferred numerosity (67 equal steps between 0 and 2) and tuning width (400 equal steps between 0.03 and 3) parameters. A single neuron is highly unlikely to show a response preference for a non-integer numerosity, as numerosity perception is inherently integer. However, as single voxels contain many neurons that might contain different sub-populations of numerosity-selective neurons, the averaged numerosity preference of a voxel may be a non-integer value. Therefore, predictions were also made for non-integer preferred numerosity. The predicted time-series were then compared to the fMRI time-series of each voxel, and the best fitting parameters for each voxel were chosen by minimizing the sum of squared errors between the predicted and measured time-series (Figure 2C-E). The best fitting preferred numerosity and tuning width were then converted to linear space, resulting in an asymmetric Gaussian with a peak at the preferred numerosity and a tuning width of its full width at half maximum (FWHM, Figure 2F; Harvey et al., 2013).

Cortical depth analysis

Volumes containing the numerosity modelling results were de-obliques and subsequently registered to the anatomy by applying the combined registration matrix (see the 'Pre-processing' section above) and the susceptibility-correction warp field using the AFNI function 3dNwarpApply with wsinc5 interpolation. These registered, distortion-corrected volumes were then resampled to the anatomy (using 3dResample with nearest-neighbor interpolation), resulting in the registered numerosity modelling results volumes. In total, the numerosity modelling results were spatially resampled twice, resulting in the registered, distortion-corrected numerosity modelling results in anatomy space (Figure 2C).

To assess preferred numerosity and tuning width at different cortical depth bins, we divided the volume-preserving depth map into 7 equal depth quantiles spanning from the GM/WM to the GM/CSF border. Next, we selected voxels within each cortical depth bin for each region of interest. Only voxels with a goodness of fit (explained variance; R^2) that exceeded the 80th R^2 percentile within that depth bin were included in further analysis (range: $R^2 = 3 - 28\%$). If not stated explicitly, the reported results are from this thresholding procedure. When stated explicitly, this procedure is called 'variable threshold'. The analysis was repeated using an absolute explained variance threshold of 10%. This threshold is denoted as the 'fixed threshold' procedure in the results (where applicable). The 80th percentile thresholding approach was used to avoid inclusion of an increasing number of voxels towards superficial depth bins, as explained variance generally increases towards the cortical surface (Fracasso, Petridou, et al., 2016). The fixed thresholding approach was included as it is the traditional thresholding method for numerosity and pRF modelling methods (Dumoulin & Wandell, 2008; Harvey, Klein, et al., 2013).

After thresholding, we estimated a bootstrapped linear fit on the preferred numerosity and tuning width of the selected voxels. This was repeated for each depth bin. Next, we sampled these fits at numerosity 3 and 5 for each subject and depth, and subsequently Z-scored. These results were then averaged across subjects and a second-degree polynomial was fit on the data. In parallel, the average tuning width was calculated per subject for each depth bin and subsequently Z-scored. These data were then combined, and a second-degree polynomial fit was performed on the group data.

Results

Tuning width increases with preferred numerosity

The R^2 80th percentile at each depth bin was used as a threshold for the model parameters (preferred numerosity and tuning width). This resulted in approximately equal numbers of voxels in each depth bin. The average number of voxels included across all subjects and depth bins was: $M = 395.5$ voxels (85.4 mm^3), standard deviation (SD) = 116.1 voxels. On average, estimated tuning width increased with preferred numerosity across subjects: $M_{\text{slope}} = 2.05$, $SD_{\text{slope}} = 1.65$, $Range_{\text{slope}} = -0.75 - 5.95$ (Figure 3A-C, E-G for two example subjects). Estimated tuning width increased with preferred numerosity for 43 out of 49 depth bins.

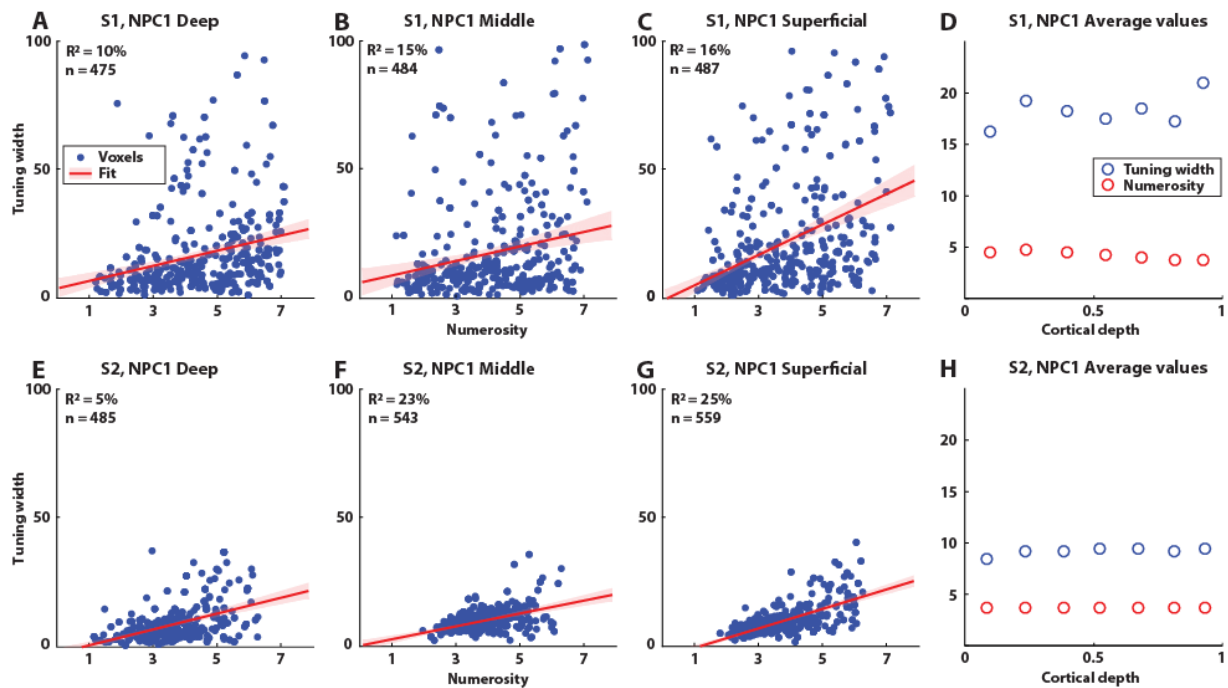


Figure 14: Preferred numerosity and tuning width across cortical depth for two example subjects. The threshold for each depth bin is the 80th R^2 percentile. A-C, E-G) Preferred numerosity versus tuning width at three cortical depth bins. Average normalized depth: 0.09 (deep), 0.54 (middle), and 0.93 (superficial). Blue circles represent individual voxels. Red lines represent the best linear fit. Shaded regions represent 95% confidence intervals of the linear fit. Tuning width consistently increased with increasing numerosity for each depth bin. R^2 = goodness of fit threshold at that specific depth (80th percentile), n = number of voxels within a depth bin after applying the R^2 threshold. D, H) Average tuning width and numerosity for each cortical depth bin.

Tuning width remains constant across cortical depth

Average tuning width and preferred numerosity did not vary consistently across cortical depth (Figure 3D, H, 4A). Average preferred numerosity and tuning width across depth ranged from 1.92 to 4.65 and 4.83 to 21.89 respectively. The Z-scored average tuning width across cortical depth decreased towards the cortical surface (mean polynomial fit parameter values: slope = 0.05, quadratic component = -1.48; Figure 4B), although this trend was not significant ($t(48)_{\text{slope}} = 0.03$, $p = 0.98$, $t(48)_{\text{quadratic}} = -0.82$, $p = 0.42$). The group average tuning width across cortical depth at numerosity 3, as sampled from the linear fits at each cortical depth (mean polynomial fit parameter values: slope = 0.04, quadratic component = -1.07; Figure 4C) did not significantly deviate from a horizontal, straight line: $t(46)_{\text{slope}} = 0.02$, $p = 0.99$, $t(46)_{\text{quadratic}} = -1.07$, $p = 0.58$. The same held for the group average tuning width across

cortical depth sampled at preferred numerosity 5 (mean polynomial fit parameter values: slope = -3.43, quadratic component = 3.10; Figure 4D), $t(46)_{\text{slope}} = -1.67$, $p = 0.10$, $t(46)_{\text{quadratic}} = 1.58$, $p = 0.12$. Results with a fixed (10%) explained variance threshold are virtually indistinguishable from the 80th percentile threshold (see Figure 4E-G). Notably, with the fixed 10% threshold the slope parameter of the polynomial fit in Figure 4H was significant, $p = 0.04$, compared to the former $p = 0.10$ (Figure 4D). No notable differences in cortical dept profiles were found between subjects with different anatomical data acquisitions (note particularly the absence of clustering in Figure 4A, E).

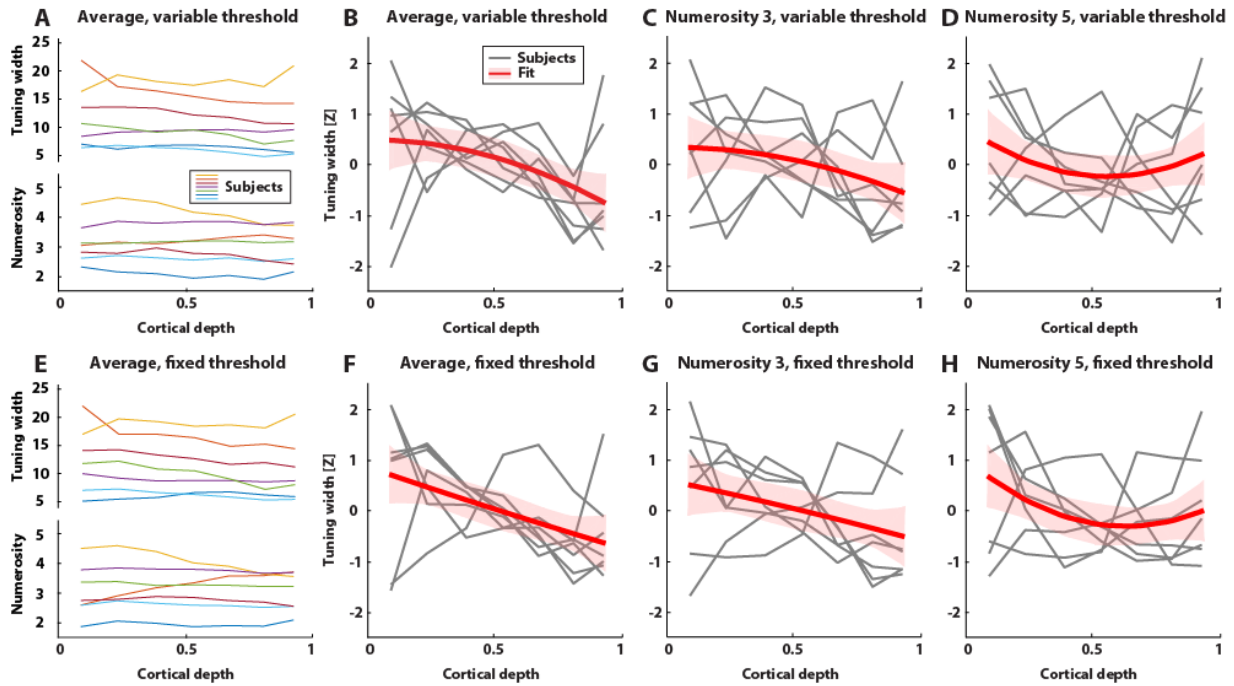


Figure 15: Tuning width generally does not vary across cortical depth. A-D) Results for 80th percentile R^2 (variable) threshold. E-H) Identical to A-D, but for a fixed threshold of $R^2 = 10\%$. A, E) Average preferred numerosity and tuning width across cortical depth bins for each subject. B, F) Z-scored average tuning width across cortical depth. Gray lines represent individual subjects. Red lines represent best second-degree polynomial fit. Shaded regions represent 95% confidence interval of the fit. C, G) Z-scored tuning width, sampled at numerosity 3 from the linear fits for each depth bin (red lines in Figure 3). Gray lines represent individual subjects. Red line represents best second-degree polynomial fit. Shaded regions represent 95% confidence interval of the fit. D, H) Same as C, G) but sampled at numerosity 5.

Discussion

We investigated information processing across cortical depth for higher-order visual processing. To this end, assessed tuning width and numerosity preferences across cortical depth in parietal cortex. We show that tuning width increases with numerosity. This increase is consistent with previous findings at lower resolutions (Harvey & Dumoulin, 2017; Harvey, Klein, et al., 2013). Additionally, we find that the estimated tuning width does not consistently change across cortical depth. This is inconsistent with what has been observed in the primary visual cortex (Fracasso, Petridou, et al., 2016). Even though we find a significant decrease across cortical depth for sampled numerosity 5 using fixed thresholding ($R^2 = 10\%$), we currently do not feel confident to draw any conclusions from this isolated finding, given the variability between thresholding schemes. Additional analysis should further substantiate these results.

The absence of a U-shaped tuning width profile across cortical depth may well indicate that laminar processing in association cortex is inconsistent with laminar processing in primary visual cortex. Primary visual cortex mainly receives ascending information directly from the lateral geniculate nucleus (LGN). However, the source of ascending information arriving in NPC1 is almost certainly more diffuse, potentially resulting in an absence of any tuning width changes across cortical depth. Moreover, NPC1 has been shown to be one of the later topographic numerosity maps in the processing hierarchy (Harvey & Dumoulin, 2017), potentially further reducing any differences across cortical depth as ascending information has already been processed. Further clues for substantial differences between numerosity and early visual processing arise from tuning width/pRF size patterns across respective processing hierarchies. In the visual system, a roughly five-fold increase of pRF size is observed when ascending in the processing hierarchy (Harvey & Dumoulin, 2011), while tuning widths remain relatively constant across topographic numerosity maps (Harvey & Dumoulin, 2017). This may reflect a fundamental difference in processing between visual and numerosity-responsive cortex that might be present across cortical depth as well. However, pRF sizes across cortical depth in the visual system have thus far only been investigated for primary visual cortex, so variations in this pattern may well be present along the visual hierarchy as well.

One potential explanation for the absence of a U-shaped tuning width profile across cortical depth might be that this pattern may be occluded by measurement noise. Tuning width between subjects varies by almost a factor of five, which might obscure to subtle trends in tuning across cortical depth being masked. However, Z-scoring the tuning width data mitigates the between-subject variation, showing no significant U-shape across cortical depth. Additionally, taking the average tuning width across cortical depth (Figure 4B, F) can obscure differences in tuning width profiles for different numerosities.

Another reason why a significant U-shaped profile was not observed, is that the data processing pipeline used might not be sensitive enough to detect it. Although this remains a possibility, near-identical methods have previously been used to show attention effects (Klein, Fracasso, van Dijk, et al., 2018) and pRF size changes (Fracasso, Petridou, et al., 2016) across cortical depth. These studies have revealed systematic variations across cortical depth, making it unlikely that the processing pipeline is not sensitive enough to pick up cortical depth-dependent variations in the current study. Moreover, we replicated the commonly found pattern of tuning width increases with preferred numerosity, while goodness of fit values were reasonable. Although these latter values were generally lower than in previous numerosity studies (Harvey & Dumoulin, 2017; Harvey, Klein, et al., 2013), this was to be expected as the signal-to-noise ratio (SNR) of the fMRI signal decreases significantly with increasing spatial resolution. Goodness of fit values for the sub-millimeter experiments by Klein and colleagues (2018) and Fracasso et al (2016) were on average higher than for the current study. However, these measurements were all performed in primary visual cortex. Cognitive tasks generally have a lower inherent SNR, requiring more data to be collected to reach the same statistical power as in the early visual cortex (Harvey, Klein, et al., 2013). This can be achieved for the current study by collecting even more data from the existing subjects and increasing the number of subjects.

The resolution of the collected fMRI data was 0.93 mm isotropic. This resolution was chosen to optimize the repetition time (1200 ms), while remaining in the sub-millimeter domain. This short repetition time resulted in the higher statistical power required here as all data had to be collected in one session because registration between sessions is undesirable for sub-millimeter fMRI. Additionally, numerosity mapping experiments have a relatively low SNR by default. The spatial resolution of the fMRI data combined with the local thickness of the cortex allows for the definition of approximately 4 cortical depth bins. Due to the curvature and the location of the gray matter on

the acquisition grid, more depth bins can be defined. However, due to the limited number of bins, more complex trends across cortical depth may be difficult to identify.

To further differentiate different explanations for the found differences in receptive field profiles across cortical depth between numerosity-selective and early visual cortex, future research may want to focus on comparing tuning width profiles across cortical depth between topographic numerosity maps, and extending pRF size profiles across cortical depth to visual field maps outside primary visual cortex.

Conclusion

We use sub-millimeter fMRI to investigate numerosity preference across cortical depth and found robust modelling results at a sub-millimeter, single-voxel level. We find that tuning width increases with preferred numerosity within each depth bin. We show that the tuning width profile across cortical depth is mostly constant. We replicate previously identified tuning width increases with preferred numerosity, and extend this across cortical depth. The flat tuning profile is inconsistent with an early visual cortex-based model and may indicate fundamental differences in laminar organization between early visual and association cortex.

Chapter 5

Intracranial recordings show evidence of numerosity tuning in human parietal cortex

van Dijk, J.A., de Jong, M.C., Piantoni, G., Fracasso, A., van Steensel, M., Petridou, N., & Dumoulin, S.O., Intracranial recordings show evidence of numerosity tuning in human parietal cortex (in preparation)

Acknowledgement of author contributions

AF and SOD conceptualized the experiment; AF, MCdJ and JAvD designed the numerosity stimuli; MvS and GP collected the data; JAvD, GP, and MCdJ analyzed the data; all authors contributed to and reviewed the manuscript; JAvD prepared all figures; SOD and NP provided general supervision and guidance throughout.

Abstract

Numerosity -the set size of a group of items- perception is a trait shared across numerous species. Electrophysiological recordings in animals have shown the presence of numerosity-selective neuronal populations. In humans, numerosity-selective neuronal populations have been identified using functional magnetic resonance imaging (fMRI). However, the limited temporal resolution of fMRI inhibits the study of temporal characteristics of numerosity-selective neuronal populations. Here we use intracranial recordings to investigate numerosity tuning in humans, focusing on high-frequency transient activations. This technique combines a high spatial resolution with an excellent temporal resolution. We find numerosity-tuned responses at a parietal site that is in line with previous fMRI studies. Neuronal populations at this location did not respond to visual stimuli per se (faces, houses, letters), in contrast to several occipital sites. This further corroborates the specificity of the numerosity tuning of this parietal site. We show that the response profile of parietal numerosity-tuned neuronal populations is distinctly different from responses to the same stimuli in the occipital lobe, and further link fMRI results and electrophysiological recordings.

Introduction

Numerosity refers to the set size of a group of items. Its perception is implicated in many cognitive functions (Burr & Ross, 2008) and decision-making processes such as multiple object tracking (Piazza, 2011), mathematics (Dehaene, 1997; Halberda et al., 2008; Harvey, 2016), decision making (Nieder & Miller, 2003), and dividing attention (Knops et al., 2014). Behavioral studies have shown that numerosity perception is a trait shared across a wide range of species, including human infants (Dehaene, 1997), children (Cantlon et al., 2009), zebra fish (Potrich et al., 2015), non-human primates (Brannon & Terrace, 1998; Hauser et al., 2000, 2003), cats (Pisa & Agrillo, 2009), and corvids (Ditz & Nieder, 2016a). Neuronal populations that are selective for numerosity have been found using electrophysiological recording in corvids (Ditz & Nieder, 2015, 2016b), monkeys (Nieder, Freedman, & Miller, 2002; Nieder & Miller, 2003, 2004; Sawamura, Shima, & Tanji, 2002; Tokita & Ishiguchi, 2010), and using depth electrodes in humans (Kutter et al., 2018). Studies using functional magnetic resonance imaging (fMRI) have found a network of cortical areas that are involved in numerosity processing (Cantlon et al., 2009; Dehaene et al., 1999; Eger et al., 2009; Knops et al., 2014; Piazza et al., 2004; Pinel et al., 1999). Recent fMRI studies have revealed that a number of areas in locations involved in numerosity processing are topographically organized, with numerosity preference gradually changing along the cortical surface (Harvey & Dumoulin, 2017; Harvey, Klein, et al., 2013). Neuronal populations in these topographic regions show a large response for stimuli of a specific numerosity and respond less and less when the numerosity of a stimulus is farther from the preferred numerosity of that cortical location. This is in line with electrophysiological recordings for numerosity in animals, where spiking rates of (a group of) numerosity-selective neurons decrease with distance from the preferred numerosity (see Nieder, 2018 for a review). Moreover, single-neuron recordings using depth electrodes in human medial-temporal lobe also show this pattern (Kutter et al., 2018).

Recordings of topographically organized numerosity tuned neuronal populations in humans have so far been carried out using fMRI. However, temporal properties of numerosity-related responses are difficult to study with fMRI. Recordings at high temporal resolutions in the human brain are usually limited to magneto- and electroencephalography (MEG and EEG) which arguably lack the spatial resolution to find fine-grained spatial patterns of numerosity-tuning as found with fMRI. Intracranial recordings (electrocorticography; ECoG) combine excellent temporal (ms range) and good spatial (mm range) resolution and are an ideal tool to study temporal characteristics of numerosity tuning at a proper spatial scale in the awake and healthy human brain. This technique, however, is invasive and therefore recording opportunities are sparse. Thus far, ECoG in humans has been used to identify neuronal populations preferring mathematical operations (Daitch et al., 2016), but has not been used to study numerosity-tuned responses.

Here, we use electrocorticography (ECoG) to measure responses to visual stimuli depicting different numerosities. To facilitate comparison with fMRI findings, we used stimuli that were identical to those used in previous fMRI studies that have found numerosity-tuned cortical areas (Harvey & Dumoulin, 2017; Harvey, Klein, et al., 2013). We find a numerosity-selective response pattern in a location corresponding with the most robustly identifiable numerosity-selective topographic map in fMRI studies. We provide several control conditions showing that the response preferences of this electrode are not in line with purely visual, or category specific visual stimuli, further supporting the numerosity-selective nature of this response pattern.

Methods

Subject information

Subjects were two patients with drug-resistant epilepsy and candidate for resective surgery. They were admitted for intracranial epilepsy monitoring at the University Medical Center Utrecht. They were implanted with subdural ECoG electrode grids as the standard diagnostic procedure for surgical treatment. The study was approved by the ethical committee (METC) of the University Medical Center Utrecht, in accordance with the Declaration of Helsinki (2013), and patients signed informed consent.

Subject 1 was a 19-year old, left-handed female. Electrode grids were located on the left lateral surface of the brain, covering most of the temporal lobe, large parts of the occipital lobe, and part of the parietal lobe (Figure 1A). Studies for this subject were conducted under METC protocol number: NL50036.041.14.

Subject 2 was a 15-year old, right-handed female. Electrode grids were located on the right lateral and medial surface of the brain, covering part of the medial and most of the lateral occipital lobe, partially extending to the superior and inferior temporal lobe (Figure 1B). Studies for this subject were conducted under METC protocol number: NL48022.041.14.

Stimuli

Visual stimuli were presented to the subject on an NEC MultiSync E221N, 21.5-inch IPS monitor, with a resolution of 1920x1080 pixels, driven by an Acer Aspire E5-573G laptop. The screen was viewed at approximately 70 cm distance. All stimuli were presented using Presentation® software (version 18.0, Neurobehavioral Systems, Inc., Berkeley, CA, www.neurobs.com).

Numerosity stimuli

Mean luminance gray background with a large diagonal red cross was presented at all times. This cross aided fixation and ran from one corner of the screen to the other. Stimuli consisted of groups of circles, randomly distributed within an invisible circle with a 50-pixel radius. The number of circles per stimulus display included all integers from 1 to 7, and 20. Numerosity 20 was chosen because it is expected to be well outside the response range of neuronal populations responding most to small numerosities, while neurons responding to just contrast energy should respond most strongly to this energy-rich condition (Harvey & Dumoulin, 2017). The total surface area of each group of circles was constant, hence the circles were larger when the stimulus display contained fewer of them. On regular trials, the circles were black. In approximately 10% of the trials (two per numerosity on average), white circles were presented instead of black. Subjects had to respond to these trials by pressing a button. No numerosity-related judgments were required.

Stimuli were presented for 250 ms, followed by an inter-stimulus interval (ISI) of 600 ms during which only the mean luminance gray screen with the fixation cross was presented. Numerosities 1 to 7 were displayed sequentially in ascending order, then in descending order with six consecutive presentations per numerosity (Figure 1C). These ascending and descending sweeps were separated by twelve presentations of numerosity 20. The full sequence (ascending 1-7, then 20, descending 7-1, then 20) was repeated twice within each run. Each run started and ended with a 1200 ms mean luminance gray screen with a fixation cross, resulting in a total presentation time of 186 s per run. The stimulus sequence is near-identical to those used in recent numerosity-related fMRI paradigms (Harvey et al., 2013; Harvey & Dumoulin, 2017). This numerosity stimulus paradigm is further referred to as 'fixed order'.

For subject 2, an additional numerosity stimulus paradigm was added. Stimuli were identical to the fixed order paradigm, but stimuli were presented in a semi-randomized order, so that no two consecutive stimuli displayed the same numerosity. Additionally, a variable ISI of 650-950 ms (mean ISI = 800 ms) was introduced instead of the fixed ISI, and the number of presentations (24) was the same for all numerosities. Each run started and ended with 1200 ms of mean luminance. Total presentation time for one run was 194.4 s. This stimulus paradigm is further referred to as ‘random order’.

Visual category stimuli

To control for visual stimulation per se, we compared responses during our numerosity experiment with responses during an experiment in which high-pass filtered images of faces, individual letters, or houses were presented on a mean luminance gray background. Each image measured 330 x 330 pixels and was presented in the center of the screen. Each presentation lasted 500 ms, with a variable ISI lasting 690-1250 ms during which a mean luminance gray screen was presented. The total number of presentations per run was 36 (12 per stimulus category), with a total average run time of 52.9 s per run.

Data acquisition

Arrays of subdural ECoG electrodes were implanted for a week as part of epilepsy treatment, for localization of the epileptic focus. Grid electrodes (AdTech, Racine, WI) had a measurement surface of 2.3 mm diameter, with 1 cm inter-electrode spacing, and were positioned directly on the cortical surface. A reference electrode was positioned extra-cranially on the mastoid bone. Electrode signals were inspected by a clinical professional and excluded from the analysis if they showed major recording artifacts or excessive epileptic activity. A total of 80 implanted electrodes were selected for this study for subject 1, and 56 electrodes for subject 2, based on cortical location. Data were acquired using a 128-channel recording system (Micromed, Treviso, Italy) with a 2048 Hz sampling rate and band-pass filtered between 0.15–536 Hz. Electrodes were localized from an MRI co-registered cortical tomography (CT) and projected to the cortical surface of each subject (Hermes, Miller, Noordmans, Vansteensel, & Ramsey, 2010). We collected one fixed order numerosity and six visual category runs for subject 1. For subject 2, we collected one fixed order and two random order numerosity runs, and two visual category runs.

Data preprocessing

All data processing was performed using MATLAB (2018a, Mathworks, MA, USA) and the Fieldtrip toolbox (Oostenveld, Fries, Maris, & Schoffelen, 2011). Electrodes on the parietal (for subject 1 only), temporal, and occipital lobes were selected for analysis. For subject 2, three additional electrodes were excluded from further analysis due to poor signal quality. Electrodes included in the analysis were not located over the clinically defined seizure focus. All ECoG time course data of each subject were first notch-filtered at 50 Hz and 2 octaves (100 and 150 Hz, filter width of 3 Hz) to remove line noise and subsequently re-referenced to the common average of all included electrodes.

Numerosity experiment processing

All numerosity data were epoched from 500 ms before until 1000 ms after stimulus onset. Then, the first presentation of each numerosity block was removed to remove any numerosity change onset effects. This left 20 presentations per numerosity for numerosities 1-7, and 40 presentations of numerosity 20 for further analysis. We first removed the evoked signal (average over all epochs with the same numerosity) for each numerosity from the common average-corrected signals. Next, we calculated the power for each epoch using a fast Fourier transform (FFT) over a frequency range of 2-122 Hz in steps of 2 Hz with a sliding window width of 300 ms, tapered with a Hanning window to attenuate edge effects. The time-window of interest lay between 200 ms before and 700 ms after stimulus onset, in steps of 50 ms. The resulting power data were then normalized, so that the amplitudes at each frequency contributed equally to the resulting signal (Miller, Sorensen, Ojemann, & Den Nijs, 2009; Miller, Zanos, Fetz, Den Nijs, & Ojemann, 2009). These normalized data for each presentation were subsequently baseline-corrected by subtracting the temporal mean over 200 ms to 50 ms preceding stimulus onset. To identify electrodes and frequency ranges of interest, average power spectral density (PSD) for each numerosity was plotted for each electrode. All further analyses were performed on the high frequency band (HFB; 60-120 Hz). Temporal responses to each numerosity were represented by averaging over the HFB for further analysis. Subsequently, tuning preferences were identified by taking the mean response for each numerosity over the HFB and a time window 0-300 ms after stimulus onset. Initial selection of electrodes for further analysis was based on visual inspection of these mean responses. Two electrodes were selected for s1. More electrodes showed responses, but their response profiles did not differ from occipital electrode s1-Oc1. Three electrodes were selected for s2, with some other electrodes showing similar response patterns. Electrode s1-Oc2 was selected based on high responses to all stimulus types in the control experiment. The responses of the selected electrodes were then compared by performing a general linear model (GLM) analysis with the response to numerosity 20 as baseline, and each other numerosity as a categorical variable, defined as the difference between the response to that numerosity and the response to numerosity 20.

Control experiment processing

All processing steps for the visual categories data were identical to the numerosity data. However, exact parameters differed for some steps. These differences are listed next. If analysis steps are not mentioned, the parameters were identical to the numerosity data analysis.

Initial epochs were defined starting 500 ms before until 1750 ms after stimulus onset, and all epochs were retained for further analysis. The time-window of interest was 200 ms before until 1250 ms after stimulus onset. Mean responses across time and frequency range of interest were taken from 150-600 ms after stimulus onset. Responses between categories were then compared using a GLM analysis with the response to letters as baseline, and each stimulus category as categorical variable.

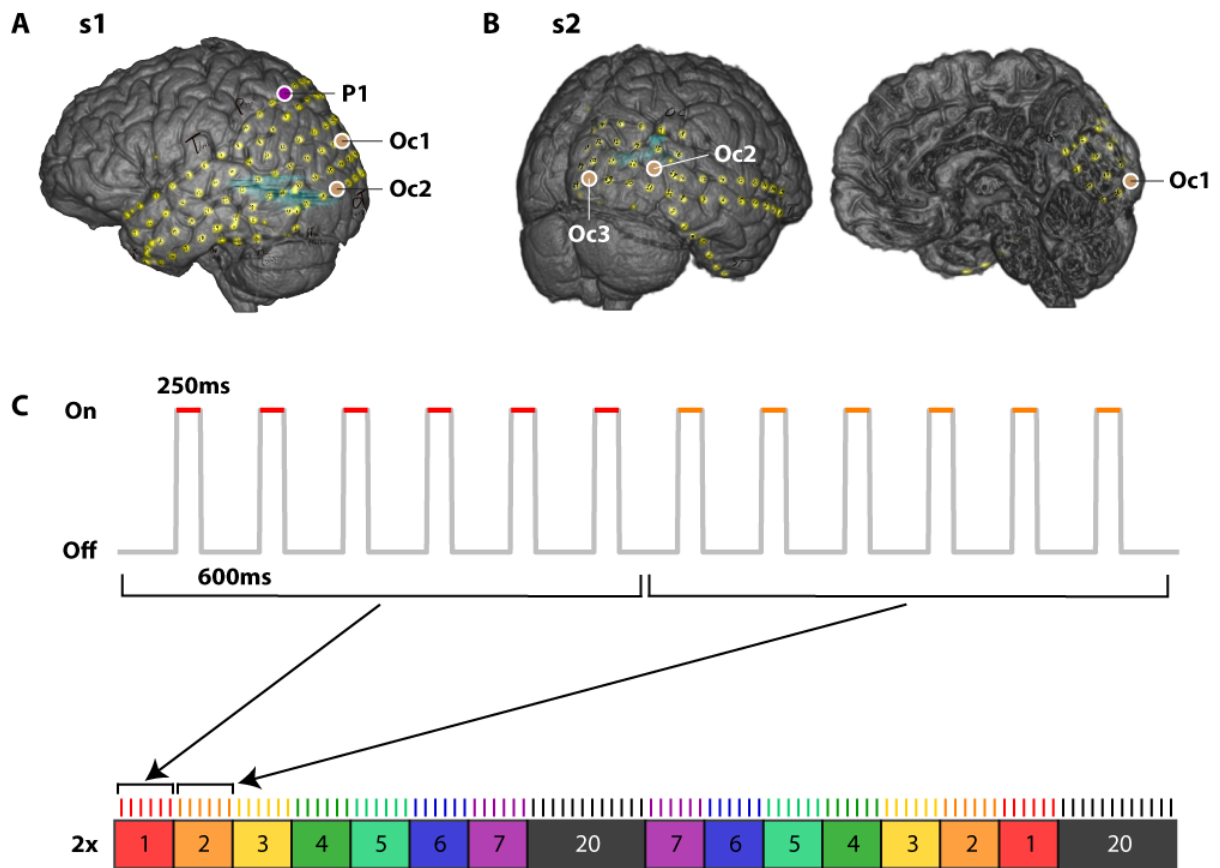


Figure 16: Electrode grid locations and stimulus sequence for the numerosity experiment. A) Lateral view with electrode locations (yellow dots) for subject 1. Purple circle indicates the location of parietal electrode 1. Light brown circles indicate the locations of occipital electrodes 1 and 2. B) Caudal-lateral and medial views with electrode locations (yellow dots) for subject 2. Brown circles indicate the locations of occipital electrodes 1, 2, and 3. C) Stimulus sequence. Stimuli were presented for 250 ms, with a 600 ms inter-stimulus interval. Horizontal colored bars in the upper half and vertical colored bars in the lower half of the panel represent the presented numerosity, corresponding to the colored block sequence. Each colored horizontal or vertical bar represents one stimulus presentation. Stimuli were presented sequentially, with six (numerosity 1-7) or twelve (numerosity 20) consecutive presentations. The colored block sequence was repeated four times per run.

Results

High-frequency band power reveals numerosity tuned responses in parietal cortex

Parietal electrode 1 in patient 1 (s1-P1) PSD-plots showed a large response across the HFB to numerosity 7 and a smaller response to numerosities further away from 7 (Figures 2A and 3A, see full power spectrum per numerosity in Figure 3C). The response to numerosity 7 showed a clear peak around 150 ms after stimulus onset (Figure 2B). In line with existing fMRI studies, we performed a GLM analysis with 20 as baseline and numerosities 1-7 as categorical variables, showing that the responses of s1-P1 to numerosity 7 were significantly higher than for numerosity 20, $t(171) = 2.95$, $p = 0.004$, even though these numerosities are relatively close to each other in logarithmic space in which numerosity response modelling is commonly performed (Dehaene & Changeux, 1993; Nieder & Miller, 2003, 2004; Piazza et al., 2004). Responses to numerosity 20 were significantly higher than 0, $t(171) = -2.24$, $p = 0.03$. Responses to numerosity 1 were significantly lower than for numerosity 20, $t(171) = -2.33$, $p = 0.02$. Responses to other numerosities were not significantly different from 20,

$t(171) = -1.75$ - 1.70 , $p = 0.08$ - 0.95 . The same response pattern was observed in a split-half analysis (Figure S1). We thus observe a clear tuning to numerosity 7 in s1-P1.

Comparing the response of s1-P1 to numerosity 7 with its response to visual category stimuli shows that s1-P1 selectively responds to numerosity, as responses to face, letter, or house-stimuli are not significantly different from 0, $t(212) = -0.08$, $p = 0.93$ (Figure 3B, see Figure S2 column A for more elaborate results for the visual category stimuli).

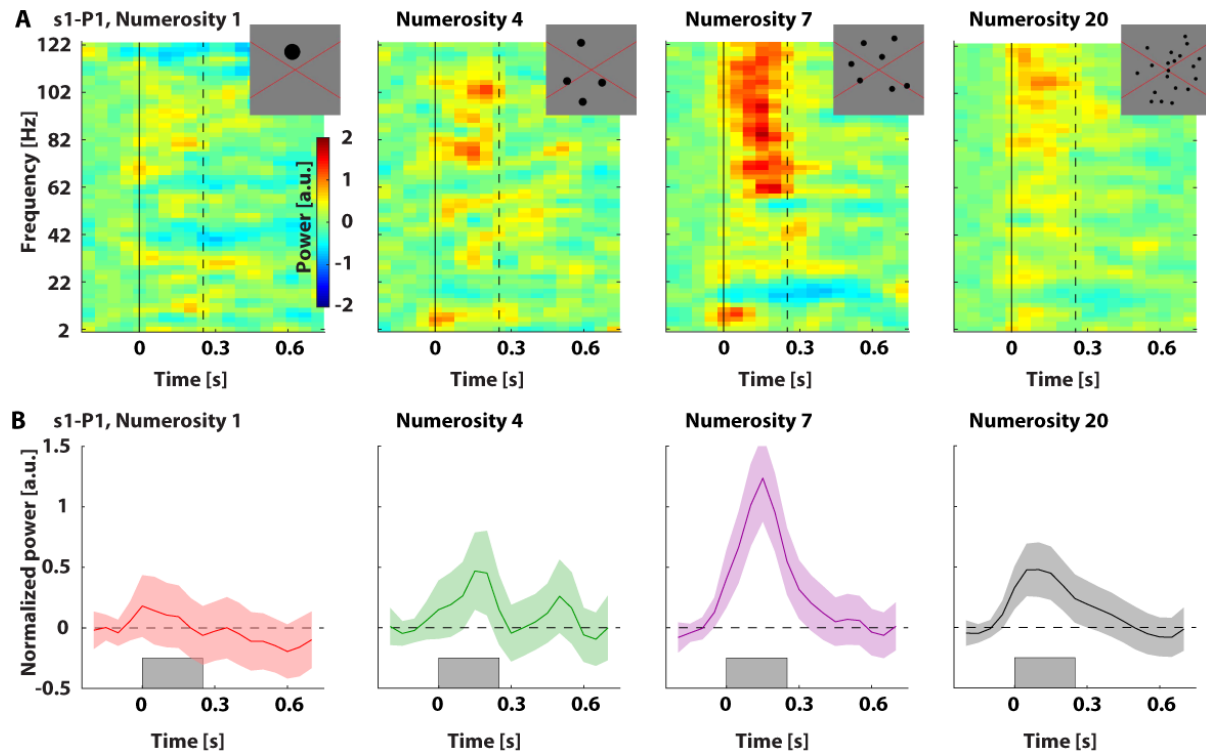


Figure 17: Responses to numerosity stimuli for subject 1. A) Normalized power spectral density across frequency and time for parietal electrode 1 for numerosity 1, 4, 7, and 20 (example stimuli as insets). Solid black lines represent stimulus onset, dashed black lines represent stimulus offset (total presentation time per epoch: 250 ms). B) Mean normalized power in the high frequency band (60-120 Hz) over time. Shaded regions represent standard error of the mean across stimulus repetitions. Gray rectangles represent when a stimulus was presented.

Response patterns in occipital cortex do not show numerosity tuning

Response patterns in occipital cortex were either tuned for stimulus energy, or were untuned, i.e. responding to all numerosities. Electrodes s1-Oc1 (Figure 3D) and s1-Oc2 (Figure 3E) did not show numerosity-tuned responses. Electrode s1-Oc1 showed a general response for numerosity 4 and higher. A GLM with 20 as baseline and numerosities 1-7 as categorical variables revealed that the response to numerosity 20 was higher than the responses to 1-3: $t(171) = -2.24$, $p = 0.03$ (numerosity 1), $t(171) = -2.30$, $p = 0.02$ (numerosity 2), and $t(171) = -3.40$, $p = 0.0008$ (numerosity 3). Responses to numerosity 20 were significantly higher than 0, $t(171) = 4.60$, $p < 0.001$. Responses to numerosity 4-7 did not differ significantly from 20, $t(171) = -0.71$ - 0.21 , $p = 0.48$ - 0.84 . Responses for s1-Oc2 did not show any consistency between numerosities, with only the responses to numerosity 3 being significantly lower than the ones to numerosity 20, $t(171) = -2.48$, $p = 0.01$. All other responses were not significantly different from 20, $t(171) = -1.67$ - 0.97 , $p = 0.10$ - 0.61 .

In contrast to the parietal numerosity-tuned electrode s1-P1, occipital electrodes did respond to stimuli in the control experiment (face, letter, and house stimuli; see Figure S2). Responses of s1-Oc1 in the control experiment were significantly higher than 0, $t(212) = 8.45$, $p < 0.001$, and significantly higher for letters than for faces ($t(212) = -2.82$, $p = 0.005$) or houses ($t(212) = -4.33$, $p < 0.001$). Responses for s1-Oc2 were consistently higher than 0, $t(212) = 8.09$, $p < 0.001$, and were not significantly different between stimulus categories (letters versus faces $t(212) = -0.47$, $p = 0.66$; letters versus houses $t(212) = -1.34$, $p = 0.18$). In summary, s1-Oc1 and s1-Oc2 do not exhibit numerosity-tuned response patterns, but do show responses to face, letter, and house stimuli.

Response patterns for subject 2 (s2-Oc1, s2-Oc2, and s2-Oc3) were inconsistent with patterns expected for numerosity tuning. Responses for fixed order numerosity stimuli were variable for s2-Oc1 (Figure 3F) and s2-Oc3 (Figure 3H), but consistent between numerosities for s2-Oc2 (Figure 3G). For the random order version of the numerosity experiment, response patterns for s2-Oc1-3 (Figure 3I-K) showed much clearer trends.

For s2-Oc1 (Figure 3F, I), responses to 20 were higher than all other numerosities except 5 for the fixed order run, and higher than all other numerosities for the random order runs with responses steadily increasing with numerosity. A GLM with 20 as baseline and numerosities 1-7 as categorical variables revealed that for the fixed order run, responses to 20 were significantly higher than responses to numerosity 1, 2, 4, and 7, $t(154) = -3.57$, -3.16 , -2.21 , -2.18 respectively, with $p < 0.001$, $p = 0.002$, 0.03 , 0.03 . For the random order runs, responses to 20 were significantly higher than those to numerosity 1-4, $t(154) = -3.78$, -3.11 , -2.80 , -2.18 respectively, with $p < 0.001$, $p = 0.002$, 0.006 , 0.03 . Thus, responses consistently increased with numerosity for the random order runs, consistent with a response increase with increasing stimulus energy. This pattern was less clear for the fixed order run.

For s2-Oc2 (Figure 3G, J), responses were consistent between numerosity and fixed and random order runs. A GLM showed that responses to 20 were significantly higher than 0 for both stimulus orders, $t(154) = 13.57$, 10.10 (fixed and random order respectively), $p < 0.001$. For the fixed order run, responses to numerosity 2 were on average significantly lower than for 20, $t(154) = -2.32$, with $p = 0.02$ with a difference of 0.18 between the two. No numerosity responses were significantly different from 20 for the random order runs. In summary, s1-Oc2 did not show a numerosity-tuned response pattern, but rather responded to all numerosity stimuli virtually equal. This did not differ between run types.

For s2-Oc3 (Figure 3H, K), responses are highest for numerosity 20 for both the fixed and random order runs. For the fixed order run, responses to numerosity 20 are on average significantly higher than all other responses except numerosity 6, $t(154) = -4.04$ -2.28 , $p < 0.001$ 0.03 . For numerosity 6: $t(154) = -1.89$, $p = 0.06$. The response pattern is inconsistent across numerosities, with neither a constant increase, nor a constant overall response, though still responsive to all visual stimuli. For the random order runs, responses to numerosity 20 were on average higher than all numerosities, $t = -6.00$ -2.87 , $p < 0.005$. Responses generally increased with numerosity. To summarize, s2-Oc3 consistently responds most to numerosity 20, with a general increased response with numerosity for the random order runs.

All in all, response patterns of electrodes in subject 2 are inconsistent with numerosity-tuned responses. However, response patterns of s2-Oc1 and s2-Oc3 correspond with responses of neuronal populations sensitive to stimulus energy, as increasing numerosity of a stimulus display increases its stimulus energy. This type of response is typically found in the visual system (Harvey & Dumoulin, 2017). Responses of s2-Oc2 are consistent with neuronal populations that respond non-selectively to

any transient visual information. Note that the coverage for s2 differed from s1. For s2, coverage did not include the equivalent of the parietal region covered by s1-P1.

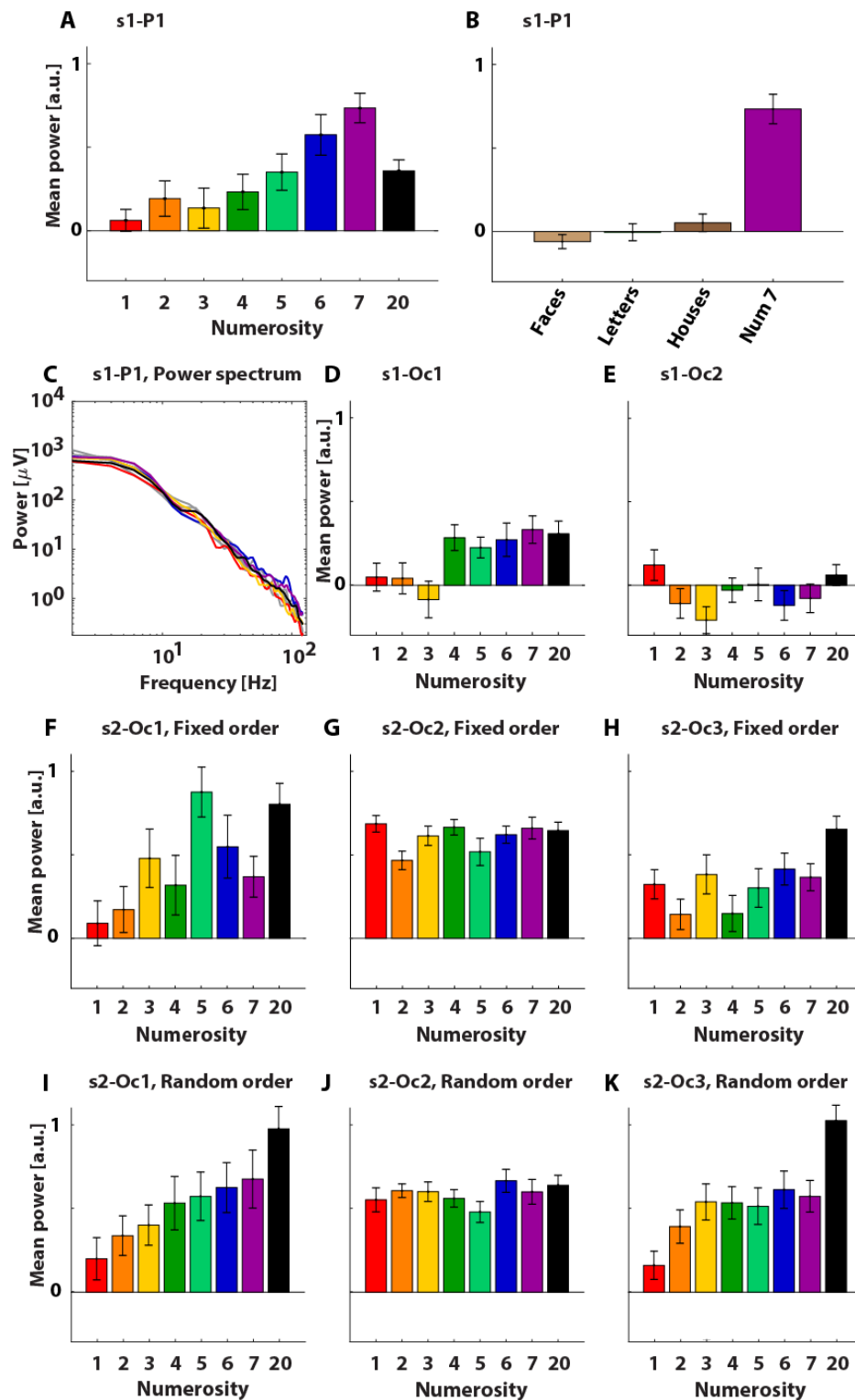


Figure 18: Average responses to numerosity and visual category stimuli. A) Mean normalized power across high gamma (60-120 Hz) across a time window 0-300 ms after stimulus onset for electrode s1-P1. B) Electrode s1-P1: mean normalized power across high gamma (60-120 Hz) across 150-600 ms after stimulus onset for visual category stimuli and mean normalized power as in 3A for numerosity 7. C) Power spectrum log-log plot averaged over epochs (0-300 ms after stimulus onset) with the same presented numerosity for s1-P1. D-K) Mean normalized power across high gamma (60-120 Hz) across

a time window 0-300 ms after stimulus onset for several electrodes in s1 (D, E) and s2 (F-K). F-H) For fixed-order numerosity stimulus presentation, subject 2. I-K) Same electrodes as in F-H, for random-order numerosity stimulus presentation.

Discussion

We provide intracranial recordings of numerosity-tuned neuronal populations in humans. We show that the response pattern of this population is distinct from the response pattern of electrodes that visually responsive per se, which showed either a flat or an increasing response with numerosity. Furthermore, we show that the numerosity-tuned population is unresponsive to images of faces, letters, and houses.

With the identification of numerosity-tuned neuronal populations, we attempt to bridge the gap between non-human electrophysiology and human fMRI. Thus far, recordings in humans have been limited to fMRI, which has a limited temporal resolution. The current recordings provide high spatial and excellent temporal resolution, making it possible to look at transient responses of numerosity-tuned neuronal populations in humans. Additionally, intracranial recordings measure a different aspect of neuronal activity when compared to fMRI, with ECoG recording electric signals (similar to electrophysiology, but in humans) and fMRI measuring the hemodynamic consequences of neuronal activity. Even though these fMRI signals are correlated with HFB power (Hermes et al., 2012; Manning, Jacobs, Fried, & Kahana, 2009), the relationship between the two is not completely clear.

The location of the numerosity-tuned electrode is consistent with the most robust numerosity map identified in previous fMRI results (Eger et al., 2009; Harvey & Dumoulin, 2017; Knops et al., 2014; Piazza et al., 2004). Moreover, the response profile of the parietal numerosity-tuned neuronal population was distinctly different from the response profiles in occipital locations, for both the numerosity and faces/houses/letters control experiment.

Even though the current results are indicative of numerosity-tuned responses in the human parietal cortex, the identified numerosity-tuned neuronal populations underlie only a single electrode in a single subject. A more parietal-frontal coverage would be desirable to cover more locations previously identified using fMRI. A previous study using ECoG also shows that there are neuronal populations selective for mathematical tasks in these regions (Daitch et al., 2016). Additionally, having the aforementioned coverage on the right hemisphere would be optimal, as topographic numerosity maps are more robust in this hemisphere (Harvey & Dumoulin, 2017; Harvey et al., 2013). However, electrode grid coverage is entirely dependent on clinical purposes, greatly reducing the possibility of covering these exact locations and limiting the available time to collect data.

As the numerosity stimuli for subject 1 -in which we identified the numerosity-tuned electrode- were presented in a predictable order, some order effects might have been present in the data. To reduce these effects, we removed every first presentation from a stimulus block with the same numerosity. However, these potential order effects combined with the fact that all data came from a single run, make replication with a (semi-) random presentation order over multiple runs desirable.

Conclusion

We provide intracranial recordings of numerosity-tuned neuronal populations in human parietal cortex, thereby linking animal electrophysiology and fMRI findings on numerosity tuning. Moreover, we show that the response profile of parietal numerosity-tuned neuronal populations is distinctly different from responses to the same stimuli in the occipital lobe.

Supplementary information

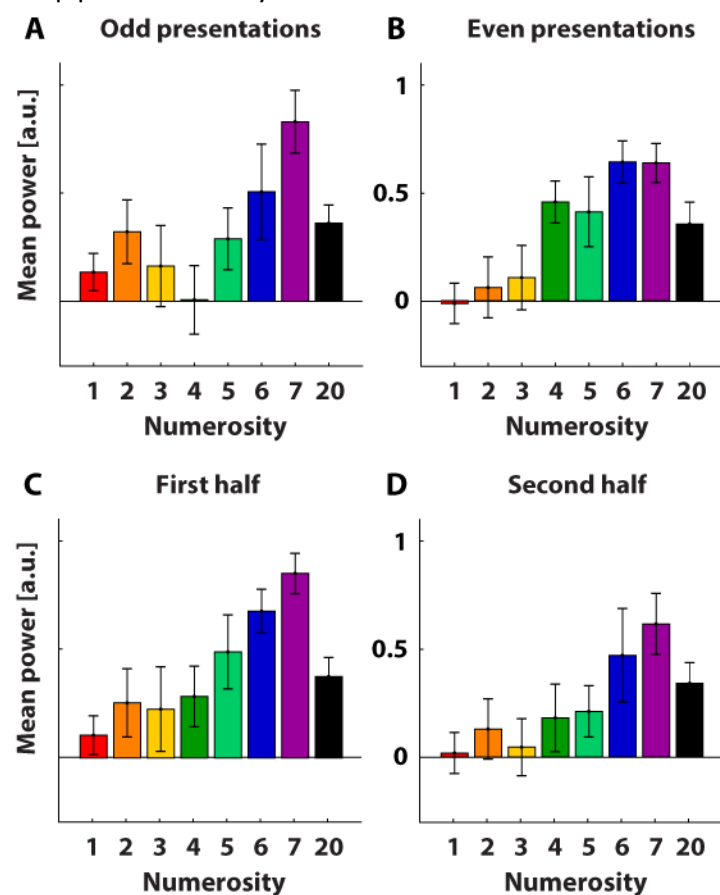


Figure S 5: Split half analysis of responses of parietal electrode 1 (s1-P1) for all numerosity stimuli shows a consistent response preference for numerosity 7. Mean power across high frequency band (60-120 Hz) across a time window 0-300 ms after stimulus onset for odd (A) and even (B) presentations, and for the first (C) and second (D) half of the run.

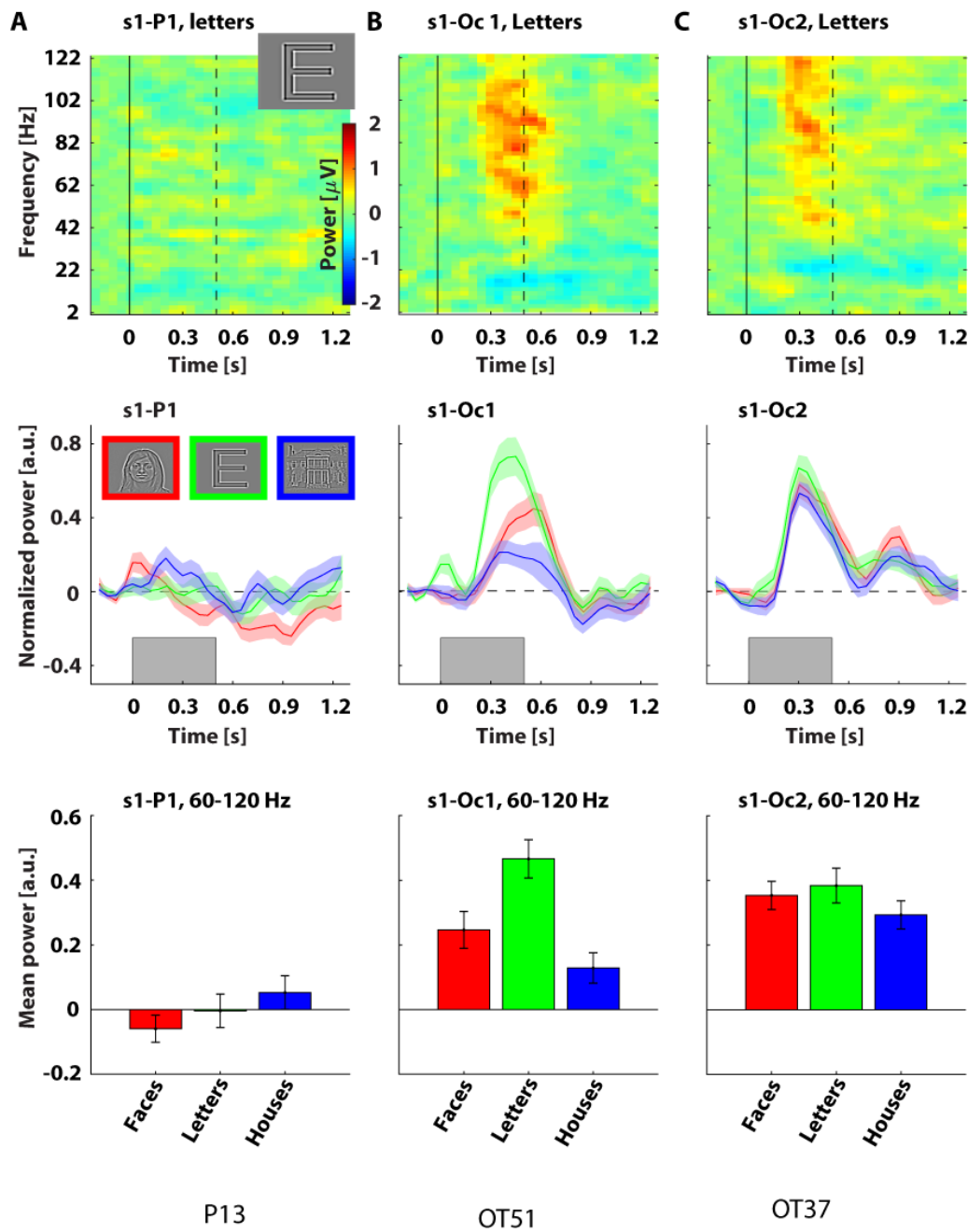


Figure S 6: Responses to face, letter, and house stimuli for subject 1. A-C) Different columns represent different electrodes (s1-P1, s1-Oc1, s1-Oc2) Top row: Normalized power spectral density across frequency and time for three electrodes for epochs containing letter presentations. Middle row: Mean normalized power in the high frequency band (60-120 Hz) over time. Different trace colors represent different stimulus condition: faces, letters, and houses (see inset). Shaded regions represent standard error of the mean across stimulus repetitions. Gray rectangles represent when a stimulus was presented. Bottom row: Mean power across the high frequency band (60-120 Hz) across 150-600 ms after stimulus onset. Different colors represent different stimulus conditions. The numerosity-selective electrode s1-P1 (column A) does not show a significant response to any of the stimulus categories. Occipital electrode s1-Oc1 (column B) shows a clear preference for letter stimuli, while also responding to general visual information from numerosity stimuli (see Figure 3D). Occipital electrode s1-Oc2 (column C) shows a general response for all three stimulus categories, while not responding to numerosity stimuli (see Figure 3E).

Chapter 6

General discussion

In this thesis, I have discussed how information processing streams in the human brain are organized across cortical depth, and methods that we can use to investigate this. Ultra-high field sub-millimeter (f)MRI has seen significant development over the last ten years (for reviews, see De Martino et al., 2018; Dumoulin, Fracasso, van der Zwaag, Siero, & Petridou, 2018; Lawrence, Formisano, Muckli, & de Lange, 2017; Petridou & Siero, 2017; Self & Roelfsema, 2017; Stephan et al., 2019). So much so, that it is now possible -for the first time in history- to study laminar information processing in humans without having to perform invasive procedures to get a high enough spatial resolution. We have seen that, although laminar fMRI is very promising, it is difficult to perform and there are several significant challenges we need to overcome, both in terms of data acquisition and analysis. Although analysis techniques from regular-resolution fMRI can largely be used for laminar fMRI, there are potential complications. One of the main complications is that, due to directional blood draining across cortical depth, the measured BOLD signal from each neuronal population is not only dependent on the signal from that population, but also on the fMRI signal from deeper-lying neuronal populations (Koopmans et al., 2011; Markuerkiaga et al., 2016). Traditional fMRI analysis techniques assume that the signals from two different neuronal populations are independent. Therefore, these techniques might not be applicable for laminar fMRI, potentially resulting in a biased picture of activation patterns. One of the fundamental assumptions of most analysis techniques is that the relationship between neuronal activation and the measured signal is linear. I have assessed the requirements for this assumption in **Chapters 2 & 3**.

While early visual and (sensori)motor processing at the laminar level is relatively well-studied (e.g. De Martino et al., 2013; Fracasso, Petridou, & Dumoulin, 2016; Huber et al., 2014; Kok, Bains, Van Mourik, Norris, & De Lange, 2016), much is still unknown about laminar processing for any higher-order processes. These processes are most easily studied in humans, as they can easily comply with, and respond to, complex instructions that are (usually) essential in studying higher-order processes. With laminar fMRI, it is now possible to start investigating laminar processing of higher-order information. In **Chapter 4**, I used laminar fMRI to study higher-order information processing in the form of numerosity-tuning properties across cortical depth. In **Chapter 5**, I have investigated transient numerosity-tuned responses using ECoG and compared the numerosity response profiles between numerosity-selective and visual cortex.

BOLD-response linearity holds for laminar fMRI of the visual system

The linearity between neuronal activation and the measured BOLD signal can be confirmed by assessing the two main assumptions for a linear system: scaling, and temporal additivity. The scaling assumption tells us that the signal measured from a stimulus that elicits e.g. twice the neuronal response amplitude, should be twice the original signal amplitude. The temporal additivity assumption tells us that the signal measured from two stimuli being presented close in time, should be equal to the sum of measured signal caused by each stimulus separately. For this summation, the second signal is shifted by the amount of time between the two stimuli and added to the first response. The linearity of the BOLD response has been shown to (mostly) hold for regular fMRI (see e.g. Boynton, Engel, Glover, & Heeger, 1996; Boynton, Engel, & Heeger, 2012; Cohen, 1997; Friston, Jezzard, & Turner, 1994; Miezin, Maccotta, Ollinger, Petersen, & Buckner, 2000).

Although applying laminar fMRI to neuroscientific questions is the ultimate goal, it is important to first confirm that the two assumptions for a linear system hold for this extremely promising field. This way, we can make sure that our interpretations and measurements are indeed the result of experimental manipulations, and not of an overlooked assumption that may have been violated. Therefore, I assessed the linearity of gradient-echo (GRE) BOLD-based fMRI signal amplitude measurements across

cortical depth in **Chapters 2 & 3** of this thesis, using the visual system as a testbed. I found that both assumptions for a linear system generally hold. In **Chapter 2**, I showed that the response amplitude across cortical depth resulting from one stimulus contrast, is an excellent predictor for the response amplitude across cortical depth for another stimulus contrast. I thus confirmed that, despite the directional blood draining across cortical depth and resulting dependencies, the scaling assumption for a linear system holds. In **Chapter 3**, I showed that at each cortical depth responses to shorter stimulus presentations, shifted in time and added together, are good predictors for responses to longer stimulus presentations. In summary, I have shown that the linearity assumptions that are required to perform traditional fMRI analyses, are generally met for laminar fMRI in the visual system.

Limitations

As with any other study, there are limitations to this linearity assessment. First of all, I have only carried out this assessment in a small part of the brain: the early and intermediate visual cortex (visual field maps V1, V2, and V3). While these are important and often-studied parts of the brain, they only cover a small portion of the cortex. We know from previous studies that BOLD responses differ between for instance visual and motor cortices (see e.g. Birn, Saad, & Bandettini, 2001). This may be exacerbated across cortical depth. Therefore, care should be taken when extrapolating the results from this thesis to regions of the brain that do not process visual information, although they may well still hold. Secondly, the acquisition method used for all experiments in this thesis is suboptimal for recording microvascular signals, as GRE echo planar imaging (EPI) is also sensitive to the macrovasculature (Huber et al., 2017). The latter is less layer-specific, resulting in a contamination of the more layer-specific signal from the microvasculature. Alternative acquisition sequences that are less sensitive to the macrovasculature, as discussed in the general introduction, are in my opinion likely to be the way forward for the field of laminar fMRI. However, as GRE-EPI remains the most widely available and consistently used acquisition method to this day, our linearity assessment is relevant for a substantial part of the current laminar fMRI field. Moreover, if any sequence is likely to be sensitive to nonlinearities in the fMRI signal across cortical depth, it is arguably GRE-EPI (as discussed at length in **Chapter 2**). Thus, as we find only limited nonlinearities using GRE-EPI, it is likely that other acquisition protocols suffer from even less nonlinear interactions. Lastly, I only used luminance contrast and presentation duration manipulation to assess the scaling and temporal additivity assumption respectively. While luminance contrast manipulations are often used for fundamental research and have been used extensively in regular-resolution fMRI linearity assessments, they are only a small part of a vast array of possible stimulus manipulations such as spatial frequency, color, orientation, density, etc. Linearity across cortical depth could be assessed for different stimulus properties, but this would require many scans, and would be very time-consuming. Moreover, an exhaustive study of all stimulus properties would be virtually impossible, as there are many. Instead, we decided to limit our efforts to contrast and presentation duration manipulation. The main motivation for this was that these were the stimulus properties that were varied in early linearity assessments for regular-resolution fMRI (see e.g. Boynton, Demb, Glover, & Heeger, 1999; Boynton et al., 1996; Friston et al., 1994).

Assessing higher-order cognitive processing across laminae: numerosity

Once I confirmed that the linearity assumptions hold for laminar fMRI analysis, we were ready to apply high-resolution imaging methods to neuroscientific questions. Most laminar fMRI studies have focused on early sensory processing (for reviews, see De Martino et al., 2018; Dumoulin, Fracasso, van der Zwaag, Siero, & Petridou, 2018; Lawrence, Formisano, Muckli, & de Lange, 2017; Petridou & Siero, 2017; Self & Roelfsema, 2017; Stephan et al., 2019; Yacoub, De Martino, & Ugurbil, 2018). However, relatively little is known about laminar processing for higher-order information. Thus, we set out to investigate exactly this. We used sub-millimeter fMRI to study laminar processing in numerosity-selective cortical regions. Numerosity perception refers to the set size of a group of items and is a higher-order process. Response curves for numerosity were estimated using a numerosity-tuning forward model previously developed in our group (Harvey, Klein, et al., 2013). For each neuronal population in the region of interest, I estimated the numerosity to which a population responded most (the preferred numerosity), and the numerosity range to which a population responded (the tuning width).

Assuming that laminar processing for numerosity information follows a similar pattern as this early visual cortex model, we would expect one of two patterns for tuning width across cortical depth: A U-shaped profile, or an inverted U-shaped profile. In early visual cortex, ascending information arrives in layer IV (central layer), and feedback information arrives in laminae above and below it (the supra- and infragranular layers; Felleman & Van Essen, 1991; Shipp, 2007). As information is processed more extensively with distance from layer IV, the (population) receptive field size profile across cortical depth is U-shaped (Fracasso, Petridou, et al., 2016; Hubel, 1988; Self et al., 2019). The rationale for the U-shaped profile for laminar processing of numerosity information would be identical to this: more extensive information processing results in increasing tuning widths with distance from layer IV. An inverted U-shape could be expected as, rather than generalizing the incoming information (as in early visual cortex), numerosity processing may sharpen the responses outwards from layer IV, as this processing should ultimately result in one specific output (e.g. perception of the set size '5'). However, there is no direct sensory innervation to the numerosity-selective cortex, i.e. there is no direct correspondence between the low-level visual properties of the numerosity stimuli (such as stimulus size, total surface area, shape, etc.) and the responses of numerosity-selective neuronal populations (Harvey, Klein, et al., 2013). Therefore, the tuning width profile across cortical depth may also differ from the above predictions.

Tuning width in numerosity-responsive cortex does not vary across cortical depth

In **Chapter 4**, I investigated the tuning width across cortical depth in a numerosity-responsive region of interest, NPC1 (Harvey, Klein, et al., 2013). I found that tuning width increases with increasing preferred numerosity for most cortical depth bins. This is consistent with previous results from fMRI studies at regular resolution (Harvey & Dumoulin, 2017; Harvey, Klein, et al., 2013). Contrary to the hypotheses, there were no consistent significant differences in tuning width across cortical depth. For this, it did not matter whether I took the average tuning width for each cortical depth bin, or extracted the tuning widths at a set numerosity from a linear fit for each cortical depth bin. Two potential explanations for this pattern across cortical depth come to mind. The first one is that the U or inverted U-shaped pattern was lost in the measurement noise, stemming from factors such as subject motion, scanner-related instabilities, and/or physiological noise from breathing and heartrate. However, general model fit quality was fine, albeit lower than for previous -non-laminar- fMRI studies. This is easily explained by the reduced signal-to-noise ratio (SNR) that comes with increasing spatial resolutions. To reduce the measurement noise, I could increase the SNR by adding additional scanning

sessions for the subjects, and potentially by exploring alternative/additional denoising strategies and voxel selection criteria. The second explanation for the absence of a(n inverted) U-shaped tuning width profile, is that laminar organization of maps involved in higher cognitive functions (in this case numerosity) may be constructed differently from maps innervated by our sensory organs. Population receptive field sizes in the visual system increase roughly five-fold between visual field maps across the visual processing hierarchy (Harvey & Dumoulin, 2011). However, previous comparisons across a network of numerosity-selective cortical maps showed only small differences in tuning width between different numerosity maps (Harvey & Dumoulin, 2017). Seeing that tuning width differences between cortical maps are mostly negligible, it is entirely plausible that the same holds for numerosity processing across cortical depth. Moreover, little is known about laminar information processing outside the primary sensory cortices. Assuming the same laminar information processing flow for the entire brain is an attractive hypothesis, but as I found in **Chapter 4**, this assumption may not hold.

Intracranial recordings reveal numerosity-tuned neuronal populations

While laminar fMRI has a great spatial resolution, the inherently sluggish temporal nature of the BOLD response prevents us from measuring neuronal responses at a great temporal resolution using fMRI (Gazzaniga et al., 2014). To investigate brain processes at a higher temporal resolution while simultaneously not losing too much spatial resolution, I needed to revert to invasive neuroimaging methods. In **Chapter 5**, I used electrocorticography (ECoG) to identify transient numerosity-tuned responses in humans. This imaging technique has a spatial resolution of 1-2 mm, and a temporal resolution in the millisecond range (Gazzaniga et al., 2014). Both subjects were patients who temporarily had electrode grids implanted directly on the cortical surface for clinical purposes. While these patients are relatively rare, it is even rarer that the coverage of the electrode grids includes the parietal cortex, where one of the most reliably identifiable numerosity map (in fMRI studies) is located (Harvey, Klein, et al., 2013). We presented numerosity stimuli that were very similar to the laminar fMRI study from the previous chapter. I identified a neuronal population that responds selectively to numerosity 7, with a decreasing response to numerosities that lie numerically further away from it. This response was limited to only the high-frequency band. The location of this neuronal population could be traced to roughly the location of NPC1 (as studied in **Chapter 4**); one of the numerosity maps located around the intraparietal sulcus. Furthermore, this neuronal population did not respond to category-specific (face, house, or letter) stimuli, further supporting its response specificity, and excluding the possibility that this population was generally active for any visual input (as would be expected for early visual electrodes). I further support the latter claim by showing that the response pattern of the numerosity-selective neuronal population is fundamentally different from that of neuronal populations in early/intermediate visual cortex. In summary, I identified a neuronal population that showed a numerosity-tuned response pattern in a similar location as in previous fMRI experiments (Harvey & Dumoulin, 2017; Harvey, Klein, et al., 2013).

Limitations

The identified numerosity-selective neuronal population underlies a single electrode in a single subject. As electrode grids covered the parietal lobe in only one subject, it is not surprising that I find a limited number of electrodes. However, a single electrode is very little to go on, even though the location corresponds to previous fMRI experiments, it appears to be selectively responsive to numerosity stimuli, and is tuned to a specific numerosity. The electrode grids in the second subject covered most of the occipital cortex, which provided a clear image of what low-level visual responses to the numerosity stimuli should look like. Nonetheless, the coverage for this subject was suboptimal for identification of numerosity-selective neuronal populations. Thus, it is desirable to increase the number of subjects for this study, even though parietal electrode coverage is rare. As the keen reader

may have spotted, I do not make full use of the advantages in temporal resolution that ECoG has to offer. So far, the main analysis was focused on the average response across a certain time window. I thus do not specifically investigate any high-resolution temporal patterns. This would be of interest as this is a major benefit of ECoG over fMRI.

Laminar fMRI for clinical applications

Laminar fMRI can not only be used to study higher-order visual processing, but also for studying clinical conditions. Thus far, researchers have been left guessing as to the explanation of certain findings in clinical populations, such as macular degeneration (MD). Patients suffering from MD have a defect in the macula (part of the retina where most cone-type photoreceptors are located) that results in a blurred or complete absence of vision in the center of the visual field. It has been argued that in patients with MD, feedback connections to early visual cortex representations of the macula have been spared, while feedforward connections to these areas are absent. This theory, however, is based on a regular resolution fMRI-study (Masuda et al., 2008). This study has shown that there is task-related activation in regions of the primary visual cortex that represent the macula, which should not be activated as they do not receive any visual input. It was hypothesized that this activation was the effect of spared feedback interactions to the macular representations in the primary visual cortex. With laminar fMRI, it is possible to investigate this hypothesis, thus expanding our knowledge of information processing in clinical populations. Of course, laminar fMRI can be applied to better understand ample other clinical conditions, such as retinitis pigmentosa, achiasma, amblyopia, and albinism. It is thus a promising tool to further our understanding of numerous conditions, both in the visual as well as in other domains.

Conclusion

All in all, I have investigated laminar processing of higher-order (visual) information in this thesis. The chosen methods for this were laminar fMRI and intracranial recordings. I first set out to investigate whether the linearity assumptions that underly most fMRI analyses, hold for laminar fMRI. I have shown that both linearity assumptions for laminar fMRI are met for recordings in the visual system. We can thus apply previously developed fMRI analyses to laminar fMRI data, without having to implement major corrections for BOLD nonlinearities. Next, I used this knowledge in my assessment of laminar processing of numerosity information. Using laminar fMRI, I showed that laminar information processing in numerosity-responsive parietal cortex is arranged differently from laminar information processing in the visual cortex. This observation was further supported using intracranial recordings, showing that the neuronal population response pattern in numerosity-responsive parietal cortex is distinct from response patterns in the visual cortex.

While fMRI has been around for a couple decades, laminar fMRI has only become feasible in humans less than a decade ago. It is a big step forward in the level of detail at which we can record the structure and function of the brain, as it for the first time allows for the non-invasive investigation of information processing across cortical depth. However, conducting laminar fMRI research remains challenging to this day as data acquisition, processing, analysis, and interpretation all require additional steps, precision, and considerations. Substantial progress has been made in the laminar fMRI field, slowly converging towards a set of common acquisition, processing, and analysis methods. A considerable amount of fundamental research is still being carried out in this field, with neuroscientific applications beginning to emerge slowly but steadily. At the end of the day, laminar fMRI is a relatively new, quickly developing, and very exciting field with promising applications for neuroscience across the board.

Appendix

References

- Anderson, J. C., & Martin, K. A. C. (2009). *The Synaptic Connections between Cortical Areas V1 and V2 in Macaque Monkey*. <https://doi.org/10.1523/JNEUROSCI.5757-08.2009>
- Andersson, J. L. R., Skare, S., & Ashburner, J. (2003). How to correct susceptibility distortions in spin-echo echo-planar images: Application to diffusion tensor imaging. *NeuroImage*, 20(2), 870–888. [https://doi.org/10.1016/S1053-8119\(03\)00336-7](https://doi.org/10.1016/S1053-8119(03)00336-7)
- Angelucci, A., Levitt, J. B., Walton, E. J. S., Hupe, J.-M., Bullier, J., & Lund, J. S. (2002). Circuits for local and global signal integration in primary visual cortex. *The Journal of Neuroscience : The Official Journal of the Society for Neuroscience*, 22(19), 8633–8646. <https://doi.org/10.1523/JNEUROSCI.22-19-08633.2002>
- Aquino, K. M., Robinson, P. A., Schira, M. M., & Breakspear, M. (2014). Deconvolution of neural dynamics from fMRI data using a spatiotemporal hemodynamic response function. *NeuroImage*, 94, 203–215. <https://doi.org/10.1016/j.neuroimage.2014.03.001>
- Aquino, K. M., Schira, M. M., Robinson, P. A., Drysdale, P. M., & Breakspear, M. (2012). Hemodynamic traveling waves in human visual cortex. *PLoS Computational Biology*, 8(3), e1002435. <https://doi.org/10.1371/journal.pcbi.1002435>
- Bazin, P.-L., Cuzzocreo, J. L., Yassa, M. A., Gandler, W., Mcauliffe, M. J., Bassett, S. S., & Pham, D. L. (2007). Volumetric neuroimage analysis extensions for the MIPAV software package. *Journal of Neuroscience Methods*, 165, 111–121. <https://doi.org/10.1016/j.jneumeth.2007.05.024>
- Bennett, C., Miller, M., & Wolford, G. (2009). Neural correlates of interspecies perspective taking in the post-mortem Atlantic Salmon: an argument for multiple comparisons correction. *NeuroImage*, 47, S125. [https://doi.org/10.1016/s1053-8119\(09\)71202-9](https://doi.org/10.1016/s1053-8119(09)71202-9)
- Birn, R. M., Saad, Z. S., & Bandettini, P. A. (2001). Spatial heterogeneity of the nonlinear dynamics in the fMRI BOLD response. *NeuroImage*, 14(4), 817–826. <https://doi.org/10.1006/nimg.2001.0873>
- Boas, D. A., Jones, S. R., Devor, A., Huppert, T. J., & Dale, A. M. (2008). A vascular anatomical network model of the spatio-temporal response to brain activation. *NeuroImage*, 40(3), 1116–1129. <https://doi.org/10.1016/j.neuroimage.2007.12.061>
- Boynton, G. M., Demb, J. B., Glover, G. H., & Heeger, D. J. (1999). Neuronal basis of contrast discrimination. *Vision Research*, 39(2), 257–269. [https://doi.org/10.1016/S0042-6989\(98\)00113-8](https://doi.org/10.1016/S0042-6989(98)00113-8)
- Boynton, G. M., Engel, S. A., Glover, G. H., & Heeger, D. J. (1996). Linear systems analysis of functional magnetic resonance imaging in human V1. *Journal of Neuroscience*, 16(13), 4207–21. Retrieved from http://www.ncbi.nlm.nih.gov/entrez/query.fcgi?cmd=Retrieve&db=PubMed&dopt=Citation&list_uids=8753882
- Boynton, G. M., Engel, S. A., & Heeger, D. J. (2012). Linear systems analysis of the fMRI signal. *NeuroImage*, 62(2), 975–984. <https://doi.org/10.1016/j.neuroimage.2012.01.082>
- Brainard, D. H. (1997). The Psychophysics Toolbox. *Spatial Vision*, 10(4), 433–436. <https://doi.org/10.1163/156856897X00357>
- Brannon, E. M., & Terrace, H. S. (1998). Ordering of the numerosities 1 to 9 by monkeys. *Science*, 282(5389), 746–749. <https://doi.org/10.1126/science.282.5389.746>
- Brodmann, K. (1903). Beiträge zur histologischen Lokalisation der Grosshirnrinde. II. Der Calcarinustyp. *Journal of Psychology and Neurology*, 2, 133–159.

- Brodmann, K. (1909). *Vergleichende Lokalisationslehre der Grosshirnrinde in ihren Prinzipien dargestellt auf Grund des Zellenbaues*. Leipzig: JA Barth.
- Burr, D., & Ross, J. (2008). A Visual Sense of Number. *Current Biology*, 18(6), 425–428. <https://doi.org/10.1016/j.cub.2008.02.052>
- Buxton, R. B., Wong, E. C., & Frank, L. R. (1998). Dynamics of blood flow and oxygenation changes during brain activation: The balloon model. *Magnetic Resonance in Medicine*, 39(6), 855–864. <https://doi.org/10.1002/mrm.1910390602>
- Cambridge Research Systems. (2012). BOLDscreen 32 LCD for fMRI. Retrieved from <http://www.crsi.com/tools-for-functional-imaging/mr-safe-displays/boldscreen-32-lcd-for-fmri/nest/boldscreen-32-technical-specification#npm>
- Cantlon, J. F., Libertus, M. E., Pinel, P., Dehaene, S., Brannon, E. M., & Pelphrey, K. A. (2009). The neural development of an abstract concept of number. *Journal of Cognitive Neuroscience*, 21(11), 2217–2229. <https://doi.org/10.1162/jocn.2008.21159>
- Chen, G., Wang, F., Gore, J. C., & Roe, A. W. (2012). Identification of cortical lamination in awake monkeys by high resolution magnetic resonance imaging. *NeuroImage*, 59(4), 3441–3449. <https://doi.org/10.1016/j.neuroimage.2011.10.079>
- Chen, Y., Namburi, P., Elliott, L. T., Heinzle, J., Soon, C. S., Chee, M. W. L., & Haynes, J. D. (2011). Cortical surface-based searchlight decoding. *NeuroImage*, 56(2), 582–592. <https://doi.org/10.1016/j.neuroimage.2010.07.035>
- Cheng, K., Waggoner, R. A., & Tanaka, K. (2001). Human ocular dominance columns as revealed by high-field functional magnetic resonance imaging. *Neuron*, 32(2), 359–374. [https://doi.org/10.1016/S0896-6273\(01\)00477-9](https://doi.org/10.1016/S0896-6273(01)00477-9)
- Clark, V. P., & Hillyard, S. A. (1996). Spatial selective attention affects early extrastriate but not striate components of the visual evoked potential. *Journal of Cognitive Neuroscience*, 8(5), 387–402. <https://doi.org/10.1162/jocn.1996.8.5.387>
- Cohen, M. S. (1997). Parametric Analysis of fMRI Data Using Linear Systems Methods. *NeuroImage*, 6(2), 93–103. <https://doi.org/10.1006/nimg.1997.0278>
- Cox, R. W. (1996). AFNI: Software for Analysis and Visualization of Functional Magnetic Resonance Neuroimages. *Computers and Biomedical Research* 29, 162–173.
- Daitch, A. L., Foster, B. L., Schrouff, J., Rangarajan, V., Kaşıkçı, I., Gattas, S., & Parvizi, J. (2016). Mapping human temporal and parietal neuronal population activity and functional coupling during mathematical cognition. *Proceedings of the National Academy of Sciences of the United States of America*, 113(46), E7277–E7286. <https://doi.org/10.1073/pnas.1608434113>
- De Martino, F., Moerel, M., Ugurbil, K., Goebel, R., Yacoub, E., & Formisano, E. (2015). Frequency preference and attention effects across cortical depths in the human primary auditory cortex. *Proceedings of the National Academy of Sciences*, 112(52), 16036–16041. <https://doi.org/10.1073/pnas.1507552112>
- De Martino, F., Yacoub, E., Kemper, V., Moerel, M., Uludag, K., De Weerd, P., ... Formisano, E. (2018). The impact of ultra-high field MRI on cognitive and computational neuroimaging. *NeuroImage*, 168, 366–382. <https://doi.org/10.1016/j.neuroimage.2017.03.060>
- De Martino, F., Zimmermann, J., Muckli, L., Ugurbil, K., Yacoub, E., & Goebel, R. (2013). Cortical Depth Dependent Functional Responses in Humans at 7T: Improved Specificity with 3D GRASE. *PLoS ONE*, 8(3), e60514. <https://doi.org/10.1371/journal.pone.0060514>

- Dehaene, S. (1997). *The number sense : how the mind creates mathematics*. Oxford University Press.
- Dehaene, S., & Changeux, J. P. (1993). Development of elementary numerical abilities: A neuronal model. *Journal of Cognitive Neuroscience*, 5(4), 390–407. <https://doi.org/10.1162/jocn.1993.5.4.390>
- Dehaene, S., Spelke, E., Pinel, P., Stanescu, R., & Tsivkin, S. (1999). Sources of mathematical thinking: Behavioral and brain-imaging evidence. *Science*, 284(5416), 970–974. <https://doi.org/10.1126/science.284.5416.970>
- Ditz, H. M., & Nieder, A. (2015). Neurons selective to the number of visual items in the corvid songbird endbrain. *Proceedings of the National Academy of Sciences of the United States of America*, 112(25), 7827–7832. <https://doi.org/10.1073/pnas.1504245112>
- Ditz, H. M., & Nieder, A. (2016a). Numerosity representations in crows obey the Weber-Fechner law. *Proceedings of the Royal Society B: Biological Sciences*, 283(1827). <https://doi.org/10.1098/rspb.2016.0083>
- Ditz, H. M., & Nieder, A. (2016b). Sensory and working memory representations of small and large numerosities in the crow endbrain. *Journal of Neuroscience*, 36(47), 12044–12052. <https://doi.org/10.1523/JNEUROSCI.1521-16.2016>
- Dumoulin, S. O. (2017). Layers of Neuroscience. *Neuron*, Vol. 96, pp. 1205–1206. <https://doi.org/10.1016/j.neuron.2017.12.004>
- Dumoulin, S. O., Fracasso, A., van der Zwaag, W., Siero, J. C. W., & Petridou, N. (2018). Ultra-high field MRI: Advancing systems neuroscience towards mesoscopic human brain function. *NeuroImage*, 168, 345–357. <https://doi.org/10.1016/j.neuroimage.2017.01.028>
- Dumoulin, S. O., & Wandell, B. A. (2008). Population receptive field estimates in human visual cortex. *NeuroImage*, 39(2), 647–660. <https://doi.org/10.1016/j.neuroimage.2007.09.034>
- Duvernoy, H. M., Delon, S., & Vannson, J. L. (1981). Cortical blood vessels of the human brain. *Brain Research Bulletin*, 7(5), 519–579. [https://doi.org/10.1016/0361-9230\(81\)90007-1](https://doi.org/10.1016/0361-9230(81)90007-1)
- Eger, E., Michel, V., Thirion, B., Amadon, A., Dehaene, S., & Kleinschmidt, A. (2009). Deciphering Cortical Number Coding from Human Brain Activity Patterns. *Current Biology*, 19(19), 1608–1615. <https://doi.org/10.1016/j.cub.2009.08.047>
- Fedorov, A., Beichel, R., Kalpathy-Cramer, J., Finet, J., Fillion-Robin, J. C., Pujol, S., ... Kikinis, R. (2012). 3D Slicer as an image computing platform for the Quantitative Imaging Network. *Magnetic Resonance Imaging*, 30(9), 1323–1341. <https://doi.org/10.1016/j.mri.2012.05.001>
- Feinberg, D. A., & Günther, M. (2009). Cerebral Blood Flow Imaging with 3D GRASE ASL Sequence Increases SNR and Shortens Acquisition Time. *MAGNETOM Flash*, 3(3), 62–69. Retrieved from www.siemens.com/magnetom-world
- Felleman, D. J., & Van Essen, D. C. (1991). Distributed hierarchical processing in the primate cerebral cortex. *Cerebral Cortex*, 1(1), 1–47. <https://doi.org/10.1093/cercor/1.1.1-a>
- Fischl, B., & Dale, A. M. (1999). Measuring the thickness of the human cerebral cortex. *NeuroImage*, 9(6 PART II). Retrieved from www.pnas.org
- Fracasso, A., Luijten, P. R., Dumoulin, S. O., & Petridou, N. (2017). Laminar imaging of positive and negative BOLD in human visual cortex at 7T. *NeuroImage*, (February), 1–12. <https://doi.org/10.1016/j.neuroimage.2017.02.038>

- Fracasso, A., Petridou, N., & Dumoulin, S. O. (2016). Systematic variation of population receptive field properties across cortical depth in human visual cortex. *NeuroImage*, 139, 427–438. <https://doi.org/10.1016/j.neuroimage.2016.06.048>
- Fracasso, A., Van Veluw, S. J., Visser, F., Luijten, P. R., Spliet, W., Zwanenburg, J. J. M. M., ... Petridou, N. (2016). Lines of Baillarger in vivo and ex vivo: Myelin contrast across lamina at 7 T MRI and histology. *NeuroImage*, 133, 163–175. <https://doi.org/10.1016/j.neuroimage.2016.02.072>
- Friston, K. J., Fletcher, P., Josephs, O., Holmes, A., Rugg, M. D., & Turner, R. (1998). Event-related fMRI: Characterizing differential responses. *NeuroImage*, 7(1), 30–40. <https://doi.org/10.1006/nimg.1997.0306>
- Friston, K. J., Jezzard, P., & Turner, R. (1994). The analysis of functional MRI time-series. *Human Brain Mapping*, 1, 153–171. Retrieved from
- Gazzaniga, M. S., Ivry, R. B., & Mangun, G. R. (2014). Methods of Cognitive Neuroscience. In *Cognitive Neuroscience* (4th ed., pp. 72–117). New York, London: W. W. Norton & Company, Inc.
- Gennari, F. (1782). *De Peculiari Structura Cerebri Parma Ex Regio Typographeo*.
- Geyer, S., & Turner, R. (2013). Microstructural parcellation of the human cerebral cortex: From Brodmann's post-mortem map to in vivo mapping with high-field magnetic resonance imaging. In *Microstructural Parcellation of the Human Cerebral Cortex: From Brodmann's Post-Mortem Map to in Vivo Mapping with High-Field Magnetic Resonance Imaging* (Vol. 5). <https://doi.org/10.1007/978-3-642-37824>
- Gilbert, C. D. (2000). The Constructive Nature of Visual Processing. In E. R. Kandel, J. H. Schwartz, T. M. Jessell, S. A. Spiegelbaum, & A. J. Hudspeth (Eds.), *Principles of Neural Science* (5th ed., pp. 556–576). New York: McGraw-Hill Professional.
- Goense, J. B. M., & Logothetis, N. K. (2006). Laminar specificity in monkey V1 using high-resolution SE-fMRI. *Magnetic Resonance Imaging*, 24(4), 381–392. <https://doi.org/10.1016/j.mri.2005.12.032>
- Goense, J. B. M., Merkle, H., & Logothetis, N. K. (2012). High-Resolution fMRI Reveals Laminar Differences in Neurovascular Coupling between Positive and Negative BOLD Responses. *Neuron*, 76(3), 629–639. <https://doi.org/10.1016/j.neuron.2012.09.019>
- Goense, J. B. M., Zappe, A. C., & Logothetis, N. K. (2007). High-resolution fMRI of macaque V1. *Magnetic Resonance Imaging*, 25(6), 740–747. <https://doi.org/10.1016/j.mri.2007.02.013>
- Goodyear, B. G., & Menon, R. S. (2001). Brief visual stimulation allows mapping of ocular dominance in visual cortex using fMRI. *Human Brain Mapping*, 14(4), 210–217. <https://doi.org/10.1002/hbm.1053>
- Graham, J., Lin, C. -S, & Kaas, J. H. (1979). Subcortical projections of six visual cortical areas in the owl monkey, *Aotus trivirgatus*. *Journal of Comparative Neurology*, 187(3), 557–580. <https://doi.org/10.1002/cne.901870307>
- Gray, H. (1995). *Gray's anatomy : the anatomical basis of medicine and surgery*. (38th ed.; P. L. Williams & L. H. Bannister, Eds.). New York: Churchill Livingstone.
- Halberda, J., Mazocco, M. M. M., & Feigenson, L. (2008). Individual differences in non-verbal number acuity correlate with maths achievement. *Nature*, 455(7213), 665–668. <https://doi.org/10.1038/nature07246>

- Harel, N., Lin, J., Moeller, S., Ugurbil, K., & Yacoub, E. (2006). Combined imaging-histological study of cortical laminar specificity of fMRI signals. *NeuroImage*, 29(3), 879–887. <https://doi.org/10.1016/j.neuroimage.2005.08.016>
- Harvey, B. M. (2016). Quantity cognition: Numbers, numerosity, zero and mathematics. *Current Biology*, Vol. 26, pp. R419–R421. <https://doi.org/10.1016/j.cub.2016.03.059>
- Harvey, B. M., & Dumoulin, S. O. (2011). The Relationship between Cortical Magnification Factor and Population Receptive Field Size in Human Visual Cortex: Constancies in Cortical Architecture. *Journal of Neuroscience*, 31(38), 13604–13612. <https://doi.org/10.1523/JNEUROSCI.2572-11.2011>
- Harvey, B. M., & Dumoulin, S. O. (2017). A network of topographic numerosity maps in human association cortex. *Nature Human Behaviour*, 1(2), 0036. <https://doi.org/10.1038/s41562-016-0036>
- Harvey, B. M., Klein, B. P., Petridou, N., & Dumoulin, S. O. (2013). Topographic Representation of Numerosity in the Human Parietal Cortex. *Science*, 341(6150), 1123–1126. <https://doi.org/10.1126/science.1239052>
- Harvey, B. M., Vansteensel, M. J., Ferrier, C. H., Petridou, N., Zuiderbaan, W., Aarnoutse, E. J., ... Dumoulin, S. O. (2013). Frequency specific spatial interactions in human electrocorticography: V1 alpha oscillations reflect surround suppression. *NeuroImage*, 65, 424–432. <https://doi.org/10.1016/j.neuroimage.2012.10.020>
- Hauser, M. D., Carey, S., & Hauser, L. B. (2000). Spontaneous number representation in semi-free-ranging rhesus monkeys. *Proceedings of the Royal Society B: Biological Sciences*, 267(1445), 829–833. <https://doi.org/10.1098/rspb.2000.1078>
- Hauser, M. D., Tsao, F., Garcia, P., & Spelke, E. S. (2003). Evolutionary foundations of number: Spontaneous representation of numerical magnitudes by cotton-top tamarins. *Proceedings of the Royal Society B: Biological Sciences*, 270(1523), 1441–1446. <https://doi.org/10.1098/rspb.2003.2414>
- Havlicek, M., & Uludag, K. (2019). A dynamical model of the laminar BOLD response. *BioRxiv*, 1–39. <https://doi.org/10.1101/609099>
- Heeger, D. J., Huk, A. C., Geisler, W. S., & Albrecht, D. G. (2000). Spikes versus BOLD: What does neuroimaging tell us about neuronal activity? *Nature Neuroscience*, 3(7), 631–633. <https://doi.org/10.1038/76572>
- Heinzle, J., Koopmans, P. J., den Ouden, H. E. M., Raman, S., & Stephan, K. E. (2016). A hemodynamic model for layered BOLD signals. *NeuroImage*, 125, 556–570. <https://doi.org/10.1016/j.neuroimage.2015.10.025>
- Herman, P., Sanganahalli, B. G., Blumenfeld, H., Rothman, D. L., & Hyder, F. (2013). Quantitative basis for neuroimaging of cortical laminae with calibrated functional MRI. *Proceedings of the National Academy of Sciences*, 110(37), 15115–15120. <https://doi.org/10.1073/pnas.1307154110>
- Hermes, D., Miller, K. J., Noordmans, H. J., Vansteensel, M. J., & Ramsey, N. F. (2010). Automated electrocorticographic electrode localization on individually rendered brain surfaces. *Journal of Neuroscience Methods*, 185(2), 293–298. <https://doi.org/10.1016/j.jneumeth.2009.10.005>
- Hermes, D., Miller, K. J., Vansteensel, M. J., Aarnoutse, E. J., Leijten, F. S. S., & Ramsey, N. F. (2012). Neurophysiologic correlates of fMRI in human motor cortex. *Human Brain Mapping*, 33(7), 1689–1699. <https://doi.org/10.1002/hbm.21314>

- Hubel, D. H. (1988). Eye, Brain, and Vision. In *New York*.
- Hubel, D. H., & Wiesel, T. N. (1962). Receptive fields, binocular interaction and functional architecture in the cat's visual cortex. *The Journal of Physiology*, 160(1), 106–154. <https://doi.org/10.1113/jphysiol.1962.sp006837>
- Hubel, D. H., & Wiesel, T. N. (1972). Laminar and columnar distribution of geniculo-cortical fibers in the macaque monkey. *Journal of Comparative Neurology*, 146(4), 421–450. <https://doi.org/10.1002/cne.901460402>
- Hubel, D. H., & Wiesel, T. N. (1974). Uniformity of monkey striate cortex: A parallel relationship between field size, scatter, and magnification factor. *Journal of Comparative Neurology*, 158(3), 295–305. <https://doi.org/10.1002/cne.901580305>
- Huber, L., Goense, J. B. M., Kennerley, A. J., Ivanov, D., Krieger, S. N., Lepsien, J., ... Möller, H. E. (2014). Investigation of the neurovascular coupling in positive and negative BOLD responses in human brain at 7T. *NeuroImage*, 97, 349–362. <https://doi.org/10.1016/j.neuroimage.2014.04.022>
- Huber, L., Goense, J. B. M., Kennerley, A. J., Trampel, R., Guidi, M., Reimer, E., ... Möller, H. E. (2015). Cortical lamina-dependent blood volume changes in human brain at 7T. *NeuroImage*, 107, 23–33. <https://doi.org/10.1016/j.neuroimage.2014.11.046>
- Huber, L., Handwerker, D. A., Jangraw, D. C., Chen, G., Hall, A., Stüber, C., ... Bandettini, P. A. (2017). High-Resolution CBV-fMRI Allows Mapping of Laminar Activity and Connectivity of Cortical Input and Output in Human M1. *Neuron*, 96(6), 1253-1263.e7. <https://doi.org/10.1016/j.neuron.2017.11.005>
- Huber, L., Ivanov, D., Krieger, S. N., Streicher, M. N., Mildner, T., Poser, B. A., ... Turner, R. (2014). Slab-selective, BOLD-corrected VASO at 7 Tesla provides measures of cerebral blood volume reactivity with high signal-to-noise ratio. *Magnetic Resonance in Medicine*, 72(1), 137–148. <https://doi.org/10.1002/mrm.24916>
- Jin, T., & Kim, S. G. (2008). Cortical layer-dependent dynamic blood oxygenation, cerebral blood flow and cerebral blood volume responses during visual stimulation. *NeuroImage*, 43(1), 1–9. <https://doi.org/10.1016/j.neuroimage.2008.06.029>
- Kashyap, S., Ivanov, D., Havlicek, M., Poser, B. A., & Uludağ, K. (2017). Impact of acquisition and analysis strategies on cortical depth-dependent fMRI. *NeuroImage*. <https://doi.org/10.1016/j.neuroimage.2017.05.022>
- Kay, K. N., Winawer, J., Mezer, A., & Wandell, B. A. (2013). Compressive spatial summation in human visual cortex. *Journal of Neurophysiology*, 110(2), 481–494. <https://doi.org/10.1152/jn.00105.2013>
- Kemper, V. G., De Martino, F., Vu, A. T., Poser, B. A., Feinberg, D. A., Goebel, R., & Yacoub, E. (2015). Sub-millimeter T2-weighted fMRI at 7 T: Comparison of 3D-GRASE and 2D SE-EPI. *Frontiers in Neuroscience*, 9(APR), 1–14. <https://doi.org/10.3389/fnins.2015.00163>
- Kershaw, J., Kashikura, K., Zhang, X., Abe, S., & Kanno, I. (2001). Bayesian technique for investigating linearity in event-related BOLD fMRI. *Magnetic Resonance in Medicine*, 45(6), 1081–1094. <https://doi.org/10.1002/mrm.1143>
- Kim, J. H., & Ress, D. (2017). Reliability of the depth-dependent high-resolution BOLD hemodynamic response in human visual cortex and vicinity. *Magnetic Resonance Imaging*, 39, 53–63. <https://doi.org/10.1016/j.mri.2017.01.019>

- Kim, S. G., & Ogawa, S. (2012). Biophysical and physiological origins of blood oxygenation level-dependent fMRI signals. *Journal of Cerebral Blood Flow and Metabolism*, Vol. 32, pp. 1188–1206. <https://doi.org/10.1038/jcbfm.2012.23>
- Klein, B. P., Fracasso, A., Dijk, J. A. van, Paffen, C. L. E., Pas, S. F., & Dumoulin, S. O. (2018). Cortical depth dependent population receptive field attraction by spatial attention in human V1. *NeuroImage*. <https://doi.org/10.1016/j.neuroimage.2018.04.055>
- Klein, B. P., Fracasso, A., van Dijk, J. A., Paffen, C. L. E., te Pas, S. F., & Dumoulin, S. O. (2018). Cortical depth dependent population receptive field attraction by spatial attention in human V1. *NeuroImage*, 176, 301–312. <https://doi.org/10.1016/j.neuroimage.2018.04.055>
- Knops, A., Piazza, M., Sengupta, R., Eger, E., & Melcher, D. (2014). A shared, flexible neural map architecture reflects capacity limits in both visual short-term memory and enumeration. *Journal of Neuroscience*, 34(30), 9857–9866. <https://doi.org/10.1523/JNEUROSCI.2758-13.2014>
- Kok, P., Bains, L. J., Van Mourik, T., Norris, D. G., & De Lange, F. P. (2016). Selective activation of the deep layers of the human primary visual cortex by top-down feedback. *Current Biology*, 26(3), 371–376. <https://doi.org/10.1016/j.cub.2015.12.038>
- Koopmans, P. J., Barth, M., & Norris, D. G. (2010). Layer-specific BOLD activation in human V1. *Human Brain Mapping*, 31(9), 1297–1304. <https://doi.org/10.1002/hbm.20936>
- Koopmans, P. J., Barth, M., Orzada, S., & Norris, D. G. (2011). Multi-echo fMRI of the cortical laminae in humans at 7T. *NeuroImage*, 56(3), 1276–1285. <https://doi.org/10.1016/j.neuroimage.2011.02.042>
- Koopmans, P. J., Boyacıoğlu, R., Barth, M., & Norris, D. G. (2012). Whole brain, high resolution spin-echo resting state fMRI using PINS multiplexing at 7T. *NeuroImage*, 62(3), 1939–1946. <https://doi.org/10.1016/j.neuroimage.2012.05.080>
- Kutter, E. F., Bostroem, J., Elger, C. E., Mormann, F., & Nieder, A. (2018). Single Neurons in the Human Brain Encode Numbers. *Neuron*, 100(3), 753–761.e4. <https://doi.org/10.1016/j.neuron.2018.08.036>
- Lachaux, J. P., Rudrauf, D., & Kahane, P. (2003). Intracranial EEG and human brain mapping. *Journal of Physiology Paris*, 97(4–6), 613–628. <https://doi.org/10.1016/j.jphysparis.2004.01.018>
- Lawrence, S. J. D., Formisano, E., Muckli, L., & de Lange, F. P. (2017). Laminar fMRI: Applications for cognitive neuroscience. *NeuroImage*. <https://doi.org/10.1016/j.neuroimage.2017.07.004>
- Lee, S. A., Spencer, D. D., & Spencer, S. S. (2000). Intracranial EEG seizure-onset patterns in neocortical epilepsy. *Epilepsia*, 41(3), 297–307. <https://doi.org/10.1111/j.1528-1157.2000.tb00159.x>
- Logothetis, N. K. (2002). The neural basis of the blood-oxygen-level-dependent functional magnetic resonance imaging signal. *Phil. Trans. R. Soc. Lond. B*, (357), 1003–1037. <https://doi.org/10.1098/rstb.2002.1114>
- Lu, H., Patel, S., Luo, F., Li, S. J., Hillard, C. J., Ward, B. D., & Hyde, J. S. (2004). Spatial correlations of laminar BOLD and CBV responses to rat whisker stimulation with neuronal activity localized by Fos expression. *Magnetic Resonance in Medicine*, 52(5), 1060–1068. <https://doi.org/10.1002/mrm.20265>
- Manning, J. R., Jacobs, J., Fried, I., & Kahana, M. J. (2009). Broadband shifts in local field potential power spectra are correlated with single-neuron spiking in humans. *Journal of Neuroscience*, 29(43), 13613–13620. <https://doi.org/10.1523/JNEUROSCI.2041-09.2009>

- Markov, N. T., & Kennedy, H. (2013, April). The importance of being hierarchical. *Current Opinion in Neurobiology*, Vol. 23, pp. 187–194. <https://doi.org/10.1016/j.conb.2012.12.008>
- Markuerkiaga, I., Barth, M., & Norris, D. G. (2016). A cortical vascular model for examining the specificity of the laminar BOLD signal. *NeuroImage*, 132, 491–498. <https://doi.org/10.1016/j.neuroimage.2016.02.073>
- Marquardt, I., Schneider, M., Gulban, O. F., Ivanov, D., & Uludağ, K. (2018). Cortical depth profiles of luminance contrast responses in human V1 and V2 using 7 T fMRI. *Human Brain Mapping*. <https://doi.org/10.1002/hbm.24042>
- Marques, J. P., Kober, T., Krueger, G., van der Zwaag, W., Van de Moortele, P. F., & Gruetter, R. (2010). MP2RAGE, a self bias-field corrected sequence for improved segmentation and T1-mapping at high field. *NeuroImage*, 49(2), 1271–1281. <https://doi.org/10.1016/j.neuroimage.2009.10.002>
- Masuda, Y., Dumoulin, S. O., Nakadomari, S., & Wandell, B. A. (2008). V1 projection zone signals in human macular degeneration depend on task, not stimulus. *Cerebral Cortex*, 18(11), 2483–2493. <https://doi.org/10.1093/cercor/bhm256>
- Masuda, Y., Horiguchi, H., Dumoulin, S. O., Furuta, A., Miyauchi, S., Nakadomari, S., & Wandell, B. A. (2010). Task-dependent V1 responses in human retinitis pigmentosa. *Investigative Ophthalmology and Visual Science*, 51(10), 5356–5364. <https://doi.org/10.1167/iovs.09-4775>
- Miezin, F. M., Maccotta, L., Ollinger, J. M., Petersen, S. E., & Buckner, R. L. (2000). Characterizing the hemodynamic response: Effects of presentation rate, sampling procedure, and the possibility of ordering brain activity based on relative timing. *NeuroImage*, 11(6 I), 735–759. <https://doi.org/10.1006/nimg.2000.0568>
- Miller, K. J., Sorensen, L. B., Ojemann, J. G., & Den Nijs, M. (2009). Power-law scaling in the brain surface electric potential. *PLoS Computational Biology*, 5(12). <https://doi.org/10.1371/journal.pcbi.1000609>
- Miller, K. J., Zanos, S., Fetz, E. E., Den Nijs, M., & Ojemann, J. G. (2009). Decoupling the cortical power spectrum reveals real-time representation of individual finger movements in humans. *Journal of Neuroscience*, 29(10), 3132–3137. <https://doi.org/10.1523/JNEUROSCI.5506-08.2009>
- Moran, J., & Desimone, R. (1985). Selective attention gates visual processing in the extrastriate cortex. *Science*, 229(4715), 782–784. <https://doi.org/10.1126/science.4023713>
- Muckli, L., De Martino, F., Vizioli, L., Petro, L. S., Smith, F. W., Ugurbil, K., ... Yacoub, E. (2015). Contextual Feedback to Superficial Layers of V1. *Current Biology*, 25(20), 2690–2695. <https://doi.org/10.1016/j.cub.2015.08.057>
- Nieder, A. (2018). Evolution of cognitive and neural solutions enabling numerosity judgements: Lessons from primates and corvids. *Philosophical Transactions of the Royal Society B: Biological Sciences*, Vol. 373. <https://doi.org/10.1098/rstb.2016.0514>
- Nieder, A., Freedman, D. J., & Miller, E. K. (2002). Representation of the quantity of visual items in the primate prefrontal cortex. *Science*, 297(5587), 1708–1711. <https://doi.org/10.1126/science.1072493>
- Nieder, A., & Miller, E. K. (2003). Coding of cognitive magnitude: Compressed scaling of numerical information in the primate prefrontal cortex. *Neuron*, 37(1), 149–157. [https://doi.org/10.1016/S0896-6273\(02\)01144-3](https://doi.org/10.1016/S0896-6273(02)01144-3)

- Nieder, A., & Miller, E. K. (2004). A parieto-frontal network for visual numerical information in the monkey. *Proceedings of the National Academy of Sciences of the United States of America*, 101(19), 7457–7462. <https://doi.org/10.1073/pnas.0402239101>
- Nieuwenhuys, R. (2013). The myeloarchitectonic studies on the human cerebral cortex of the Vogt-Vogt school, and their significance for the interpretation of functional neuroimaging data. In *Microstructural Parcellation of the Human Cerebral Cortex: From Brodmann's Post-Mortem Map to in Vivo Mapping with High-Field Magnetic Resonance Imaging* (Vol. 218, pp. 55–125). https://doi.org/10.1007/978-3-642-37824-9_3
- Nieuwenhuys, R., Broere, C. A. J., & Cerliani, L. (2015). A new myeloarchitectonic map of the human neocortex based on data from the Vogt–Vogt school. *Brain Structure and Function*, 220(5), 2551–2573. <https://doi.org/10.1007/s00429-014-0806-9>
- O'craven, K. M., Rosen, B. R., Kwong, K. K., Treisman, A., & Savoy, R. L. (1997). Voluntary Attention Modulates fMRI Activity in Human MT-MST responsible for processing simple visual motion information. If the visual stimulus remains unchanged, can. In *Neuron* (Vol. 18).
- Ogawa, S., Menon, R. S., Tank, D. W., Kim, S. G., Merkle, H., Ellermann, J. M., & Ugurbil, K. (1993). Functional brain mapping by blood oxygenation level-dependent contrast magnetic resonance imaging. *Biophysical Journal*, 64(3), 803–812. <https://doi.org/10.1182/blood-2006-11-055921>
- Olman, C. A., Harel, N., Feinberg, D. A., He, S., Zhang, P., Ugurbil, K., & Yacoub, E. (2012). Layer-specific fMRI reflects different neuronal computations at different depths in human V1. *PLoS ONE*, 7(3). <https://doi.org/10.1371/journal.pone.0032536>
- Oostenveld, R., Fries, P., Maris, E., & Schoffelen, J. M. (2011). FieldTrip: Open source software for advanced analysis of MEG, EEG, and invasive electrophysiological data. *Computational Intelligence and Neuroscience*, 2011. <https://doi.org/10.1155/2011/156869>
- Pelli, D. G. (1997). the Videotoolbox Software for Visual Psychophysics: Transforming Numbers Into Movies. *Spatial Vision*, 10(4), 437–442.
- Petridou, N., Italiaander, M., van de Bank, B. L., Siero, J. C. W., Luijten, P. R., & Klomp, D. W. J. (2013). Pushing the limits of high-resolution functional MRI using a simple high-density multi-element coil design. *NMR in Biomedicine*, 26(1), 65–73. <https://doi.org/10.1002/nbm.2820>
- Petridou, Natalia, & Siero, J. C. W. (2017). Laminar fMRI: What can the time domain tell us? *NeuroImage*. <https://doi.org/10.1016/j.neuroimage.2017.07.040>
- Pfeuffer, J., McCullough, J. C., Van De Moortele, P. F., Ugurbil, K., & Hu, X. (2003). Spatial dependence of the nonlinear BOLD response at short stimulus duration. *NeuroImage*, 18(4), 990–1000. [https://doi.org/10.1016/S1053-8119\(03\)00035-1](https://doi.org/10.1016/S1053-8119(03)00035-1)
- Piazza, M. (2011). Neurocognitive Start-Up Tools for Symbolic Number Representations. In *Space, Time and Number in the Brain* (pp. 267–285). <https://doi.org/10.1016/B978-0-12-385948-8.00017-7>
- Piazza, M., Izard, V., Pinel, P., Le Bihan, D., & Dehaene, S. (2004). Tuning curves for approximate numerosity in the human intraparietal sulcus. *Neuron*, 44(3), 547–555. <https://doi.org/10.1016/j.neuron.2004.10.014>
- Pinel, P., Clec, L., H.g, Moortele, V. De, P.f, Naccache, L., ... Stanislas. (1999). Event-related fMRI analysis of the cerebral circuit for number comparison. *NeuroReport*, 10(7), 1473–1479.

- Pisa, P. E., & Agrillo, C. (2009). Quantity discrimination in felines: A preliminary investigation of the domestic cat (*Felis silvestris catus*). *Journal of Ethology*, 27(2), 289–293. <https://doi.org/10.1007/s10164-008-0121-0>
- Polimeni, J. R., Fischl, B., Greve, D. N., & Wald, L. L. (2010). Laminar analysis of 7T BOLD using an imposed spatial activation pattern in human V1. *NeuroImage*, 52(4), 1334–1346. <https://doi.org/10.1016/j.neuroimage.2010.05.005>
- Potrich, D., Sovrano, V. A., Stancher, G., & Vallortigara, G. (2015). Quantity discrimination by zebrafish (*Danio rerio*). *Journal of Comparative Psychology*, 129(4), 388–393. <https://doi.org/10.1037/com0000012>
- Puckett, A. M., Aquino, K. M., Robinson, P. A., Breakspear, M., & Schira, M. M. (2016). The spatiotemporal hemodynamic response function for depth-dependent functional imaging of human cortex. *NeuroImage*, 139, 240–248. <https://doi.org/10.1016/j.neuroimage.2016.06.019>
- Reichold, J., Stampanoni, M., Lena Keller, A., Buck, A., Jenny, P., & Weber, B. (2009). Vascular graph model to simulate the cerebral blood flow in realistic vascular networks. *Journal of Cerebral Blood Flow and Metabolism*, 29(8), 1429–1443. <https://doi.org/10.1038/jcbfm.2009.58>
- Ress, D., Glover, G. H., Liu, J., & Wandell, B. (2007). Laminar profiles of functional activity in the human brain. *NeuroImage*, 34(1), 74–84. <https://doi.org/10.1016/j.neuroimage.2006.08.020>
- Robson, M. D., Dorosz, J. L., & Gore, J. C. (1998). Measurements of the temporal fMRI response of the human auditory cortex to trains of tones. *Neuroimage*, 7(3), 185–198.
- Rockland, K. S., & Pandya, D. N. (1979). Laminar origins and terminations of cortical connections of the occipital lobe in the rhesus monkey. *Brain Research*, 179(1), 3–20. [https://doi.org/10.1016/0006-8993\(79\)90485-2](https://doi.org/10.1016/0006-8993(79)90485-2)
- Saad, Z. S., Glen, D. R., Chen, G., Beauchamp, M. S., Desai, R., & Cox, R. W. (2010). Alignment using Local Pearson Correlation. *Ratio*, 44(3), 839–848. <https://doi.org/10.1016/j.neuroimage.2008.09.037.A>
- Sawamura, H., Shima, K., & Tanji, J. (2002). Numerical representation for action in the parietal cortex of the monkey. *Nature*, 415(6874), 918–922. <https://doi.org/10.1038/415918a>
- Schwartz, S., Vuilleumier, P., Hutton, C., Maravita, A., Dolan, R. J., & Driver, J. (2005). Attentional load and sensory competition in human vision: Modulation of fMRI responses by load at fixation during task-irrelevant stimulation in the peripheral visual field. *Cerebral Cortex*, 15(6), 770–786. <https://doi.org/10.1093/cercor/bhh178>
- Self, M. W., & Roelfsema, P. R. (2017). Paying Attention to the Cortical Layers. *Neuron*, 93(1), 9–11. <https://doi.org/10.1016/j.neuron.2016.12.032>
- Self, M. W., van Kerkoerle, T., Goebel, R., & Roelfsema, P. R. (2019). Benchmarking laminar fMRI: Neuronal spiking and synaptic activity during top-down and bottom-up processing in the different layers of cortex. *NeuroImage*, pp. 806–817. <https://doi.org/10.1016/j.neuroimage.2017.06.045>
- Shipp, S. (2007). Structure and function of the cerebral cortex. *Current Biology*, Vol. 17, pp. R443–R449. <https://doi.org/10.1016/j.cub.2007.03.044>
- Siero, J. C. W., Hendrikse, J., Hoogduin, H., Petridou, N., Luijten, P., & Donahue, M. J. (2015). Cortical depth dependence of the BOLD initial dip and poststimulus undershoot in human visual cortex at 7 Tesla. *Magnetic Resonance in Medicine*, 73(6), 2283–2295. <https://doi.org/10.1002/mrm.25349>

- Siero, J. C. W., Petridou, N., Hoogduin, H., Luijten, P. R., & Ramsey, N. F. (2011). Cortical depth-dependent temporal dynamics of the BOLD response in the human brain. *Journal of Cerebral Blood Flow and Metabolism*, 31(10), 1999–2008. <https://doi.org/10.1038/jcbfm.2011.57>
- Silva, A. C., & Koretsky, A. P. (2002). Laminar specificity of functional MRI onset times during somatosensory stimulation in rat. *Proceedings of the National Academy of Sciences*, 99(23), 15182–15187. <https://doi.org/10.1073/pnas.222561899>
- Sincich, L. C., & Horton, J. C. (2005). The Circuitry of V1 and V2: Integration of Color, Form, and Motion. *Annual Review of Neuroscience*, 28(1), 303–326. <https://doi.org/10.1146/annurev.neuro.28.061604.135731>
- Smirnakis, S. M., Schmid, M. C., Weber, B., Tolias, A. S., Augath, M., & Logothetis, N. K. (2007). Spatial specificity of BOLD versus cerebral blood volume fMRI for mapping cortical organization. *Journal of Cerebral Blood Flow and Metabolism*, 27(6), 1248–1261. <https://doi.org/10.1038/sj.jcbfm.9600434>
- Smith, F. W., & Muckli, L. (2010). Nonstimulated early visual areas carry information about surrounding context. *Proceedings of the National Academy of Sciences*, 107(46), 20099–20103. <https://doi.org/10.1073/pnas.1000233107>
- Soltysik, D. A., Peck, K. K., White, K. D., Crosson, B., & Briggs, R. W. (2004). Comparison of hemodynamic response nonlinearity across primary cortical areas. *NeuroImage*, 22(3), 1117–1127. <https://doi.org/10.1016/j.neuroimage.2004.03.024>
- Somers, D. C., Dale, A. M., Seiffert, A. E., & Tootell, R. B. H. (1999). Functional MRI reveals spatially specific attentional modulation in human primary visual cortex. *Proceedings of the National Academy of Sciences*, 96(4), 1663–1668. <https://doi.org/10.1073/pnas.96.4.1663>
- Stephan, K. E., Petzschner, F. H., Kasper, L., Bayer, J., Wellstein, K. V., Stefanics, G., ... Heinzle, J. (2019). Laminar fMRI and computational theories of brain function. *NeuroImage*, Vol. 197, pp. 699–706. <https://doi.org/10.1016/j.neuroimage.2017.11.001>
- Stephan, Klaas Enno, Weiskopf, N., Drysdale, P. M., Robinson, P. A., & Friston, K. J. (2007). Comparing hemodynamic models with DCM. *NeuroImage*, 38(3), 387–401. <https://doi.org/10.1016/j.neuroimage.2007.07.040>
- Tokita, M., & Ishiguchi, A. (2010). How might the discrepancy in the effects of perceptual variables on numerosity judgment be reconciled? *Attention, Perception, and Psychophysics*, 72(7), 1839–1853. <https://doi.org/10.3758/APP.72.7.1839>
- Turner, R. (2002). How much cortex can a vein drain? Downstream dilution of activation-related cerebral blood oxygenation changes. *NeuroImage*, 16(4), 1062–1067. <https://doi.org/10.1006/nimg.2002.1082>
- Uludağ, K., & Blinder, P. (2018). Linking brain vascular physiology to hemodynamic response in ultra-high field MRI. *NeuroImage*, 168, 279–295. <https://doi.org/10.1016/j.neuroimage.2017.02.063>
- van den Berg, C., Klomp, D., & Petridou, N. (2016). Ultra-high field MRI: what is in full bloom and what is sprouting? *NMR in Biomedicine*, 29(9), 1120–1121. <https://doi.org/10.1002/nbm.3595>
- Van Essen, D. C. (2003). Organization of Visual Areas in Macaque and Human Cerebral Cortex. In L. Chalupa & J. Werner (Eds.), *The Visual Neurosciences* (pp. 507–521). Cambridge, MA: MIT Press.
- Vazquez, A. L., & Noll, D. C. (1998). Nonlinear Aspects of the BOLD Response in Functional MRI. *NeuroImage*, 7, 108–118.

- Vogt, C., & Vogt, O. (1919). Ergebnisse unserer hirnforschung. 1.-4. Mitteilung. *J. Psychol. Neurol*, 25, 279–461.
- Vogt, O. (1910). Die myeloarchitektonische Felderung des menschlichen Stirnhirns. *Journal of Psychology and Neurology*, 15, 221–232.
- Waehnert, M. D., Dinse, J., Weiss, M., Streicher, M. N., Waehnert, P., Geyer, S., ... Bazin, P. L. (2014). Anatomically motivated modeling of cortical laminae. *NeuroImage*, 93, 210–220. <https://doi.org/10.1016/j.neuroimage.2013.03.078>
- Wandell, B. A., Winawer, J., & Kay, K. N. (2015). Computational Modeling of Responses in Human Visual Cortex. In *Brain Mapping: An Encyclopedic Reference* (Vol. 1, pp. 651–659). <https://doi.org/10.1016/B978-0-12-397025-1.00347-X>
- Wong-Riley, M. (1979). Columnar cortico-cortical interconnections within the visual system of the squirrel and macaque monkeys. *Brain Research*, 162(2), 201–217. [https://doi.org/10.1016/0006-8993\(79\)90284-1](https://doi.org/10.1016/0006-8993(79)90284-1)
- Xing, D., Yeh, C.-I., Burns, S., & Shapley, R. M. (2012). Laminar analysis of visually evoked activity in the primary visual cortex. *Proceedings of the National Academy of Sciences*, 109(34), 13871–13876. <https://doi.org/10.1073/pnas.1201478109>
- Yacoub, E., De Martino, F., & Ugurbil, K. (2018). The Use of Ultrahigh Field Functional MRI in Neuroscience Applications. In *Engineering in Medicine* (pp. 419–435). <https://doi.org/10.1016/b978-0-12-813068-1.00016-6>
- Yacoub, E., Harel, N., & Ugurbil, K. (2008). High-field fMRI unveils orientation columns in humans. *Proceedings of the National Academy of Sciences*, 105(30), 10607–10612. <https://doi.org/10.1073/pnas.0804110105>
- Yacoub, E., Shmuel, A., Logothetis, N., & Ugurbil, K. (2007). Robust detection of ocular dominance columns in humans using Hahn Spin Echo BOLD functional MRI at 7 Tesla. *NeuroImage*, 37(4), 1161–1177. <https://doi.org/10.1016/j.neuroimage.2007.05.020>
- Yang, X., Renken, R., Hyder, F., Siddeek, M., Greer, C. A., Shepherd, G. M., & Shulman, R. G. (2002). Dynamic mapping at the laminar level of odor-elicited responses in rat olfactory bulb by functional MRI. *Proceedings of the National Academy of Sciences*, 95(13), 7715–7720. <https://doi.org/10.1073/pnas.95.13.7715>
- Yu, X., Glen, D., Wang, S., Dodd, S., Hirano, Y., Saad, Z., ... Koretsky, A. P. (2012). Direct imaging of macrovascular and microvascular contributions to BOLD fMRI in layers IV-V of the rat whisker-barrel cortex. *NeuroImage*, 59(2), 1451–1460. <https://doi.org/10.1016/j.neuroimage.2011.08.001>
- Yu, X., Qian, C., Chen, D. Y., Dodd, S. J., & Koretsky, A. P. (2014). Deciphering laminar-specific neural inputs with line-scanning fMRI. *Nature Methods*, 11(1), 55–58. <https://doi.org/10.1038/nmeth.2730>
- Zappe, A. C., Pfeuffer, J., Merkle, H., Logothetis, N. K., & Goense, J. B. M. (2008). The effect of labeling parameters on perfusion-based fMRI in nonhuman primates. *Journal of Cerebral Blood Flow and Metabolism*, 28(3), 640–652. <https://doi.org/10.1038/sj.jcbfm.9600564>
- Zhang, N., Zhu, X. H., & Chen, W. (2008). Investigating the source of BOLD nonlinearity in human visual cortex in response to paired visual stimuli. *NeuroImage*, 43(2), 204–212. <https://doi.org/10.1016/j.neuroimage.2008.06.033>

- Zhao, F., Wang, P., Hendrich, K., Ugurbil, K., & Kim, S. G. (2006). Cortical layer-dependent BOLD and CBV responses measured by spin-echo and gradient-echo fMRI: Insights into hemodynamic regulation. *NeuroImage*, 30(4), 1149–1160. <https://doi.org/10.1016/j.neuroimage.2005.11.013>
- Zhou, J., Benson, N. C., Kay, K. N., & Winawer, J. (2018). Compressive Temporal Summation in Human Visual Cortex. *The Journal of Neuroscience*, 38(3), 691–709. <https://doi.org/10.1523/jneurosci.1724-17.2017>
- Zimmermann, J., Goebel, R., de Martino, F., van de Moortele, P. F., Feinberg, D., Adriany, G., ... Yacoub, E. (2011). Mapping the organization of axis of motion selective features in human area MT using high-field fmri. *PLoS ONE*, 6(12). <https://doi.org/10.1371/journal.pone.0028716>

Appendix

Nederlandse samenvatting

Zicht is een van de belangrijkste zintuigen. Hoewel de ogen belangrijk zijn in het verzamelen van visuele informatie, gebeurt het uiteindelijke 'zien' in de hersenen. Zicht is dusdanig belangrijk dat in mensen ongeveer een kwart van de grote hersenen bezig is met het verwerken en interpreteren van visuele informatie. Vanuit het oog reist visuele informatie via onder andere de oogzenuw naar de occipitaal kwab helemaal achterin het brein. Helemaal achterin de occipitaal kwab, verborgen tussen de twee hersenhelften in, ligt de primaire visuele cortex. Dit is de plek waar de eerste verwerking van de visuele informatie plaatsvindt. Vanuit de primaire visuele cortex wordt de informatie doorgestuurd naar andere hersengebieden, voornamelijk in de occipitaal en pariëtaal kwab.

Ieder hersengebied heeft zijn eigen functie. Hoe meer de visuele informatie al is verwerkt voordat deze een hersengebied bereikt, hoe complexer de informatie is die door dat gebied verwerkt wordt. Hierbij wordt onderscheid gemaakt tussen vroege waarneming en late waarneming. Vroege waarneming is gericht op de elementaire eigenschappen van beelden, ook wel stimuli genoemd. Zo verwerkt de primaire visuele cortex bijvoorbeeld informatie over contrast en verwerkt een ander gebied kleur-, en weer een ander gebied bewegingsinformatie. Late waarneming is gericht op de verwerking van gehele objecten in visuele informatie, bijvoorbeeld het detecteren van een gezicht in visuele informatie. Er zijn ook meerdere gebieden die zich bezighouden met hoeveelheidsperceptie. Deze gebieden houden zich niet bezig met 'simpele' stimulus eigenschappen als kleur en richting, maar verwerken vrijwel uitsluitend informatie over hoeveel dingen (bijvoorbeeld auto's op een rustige parkeerplaats of koekjes op een bord; zie Figuur 4 in de Introductie) er zijn binnen ons visuele veld op een bepaald moment. Dit gaat dusdanig automatisch dat we vaak in één oogopslag zien hoeveel relevante dingen zich ergens bevinden, maar alleen als het een klein aantal is (tot 5 à 6). Probeer het maar eens met bijvoorbeeld de borden op tafel of objecten aan een muur.

De hersenschors is de buitenste 1,5 – 4 millimeter van de grote hersenen. In deze laag, ook wel cortex of grijze stof genoemd, bevindt zich het grootste deel van de cellichamen van de ruwweg 100 miljard hersencellen. Hier vindt ook de meeste informatieoverdracht plaats tussen de hersencellen. De cortex is in het algemeen op te delen in zes verschillende lagen, genummerd met de Romeinse cijfers I-VI. Iedere laag ziet er onder een microscoop net een beetje anders uit (zie Figuur 1 in de Introductie). Een deel van de informatieverwerking in de cortex vindt plaats tussen verschillende hersengebieden. Het grootste deel vindt echter plaats tussen neuronen (zenuwcellen) binnen en vooral tussen de lagen van de cortex.

In de visuele cortex komt informatie binnen in laag IV. Deze informatie verspreidt zich van daaruit lateraal naar de diepere (lagen V en VI) en hoger liggende lagen (dichter bij het oppervlak van de cortex; lagen I, II en III). Terugkoppeling vanuit hersengebieden later in de verwerkingshiërarchie arriveert in alle lagen behalve laag IV. Deze terugkoppeling kan bestaan uit bijvoorbeeld informatie over op welk deel van een stimulus je je aandacht moet vestigen.

Neuronen hebben zuurstof nodig om te kunnen functioneren. Ze kunnen namelijk zelf geen energie opslaan. Zuurstof wordt aangeleverd door het bloed. Grote bloedvaten liggen op het oppervlak van de cortex. Deze vertakken zich in kleinere bloedvaten die haaks op het corticale oppervlak staan. Deze 'dalende' bloedvaten zorgen voor de toevoer van zuurstofrijk bloed. Zuurstofarm bloed wordt vervolgens afgevoerd door 'stijgende' bloedvaten die in tegenovergestelde richting naar het corticale oppervlak gaan en vervolgens samenkomen in de grote bloedvaten die daar liggen (zie Figuur 2 in de Introductie). Doordat de stijgende bloedvaten vaak bloed afvoeren dat afkomstig is uit verschillende corticale lagen, is de totale hoeveelheid zuurstofarm bloed in zo'n bloedvat in een bepaalde laag de combinatie van zuurstofarm bloed uit de betreffende laag en het zuurstofarme bloed uit andere lagen. De lokale hoeveelheid zuurstofarm bloed is dus afhankelijk van de betreffende laag en alle onderliggende lagen.

Magnetic resonance imaging (MRI) is een niet-invasieve beeldvormingstechniek waarbij door middel van een grote elektromagneet beelden van het lichaam gemaakt worden. Deze techniek kan ook gebruikt worden om hersenactiviteit in kaart te brengen; dit heet functionele MRI (fMRI). Met fMRI meet je de balans tussen zuurstofrijk en zuurstofarm bloed en daarmee, indirect, de activiteit van neuronen. Tot voor kort was het alleen mogelijk om informatieverwerking in detail te bestuderen in dieren, door middel van operationeel geplaatste elektroden. De afgelopen jaren zijn MRI-magneten echter steeds sterker geworden. Hierdoor is de kwaliteit en resolutie van de fMRI beelden sterk toegenomen. Tegenwoordig zijn er scanners met extreem sterke magneten van 7 Tesla beschikbaar voor hersenonderzoek. Dit is equivalent aan ongeveer 1500 koelkastmagneten. Met deze scanners is het mogelijk om hersenfuncties te onderzoeken met een resolutie van minder dan een millimeter. Hiermee is het mogelijk om informatieverwerking tussen de verschillende lagen van de cortex te onderzoeken, waar een groot deel van de informatieverwerking plaatsvindt. Daarom noemen we deze techniek ook wel laminaire fMRI.

Laminaire fMRI is in de afgelopen jaren gebruikt om onder andere de vroege visuele verwerking te bestuderen in mensen. Hoewel we hiervan al veel geleerd hebben, is het interessanter om late visuele verwerking te bestuderen. Deze is moeilijk te onderzoeken in dieren, maar een stuk makkelijker in mensen. In dit proefschrift onderzoek ik de laminaire organisatie van late visuele informatieverwerking. Ik gebruik hiervoor voornamelijk laminaire fMRI, maar ook intracraniale (onder de schedel) metingen.

Een van de fundamentele aannames van algemene fMRI dataverwerking en interpretatie is dat er een evenredig verband bestaat tussen neuronale activiteit en het gemeten fMRI signaal. Dit wordt ook wel de lineariteit aanname genoemd. Echter, vanwege de afhankelijkheid van het lokale fMRI-signaal van signalen in andere lagen in de cortex, is de lineariteit aanname mogelijk niet geldig. Dit kan resulteren in verkeerde uitkomsten die kunstmatig hoog of laag zijn, wat kan leiden tot een verkeerde interpretatie van de resultaten. In **Hoofdstukken 2 & 3** beoordeel ik de geldigheid van de lineariteit aanname voor laminaire fMRI. Hierin laat ik zien dat aan de eisen op dit punt voldaan wordt voor laminaire fMRI-metingen van visuele informatieverwerking. Hiermee leggen we de grondslag voor een bredere toepassing van laminaire fMRI.

In **Hoofdstuk 4** pas ik laminaire fMRI toe op een neurowetenschappelijk vraagstuk: hoe verloopt de informatieverwerking tussen verschillende lagen van de cortex in een hersengebied dat gespecialiseerd is in hoeveelheidsperceptie? Hiervoor gebruiken we een data-analysemethode om de verwachte reactie van een groep neuronen te voorspellen, die we vervolgens optimaliseren naar de gemeten reactie. Aan de hand hiervan kunnen we de hoeveelheid bepalen waarop een groep neuronen het sterkst reageert. Daarnaast kunnen we ook bepalen op welke hoeveelheden deze groepen neuronen specifiek reageren; dit noemen we ook wel de afstembreedte. Ik laat zien dat de verschillende corticale lagen geen voorkeur hebben voor een bepaalde hoeveelheid. Daarnaast toon ik aan dat de afstembreedte nagenoeg gelijk is tussen de verschillende corticale lagen. In de primaire visuele cortex varieert een vergelijkbare maat tussen corticale lagen, waarbij deze het kleinste is in laag IV en groter wordt richting de diepere en hoger liggende lagen. Hierdoor ontstaat een U-vormig profiel. Dit profiel is een directe afspiegeling van de corticale informatieverwerking, waarbij informatie aankomt in laag IV en verwerkt wordt richting zowel de diepere als hoger liggende lagen. Aangezien de afstembreedte in de hoeveelheidscortex een nagenoeg horizontale lijn laat zien over corticale diepte, concludeer ik dat de informatiestromen voor late visuele verwerking (in de hoeveelheidscortex) fundamenteel verschillen van die voor vroege visuele verwerking (in de visuele cortex).

In **Hoofdstuk 5** zet ik de onderzoekslijn van het vorige hoofdstuk voort. Ik gebruik in dit hoofdstuk intracraniale metingen (electrocorticografie; ECoG) om de reactie over tijd te meten van groepen neuronen. Het grote voordeel van intracraniale metingen is dat deze op de milliseconde precies de elektrische signalen van neuronen meten, in tegenstelling tot laminaire fMRI waarmee deze signalen, indirect, slechts eens per minimaal een seconde kunnen worden gemeten. Voor intracraniale metingen wordt de schedel verwijderd en worden er elektroden direct op het oppervlak van de hersenschors geplaatst. Deze operatie brengt logischerwijs risico's met zich mee en wordt daarom alleen uitgevoerd als het medisch noodzakelijk is. Vaak is dit in het geval van epilepsie, waarbij de elektroden helpen met het opsporen van de bron van de epilepsie. Terwijl de elektroden op het brein aanwezig zijn, nemen sommige patiënten deel aan wetenschappelijk onderzoek. Wij hebben tijdens een van deze onderzoeken stimuli met verschillende hoeveelheden laten zien aan deze patiënten. Ik laat zien dat zich in de pariëtaal kwab een groep neuronen bevindt die selectief reageert op bepaalde hoeveelheden, op een locatie die overeenkomt met die in het vorige hoofdstuk (gemeten met fMRI). Daarnaast toon ik aan dat de reacties van deze groep neuronen duidelijk verschillen van reacties van neuronen in de visuele cortex.

In dit proefschrift laat ik zien dat laminaire fMRI toegepast kan worden op late visuele waarnemingsprocessen. Eerst heb ik een aantal aannames getest over het verband tussen neuronale activiteit en het fMRI signaal die mogelijk niet geldig zijn voor laminaire fMRI. Ik heb aangetoond dat deze aannames veilig gemaakt kunnen worden voor laminaire fMRI van visuele verwerking. Daarnaast heb ik deze kennis gebruikt in het onderzoeken van laminaire responsen in een hersengebied dat informatie over hoeveelheden verwerkt. Daarmee heb ik aangetoond dat de informatieverwerking voor deze late visuele verwerking fundamenteel verschilt van informatieverwerking tijdens vroege visuele verwerking. Dit heb ik verder onderbouwd door middel van intracraniale metingen in epilepsiepatiënten. Al met al is laminaire fMRI een veelbelovende techniek waarmee we neurowetenschappelijke vraagstukken kunnen beantwoorden die tot voor kort moeilijk te bestuderen waren.

Appendix

List of publications

Published peer-reviewed articles

Klein, B. P., Fracasso, A., **van Dijk, J. A.**, Paffen, C. L., Te Pas, S. F., & Dumoulin, S. O. (2018). Cortical depth dependent population receptive field attraction by spatial attention in human V1. *NeuroImage*, 176, 301-312.

Ferrè, E.R., Iannetti, G.D., **van Dijk, J.A.**, Haggard, P. (2018). Ineffectiveness of tactile gating shows cortical basis of nociceptive signaling in the Thermal Grill Illusion. *Scientific Reports*.

Ahmadi, K., Fracasso, A., **van Dijk, J. A.**, Kruijt, C., Van Genderen, M., Dumoulin, S. O., & Hoffmann, M. B. (2018). Altered organization of the visual cortex in FHONDA syndrome. <https://doi.org/10.1016/j.neuroimage.2018.02.053>

van Dijk, J. A., de Haas, B., Moutsiana, C., & Schwarzkopf, D. S. (2016). Intersession reliability of population receptive field estimates. *NeuroImage*, 143. <https://doi.org/10.1016/j.neuroimage.2016.09.013>

Moutsiana, C., De Haas, B., Papageorgiou, A., **van Dijk, J. A.**, Balraj, A., Greenwood, J. A., & Schwarzkopf, D. S. (2016). Cortical idiosyncrasies predict the perception of object size. *Nature Communications*, 7. <https://doi.org/10.1038/ncomms12110>

Articles in preparation (data presented in this thesis)

van Dijk, J.A., Fracasso, A., Petridou, N., & Dumoulin, S.O. (submitted). Linear amplitude scaling across cortical depth for laminar fMRI.

van Dijk, J.A., Fracasso, A., Petridou, N., & Dumoulin, S.O. (in preparation). Evaluating temporal additivity for laminar fMRI.

van Dijk, J.A., Fracasso, A., Petridou, N., & Dumoulin, S.O. (in preparation). Numerosity-selective population receptive field properties across cortical depth.

van Dijk, J.A., de Jong, M.C., Piantoni, G., Fracasso, A., van Steensel, M., Petridou, N., & Dumoulin, S.O. (in preparation). Intracranial recordings show evidence of numerosity tuning in human parietal cortex.

Articles in preparation (data not presented in this thesis)

Cai, Y., **van Dijk, J.A.**, Hofstetter, S., Zuiderbaan, W., van der Zwaag, W., Harvey, B.M., Dumoulin, S.O. (in preparation). Topographic numerosity maps dynamically adjust to the presented numerosity range.

Appendix

Curriculum Vitae

Jelle A. van Dijk was born on the 19th of May 1991 in Delft, the Netherlands. He finished his secondary education at Stichtse Vrije School in Zeist in 2010. He subsequently moved to Utrecht to study at University College Utrecht, where he obtained his bachelor's degree (cum laude) in a combination of cognitive neuroscience, mathematics, chemistry, psychology, and physics in 2013. To pursue a master's degree in cognitive neuroscience, he moved to London (United Kingdom), where he studied at University College London (UCL). He obtained his degree (cum laude) in 2014, completing his dissertation in the lab of Dr. Sam Schwarzkopf. He then spent a year working as a research and personal assistant in the lab of Prof. Dr. Patrick Haggard in his lab at UCL. In 2015, he started his PhD at the experimental psychology department of Utrecht University and later also the Spinoza Centre for Neuroimaging (Amsterdam) under supervision of Prof. Dr. Serge Dumoulin (promotor), Dr. Natalia Petridou (co-promotor), and Dr. Alessio Fracasso (co-promotor). During his PhD candidacy, he also spent time on projects in the labs of Prof. Dr. Hoffmann (Otto von Guericke Universität, Magdeburg, DE), and Prof. Dr. Rainer Goebel (Maastricht University, NL), as part of the NextGenVis training network (nextgenvis.eu). Jelle will now continue to work for Prof. Dr. Serge Dumoulin as post-doctoral researcher.